



**UNIVERSITY OF CAPE TOWN**  
IYUNIVESITHI YASEKAPA • UNIVERSITEIT VAN KAAPSTAD

DEPARTMENT OF CIVIL ENGINEERING

*Masters Thesis*

---

**Towards a material damage model using  
the logarithmic strain, with *von Mises*  
plasticity considerations**

---



A DISSERTATION TOWARDS FULFILMENT OF THE REQUIREMENTS  
FOR A MASTER OF SCIENCES DEGREE IN STRUCTURAL  
ENGINEERING & MATERIALS.

*The financial assistance of Mr. Shadric Namalomba is hereby acknowledged.  
Opinions expressed and conclusions arrived at, are solely those of the author.*

***Author:***

Mr. Paul NAMALOMBA

***Supervisor:***

Prof. Sebastian SKATULLA

***Co-supervisor:***

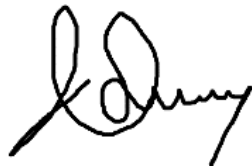
Dr. Keith MACHUTCHON

**June, 2022**

# Plagiarism declaration

1. I know that plagiarism is wrong. Plagiarism is to use another's work and to pretend that it is one's own.
2. This dissertation is my own work, save for that which is properly acknowledged through appropriate citation and referencing.
3. I have not allowed and will not allow anyone to copy my work with the intention of passing it as his or her own work.
4. This dissertation has been submitted to the Turnitin module and I confirm that my supervisor has seen my report and any concerns revealed by such have been resolved with my supervisor.

Signature

A handwritten signature in black ink, appearing to be 'J. Dwyer', written in a cursive style.

# Abstract

Damage is briefly defined as the presence and growth of micro-defects in a material. This study serves to describe the computational implementation of the material damage theory adopted for ductile materials. Thus, pays attention to the computational analysis of the physical behaviour of materials under finite deformations — in particular, the stress-strain behaviour, load-deformation behaviour and location of weak zones.

Throughout this study, non-linear continuum mechanics is utilised as the mathematical basis of the constitutive and general finite element framework. In continuum mechanics, there exists no requirement to discretely characterise each micro-crack that grows in a material, thus making it possible to provide analysis of the stress and strain response affected by micro-defects using *material particles*, which are localised collections of many *atomic*-scale particles. The continuum is thus a sum of its material particles. To complement this description of mechanics, constitutive and phenomenological equations are adopted from the non-linear thermodynamic phenomena of elasticity, plasticity, and damage; the laws of thermodynamics will therefore apply and are shown as such.

The proposed material damage model is developed and implemented in the back-end of the in-house computational mechanics toolbox SESKA, which uses finite element-based discretisation and approximation techniques. Field and scalar quantities, such as stress and strain, are computed with the use of the *return-mapping method*. The stress measures utilised are the 2<sup>nd</sup> *Piola-Kirchhoff* stress  $\mathbf{S}$  and the *Mandel* stress  $\mathbf{\Sigma}$ . The *Newton-Raphson* update scheme is applied in the plasticity evolution equations via the plastic multiplier (denoted  $\lambda$ ), which innately controls the evolution of all other inelastic phenomena. Damage is a function of plastic evolution and thus plays a role in the plasticity multiplier calculation. Moreover, this proposed model makes the assumption of full isotropy, all material properties at a material point are the same in tension and compression and the same regardless of the dimension.

Finally, several examples are utilised to showcase the model and all the intricacies are presented — the problem setup, boundary condition assignment and multi-layered analysis are detailed in the content of this study and the examples perform well under qualitative scrutiny. These examples include a cantilevered beam model, a simply supported bending model and a plane strain example to evaluate whether the material model achieves qualifiable correlation to expected behaviour and to assess whether the damage-related parameters affect the stress

and strain behaviour as expected. In brief conclusion, this paper shows that the model achieves qualifiable correlation and all the material parameters function as expected.

# Acknowledgements

I would like to thank my father and sponsor Shadric Namalomba, and my mother and moral support Chrissie Linda Namalomba, for all they do to support my education and other endeavours.

I would also like to give thanks to Prof. Sebastian Skatulla, at the University of Cape Town for the providing the research opportunity and supervision throughout the entire period of my research.

Quite crucial was the help of UCT HPC, in particular Andrew Lewis, for allowing me to use the high-performance computing capability to advance this study. Thanks to them for all their assistance.

# Table of Contents

|   |           |
|---|-----------|
| Plagiarism declaration                                | I         |
| Abstract  | II        |
| Acknowledgements                                      | IV        |
| Table of Contents                                     | VIII      |
| List of Figures                                       | XI        |
| List of Tables  | XII       |
| <b>1 Introduction</b>                                 | <b>1</b>  |
| 1.1 Background to the study . . . . .                 | 1         |
| 1.2 Aim and objectives of the study . . . . .         | 3         |
| 1.3 Scope and limitations . . . . .                   | 4         |
| 1.4 Layout of this document . . . . .                 | 5         |
| <b>2 Non-linear continuum mechanics theory</b>        | <b>6</b>  |
| 2.1 Introduction . . . . .                            | 6         |
| 2.2 Continuum configurations . . . . .                | 7         |
| 2.3 Kinematics . . . . .                              | 8         |
| 2.3.1 Differentiation of quantities . . . . .         | 8         |
| 2.3.2 Deformation gradient . . . . .                  | 10        |
| 2.3.3 Strain tensors . . . . .                        | 11        |
| 2.3.4 Strain-rate tensors . . . . .                   | 12        |
| 2.4 Stress concepts . . . . .                         | 13        |
| 2.5 Balance and conservation equations . . . . .      | 14        |
| 2.5.1 Balance of mass . . . . .                       | 14        |
| 2.5.2 Balance of linear momentum . . . . .            | 16        |
| 2.5.3 Balance of rotational momentum . . . . .        | 17        |
| 2.5.4 Balance of mechanical energy . . . . .          | 19        |
| 2.5.5 Balance of thermal energy . . . . .             | 21        |
| 2.5.6 Irreversibility of entropy production . . . . . | 22        |
| <b>3 Material damage theory</b>                       | <b>25</b> |
| 3.1 Damage phenomenology . . . . .                    | 25        |
| 3.2 Isotropic damage variable . . . . .               | 26        |

|          |  |           |
|----------|--|-----------|
| 3.3      | Effective stress concept . . . . .                             | 27        |
| 3.4      | Thermodynamic potential & dissipation potential . . . . .      | 29        |
| 3.4.1    | <i>Helmholtz</i> free-energy function . . . . .                | 29        |
| 3.4.2    | Entropy and dissipation . . . . .                              | 30        |
| <b>4</b> | <b>Modelling local elastoplastic-damage</b>                    | <b>32</b> |
| 4.1      | The general approach . . . . .                                 | 32        |
| 4.2      | Large deformation elastoplasticity . . . . .                   | 33        |
| 4.2.1    | Multiplicative decomposition of deformation gradient . . . . . | 33        |
| 4.2.2    | <i>Cauchy-Green</i> strain . . . . .                           | 34        |
| 4.2.3    | Plastic <i>strain-rate</i> . . . . .                           | 35        |
| 4.3      | <i>Mandel</i> stress measure . . . . .                         | 35        |
| 4.4      | Thermodynamic state variables . . . . .                        | 36        |
| 4.4.1    | Observed state variables . . . . .                             | 37        |
| 4.4.2    | Internal state variables . . . . .                             | 37        |
| 4.4.3    | Associated energetic variables . . . . .                       | 37        |
| 4.5      | Free-energy and dissipation . . . . .                          | 38        |
| 4.6      | Elasticity and strain . . . . .                                | 40        |
| 4.6.1    | <i>Hencky</i> strain measure . . . . .                         | 40        |
| 4.6.2    | Elastic constitutive relations . . . . .                       | 42        |
| 4.7      | Plasticity and damage evolution . . . . .                      | 43        |
| 4.7.1    | <i>von Mises</i> Yield criterion . . . . .                     | 43        |
| 4.7.2    | Damage energy density . . . . .                                | 43        |
| 4.7.3    | Non-linear isotropic hardening . . . . .                       | 44        |
| 4.7.4    | Phenomenological evolution laws . . . . .                      | 44        |
| <b>5</b> | <b>Computational methods</b>                                   | <b>47</b> |
| 5.1      | Summary of the material damage model . . . . .                 | 47        |
| 5.2      | The computational work-flow . . . . .                          | 48        |
| 5.3      | Finite element formulations . . . . .                          | 49        |
| 5.3.1    | Weak form of momentum balance . . . . .                        | 49        |
| 5.3.2    | Spatial discretisation principles . . . . .                    | 50        |
| 5.3.3    | Linearisation of the weak form . . . . .                       | 51        |
| 5.4      | Numerical treatment . . . . .                                  | 54        |
| 5.4.1    | Principles of the <i>Newton-Raphson</i> method . . . . .       | 54        |
| 5.4.2    | Local time discretisation . . . . .                            | 55        |
| 5.4.3    | Local iterative update of plastic multiplier . . . . .         | 56        |
| 5.5      | Algorithmic implementation . . . . .                           | 56        |

|          |  |           |
|----------|--|-----------|
| 5.5.1    | Elastic-plastic predictor algorithms . . . . .                                   | 56        |
| 5.5.2    | Return mapping algorithms . . . . .  | 59        |
| 5.5.3    | <i>Piola-Kirchhoff</i> stress computation . . . . .                              | 62        |
| 5.5.4    | Algorithmic tangent operator . . . . .   | 63        |
| <b>6</b> | <b>Results and example simulations</b>   | <b>65</b> |
| 6.1      | Tip-loaded cantilever beam . . . . .   | 65        |
| 6.1.1    | Problem setup, meshing and boundary conditions . . . . .                         | 66        |
| 6.1.2    | Material properties . . . . .  | 67        |
| 6.1.3    | Load-deformation analysis . . . . .  | 67        |
| 6.1.4    | Analysis of stress and strain localisation . . . . .                             | 69        |
| 6.2      | 3-point bending of simply supported slender square bar . . . . .                 | 72        |
| 6.2.1    | Problem description . . . . .  | 72        |
| 6.2.2    | Material properties . . . . .  | 72        |
| 6.2.3    | Meshing and boundary conditions . . . . .  | 73        |
| 6.2.4    | The effect of damage energetic strength on load-carrying capacity . . . . .      | 74        |
| 6.2.5    | Analysis of damage evolution and cracking . . . . .                              | 76        |
| 6.2.6    | Generalised damage distribution in the bar . . . . .                             | 77        |
| 6.3      | Uniaxial plane tension of 3D solid plates with different thickness . . . . .     | 79        |
| 6.3.1    | Problem configuration . . . . .  | 79        |
| 6.3.2    | Material properties . . . . .  | 80        |
| 6.3.3    | Meshing and boundary conditions . . . . .  | 81        |
| 6.3.4    | Load-deformation analysis . . . . .  | 82        |
| 6.3.5    | Analysis of necking and strain localisation phenomena . . . . .                  | 85        |
| <b>7</b> | <b>Discussions</b>   | <b>87</b> |
| 7.1      | Continuum damage mechanics framework . . . . .                                   | 87        |
| 7.2      | Constitutive damage coupling <i>vs.</i> finite element damage coupling . . . . . | 88        |
| 7.3      | Yield criteria and associated flow rule . . . . .                                | 88        |
| 7.4      | <i>Newton-Raphson</i> procedure . . . . .  | 89        |
| 7.5      | Predictive capability of this model . . . . .                                    | 89        |
| 7.6      | Effect of the damage energetic strength parameter . . . . .                      | 90        |
| <b>8</b> | <b>Future work and study</b>   | <b>91</b> |
| 8.1      | <i>Drucker-Prager</i> yield criterion . . . . .                                  | 91        |
| 8.2      | Implementation of meso-scale void-closure effects . . . . .                      | 91        |
| 8.3      | Implementation of viscoplastic damage . . . . .                                  | 92        |



|                     |   |
|---------------------|---|
| <b>Bibliography</b> | <b>93</b>   |
| <b>Appendix</b>     | <b>A1</b>   |
| A                   | Expansion of finite element related quantities into index notation . . . . . A1 |
| A.1                 | Weak form of the momentum balance . . . . . A1                                  |
| A.2                 | Approximation of the displacement-related fields . . . . . A1                   |
| A.3                 | Index form of linearised quantities . . . . . A2                                |
| B                   | Expansion of return-mapping quantities into index notation . . . . . A3         |
| B.1                 | Algorithmic tangent operator . . . . . A3                                       |
| B.2                 | Stress computation . . . . . A3   |
| B.3                 | Flow vector . . . . . A4  |
| B.4                 | Strain measures . . . . . A4  |
| B.5                 | <i>Strain-rate</i> measures . . . . . A4  |
| C                   | Ethics approval . . . . . A5  |

# List of Figures

|     |  |    |
|-----|--|----|
| 2.1 | Configurations of a continuum under deformation [14]. The reference configuration defines the continuum $\mathcal{B}$ at time $t = 0$ , whilst the current configuration defines the continuum at time $t$ . $P = P(\mathbf{X})$ and $p = P(\mathbf{x}, t)$ . . . . .  | 8  |
| 2.2 | Deformation of the continuum with deformation of $\chi$ . The reference configuration defines the continuum $\mathcal{B}$ at time $t = 0$ , whilst the current configuration defines the continuum at time $t$ . $P = P(\mathbf{X})$ , $p = P(\mathbf{x}, t)$ and $Q = Q(\mathbf{X})$ , $q = Q(\mathbf{x}, t)$ . . . . . | 11 |
| 2.3 | Schematic representation of 3D infinitesimal stress block showing the external force vector and the surface traction vector. . . . .   | 13 |
| 3.1 | Material damage theory represented in a material body. Showing microvoid presence [24]. . . . .  | 26 |
| 3.2 | Schematic representation of a loaded square block showing the external force vector and the surface traction vector. . . . .   | 28 |
| 4.1 | Schematic diagram showing the multiplicative decomposition of deformation gradient $\mathbf{F}$ . The intermediate configuration shows the split between elasticity and plasticity. . . . .  | 33 |
| 5.1 | Work-flow chart within simulation step . . . . .   | 48 |
| 5.2 | Newton-Raphson method. The function space contains the possible values a function may take and the solution space the possible values the inputs to the function may take. . . . .   | 54 |
| 6.1 | Mesh, problem configuration & boundary conditions. The cantilever beam model used a 3D mesh of 80 hexahedral volume elements. The fixity and loading conditions are shown. . . . .   | 66 |
| 6.2 | Deformation in the $z$ -axis (bending) compared with deformation in the $x$ -axis from $u_z : 0 \text{ m} \rightarrow 4.776 \text{ m}$ . Left-side is the damaged plasticity simulations and right-side is the undamaged plasticity. . .   | 68 |
| 6.3 | Damaged <i>vs</i> Undamaged Plasticity, Load <i>vs</i> Deformation in the Vertical $z$ -axis up to vertical displacement $u_z = 4.776 \text{ m}$ at Point $p_0$ . . .  | 68 |
| 6.4 | <i>Smoothed damage variable</i> contour plot for the cantilever beam model at vertical displacement $u_z = 2.365 \text{ m}$ . Damaged plasticity with isotropic hardening. . . . .   | 70 |

|      |   |    |
|------|---|----|
| 6.5  | Equivalent plastic strain smoothed contour plot for the cantilever beam model at vertical displacement $u_z = 2.365 m$ . Pure plasticity with isotropic hardening. . . . .            | 70 |
| 6.6  | Equivalent plastic strain smoothed contour plot for the cantilever beam model at vertical displacement $u_z = 2.365 m$ . Damaged plasticity with isotropic hardening. . . . .         | 71 |
| 6.7  | Effective stress plot smoothed contour plot for the cantilever beam model at vertical displacement $u_z = 2.365 m$ . Pure plasticity with isotropic hardening. . . . .                | 71 |
| 6.8  | Effective stress plot smoothed contour plot for the cantilever beam model at vertical displacement $u_z = 2.365 m$ . Damaged plasticity with isotropic hardening. . . . .             | 71 |
| 6.9  | Schematic representation of the slender bar bending example. . . . .  | 72 |
| 6.10 | Mesh, problem configuration & boundary conditions. The roller-supported bar model used a 3D mesh of 80 hexahedral volume elements and 172 quadrilateral surface elements. . . . .     | 74 |
| 6.11 | Damaged <i>vs</i> Undamaged Plasticity, Load <i>vs</i> Deformation in the $z$ -axis up to vertical displacement $u_z = 200 mm$ at Point $p_0$ . . . . .                               | 75 |
| 6.12 | A line plot of the evolution of <i>smoothed damage variable</i> at Point A on the bar <i>vs</i> the $z$ -axis deformation (downwards) at Point A on the bar. $S = 1.25 MPa$ . . . . . | 76 |
| 6.13 | A line plot of the time evolution of <i>smoothed damage variable</i> and the the $z$ -axis deformation (downwards) at Point A on the bar. $S = 1.25 MPa$ . . . . .                    | 77 |
| 6.14 | <i>Smoothed damage variable</i> contour plot for the simple beam model at vertical displacement $u_z = 115.16 mm$ . Damaged plasticity with $S_0 = 1.25 MPa$ . . . . .                | 77 |
| 6.15 | <i>Smoothed damage variable</i> contour plot for the 3-point bending bar model with $S_0 = 1.00 MPa$ at vertical displacement $u_z = 100 mm$ . . . . .                                | 78 |
| 6.16 | <i>Smoothed damage variable</i> contour plot for the 3-point bending bar model with $S_0 = 1.25 MPa$ at vertical displacement $u_z = 100 mm$ . . . . .                                | 78 |
| 6.17 | <i>Smoothed damage variable</i> contour plot for the 3-point bending bar model with $S_0 = 1.50 MPa$ at vertical displacement $u_z = 100 mm$ . . . . .                                | 79 |
| 6.18 | <i>Smoothed damage variable</i> line plot along the bar's $x$ -axis dimension, with distance shown from the mid-span at vertical deflection of $u_z = 100 mm$ . . . . .               | 79 |

|      |  |    |
|------|--|----|
| 6.19 | 2D schematic representation of the solid plane under tension example. ( <i>Units = mm</i> ) . . . . .  | 80 |
| 6.20 | Mesh & boundary conditions in the quarter model of the plate in uniaxial tension with $d_{plate} = 1.0 \text{ mm}$ . The fixity and displacement conditions are shown. . . . .   | 82 |
| 6.21 | Mesh & boundary conditions in the quarter model of the plate in uniaxial tension with $d_{plate} = 2.0 \text{ mm}$ . The fixity and displacement conditions are shown. . . . .   | 83 |
| 6.22 | Mesh & boundary conditions in the quarter model of the plate in uniaxial tension with $d_{plate} = 3.0 \text{ mm}$ . The fixity and displacement conditions are shown. . . . .   | 83 |
| 6.23 | Load <i>vs</i> Deformation in the $z$ -axis up to vertical displacement $u_z = 4.14 \text{ mm}$ for a node at the loaded surface. . . . .  | 84 |
| 6.24 | Evolution of lateral displacement ( $y$ -axis displacement) showing necking behaviour at Point B at the base of the quarter plate through the simulation. . . . .  | 84 |
| 6.25 | Deformation profile and strain localisation plot of the full solid plate model as viewed in the $yz$ -plane. On the left is the undeformed plate and on the right, the deformed plate at $u_{z,max} = 4.14 \text{ mm}$ . . . . . | 85 |

# List of Tables

|     |   |    |
|-----|---|----|
| 6.1 | Material properties of cantilever beam. . . . .             | 67 |
| 6.2 | Material behaviour at peak loading at Point $p_0$ . . . . . | 69 |
| 6.3 | Material properties of slender square bar. . . . .          | 73 |
| 6.4 | Material behaviour at maximum loading at Point A. . . . .   | 75 |
| 6.5 | Material properties of solid plate [44]. . . . .            | 81 |
| 6.6 | Material behaviour at peak axial loading. . . . .           | 84 |

# Chapter 1

## Introduction

### 1.1 Background to the study

Damage is briefly defined as the presence and growth of micro-defects in a material. Micro-defects in all contexts of damage are described as microscopic discontinuities which may manifest in several forms and take several different paths of growth. An instance of micro-defects are micro-voids, which manifest as a result of continuous supply of external mechanical work to break the atomic bonds that hold together homogeneous areas containing imperfections that already exist, such as lattice defects and dislocations — this is often known as ductile damage. Another instance are micro-cracks, which occur as a result of exceeding the elastic stored energy threshold by a supply of external mechanical work done to the material [17]; the phenomena of damage may only proceed if the micro-cracks are allowed to grow and connect to other small cracks upon persistent supply of external mechanical work — this is known as brittle damage [20].

However, a microscopic approach to characterising damage may require quite diligent experimental methods and compelling computational methodology. For one to be able to effectively apply the scientific method at the microscale of a material, to discretise material behaviour at this scale, computational resources are always a limiting factor — the characterisation of microscopic voids or defects requires specific statistical, chemical and physical approaches. For example, in discovering the thermodynamic of entropy in particles at the microscale, one would need to invoke the *Boltzmann-Planck* equation [35] which requires some probabilistic quantisation of a number of atoms of order  $10^{23}$  or more per particle — this would be resource intensive. It is clear that for a constitutive formulation, a discrete approach would be quite cumbersome. Furthermore, in structural engineering applications there is no need to incorporate micro-mechanics unless the micro-mechanical concepts convey a distinctly different physical reality to that at the macroscale. Thus, the use of continuum damage mechanics is often employed. This was a field pioneered in the mid to late 20<sup>th</sup> century, where non-linear continuum mechanics and the mechanics and thermodynamics of material damage theory are combined to effectively describe damage phenomena in a continuous material volume [43]. Continuum damage theory removes a focus on microscopic particles but rather collects them into larger particles of approximately  $0.1 \text{ mm}^3$  in size [24] for ductile materials; these particles form the infinitely divisible continuum body [19] and are

spread throughout the material regardless of any discontinuities and defects that may occur at the microscale. This may be otherwise interpreted as the meso-scopic overview of material damage phenomena, which then requires a local material description of damage and follows some of the principles in [13] as it pertains to "smearing" damage. It abandons any requirement for a discrete crack analysis approach as in [10]. The continuum itself may be defined in two configurations: the material (reference) configuration, which is the reference state of the continuum or the current configuration which is the deformed state of the continuum, and the mechanics of each are detailed in this thesis.

Damage is a similar thermodynamic mechanism to plasticity and plastic hardening/softening in that all these mechanisms dissipate internal energy at yielded points in a material [24]. *Dissipation* is defined as the process by which work done from external mechanical or thermal actions is converted to internal heat, which produces *entropy*. It follows from the 2<sup>nd</sup> law of thermodynamics that the production of entropy is irreversible [8], thus damage is an irreversible mechanism. This basic theory of damage is crucial to any study of material damage and crucial to the content of this study. Damage, when analysed at the meso- or micro- scale, is as a consequence of the growth and nucleation of micro-defects into singular cracks that may eventually form macroscopic cracks [23]. This may introduce discontinuities into the continuum at the mesoscale as damage evolves and by employing the isotropic damage approach, each micro-crack is extant in all three dimensions across the entire volume; this has the implication of degrading the material properties to compensate for the growth of micro-defects. Logically, the more micro-defects that exist in the continuum, the higher the degree of degradation of stiffness and elastic moduli. This results in a reduction of material's effective load-carrying capacity [23]. These concepts are the backbone of the proposed material damage model.

The material damage model is developed and implemented in the back-end of the in-house computational mechanics toolbox SESKA<sup>1</sup>, which uses finite element-based approximation and integration techniques. In SESKA, each simulation has simulation steps which contain iterative steps intrinsically. This model uses the *Mandel* stress measure [28] (defined in an intermediate configuration in elasto-plastic applications) in the computation of variables as shall be seen later in this thesis, and is important since our solving techniques employ the use of trial (inter-

---

<sup>1</sup>SESKA is a computational framework that has been developed by Prof. Sebastian Skatulla (**PhD**), who developed the entire foundation of SESKA and a majority of its material. On top of that, SESKA contains plenty of material models which are implemented by other researchers. Notably, the Phase Field fracture model by Mr. Emmanuel Omatuku-Ngongo (**MSc**) and Theory of Porous Media based models by Mr. Gary Hopkins (**MSc**) are currently part of the SESKA framework.

mediate) approximations which are then refined as the simulation progresses; the trial (Mandel) stress is then pulled back to the material configuration as the 2nd *Piola-Kirchhoff* stress, which records stress in the material configuration. Furthermore, the use of the *logarithmic strain* [12] precisely characterises finite strains in iterative increments, whilst the *material velocity gradient* is used to characterise *rate of strain* — as per the thermodynamic framework of this model. It is noted here that the background FEM details such as the spatial discretisation of the displacement and weak formulations are explored.

The implementation of this model makes several other assumptions: localised material isotropy in tension and compression, and damage analysis only includes behaviour up to the failure limit, this model does not assess fracture and all the nuances of fracture mechanics. The identification of material properties and the calibration and model verification methods will be fully explored and maximised to ensure that the model is efficient and precise in describing material behaviour.

## 1.2 Aim and objectives of the study

This particular study aims to describe an attempt at modelling damage with ductile behaviour. The model employs plasticity considerations from rate-independent plasticity principles to account for ductility of the material. For lower strain-rates such as those observed in laboratory testing procedures of individual and downscaled members, and in natural loading situations of structures, the rate-independent plasticity considerations apply well [26].

Hence, this study aims to model the ductile stress-strain behaviour and load-carrying capacity discrepancies in damaged materials and members using finite deformation concepts. Furthermore, this research hinges on pre-existing physics and mechanical concepts adopted for use in a complex and unique material mechanics framework called SESKA, developed in-house at the University of Cape Town (UCT).

Furthermore, within the Polar Engineering Research Group (PERG) at UCT, the study of material damage is proceeding via computation-based research and this study proceeds to contribute to that. The overarching aim of the study is to implement a material damage model, therefore, it contains some objectives that are part of the whole aim of the study:

- Develop an understanding of the continuum mechanics of non-linear physical phenomena, and understanding the concepts of material damage theory and



how the two aforementioned subjects combine to form continuum damage mechanics.

- Build a constitutive theory of finite elastoplasticity, using the logarithmic strain to characterise strains in the elastic regime and using *von Mises* plasticity to characterise material behaviour beyond the yield point. Material damage concepts are then used to characterise damage phenomena.
- Computational implementation of a *Lemaitre*-based elastoplastic-damage model. Whereby equations may be drawn from those developed by Lemaitre [22] to characterise local damage, and leaning on the smeared damage concepts outlined in [13] and [4] to visualise macroscopic damage. This implementation will be done in SESKA using C++.
- Perform mock tests of the implemented model, by running simulations in SESKA.

### 1.3 Scope and limitations

The scope of this research is limited to the use of continuum mechanics and material damage theory, as well as rate-independent plasticity theory concepts to build a computational material model to be implemented in an in-house software.

The entire study is based on computer simulation as it is a computation-based research topic. All computations and simulations were planned to be performed on a local computer, with 16 GB RAM, and an 8-core Intel® Core™ i7 processor – which was previously sufficient computing power for small to medium-scale simulations as per the content of this study. However, the University of Cape Town High Performance Computing (UCT HPC<sup>2</sup>) facilitated for faster simulations and the potential for large-scale simulations.

As this research is entirely based on computational modelling, it hinges on consolidation from various sources of literature and scientific direction to fulfil the objectives of the study. Sources of information are fully referenced, cited and accredited. Lastly, all work done as part of this study is set to build upon the wealth of knowledge and tools that are used in observing, characterising and predicting the physical behaviour of materials under applied load.

---

<sup>2</sup>UCT maintains a high performance computing facility available to university researchers, and private/public sector researchers as well. <http://hpc.uct.ac.za/>

## 1.4 Layout of this document

Chapter 1 of this document provides an introduction to the topic of damage, aligned with research that came precedent to this one. Chapter 2 provides the mathematics of non-linear continuum mechanics, where plasticity or damage phenomena are not discussed in detail, rather discussed is the manner in which continuum mechanics is used to describe deformation and motion of continuous solids in general.

Furthermore, Chapter 3 attempts to provide a primer to material damage theory, and serves as a literature review on this material damage implementation. It is based on non-linear continuum mechanics with thermodynamic considerations made for the damage phenomena studied throughout this research. Chapter 4 outlines the detailed, model-specific mechanics, phenomenological evolution laws, constitutive equations as well as provides the thermodynamic formulations and associated flow rule that leads to the phenomenological evolution laws within this framework.

Following from the aforementioned chapters is Chapter 5, which is the section of this document that concerns the methodology: outlining the numerical methods such as the algorithmic implementations and the parametric update scheme of damage, hardening, and plasticity phenomena. Chapter 6 presents the results of simulations ran with the implemented model and Chapter 7 outlines the discussions of the results and the implementation alike.

Lastly, Chapter 8 refers to some to some conclusions and future work plans. This is the entire description of the content of this thesis document. Throughout this research, the implemented model is referred to as the "material damage model".

# Chapter 2

## Non-linear continuum mechanics theory

### 2.1 Introduction

All continuous matter, as is the case with all materials that will be modelled using the proposed material damage model outlined in this paper, is comprised of molecules bound together by microscopic bonds — the nature of these bonds depends on the particular chemistry of the atoms that form the molecules and the mechanical behaviour of the subatomic particles that are contained as part of the fundamental structure of the atoms therein. This is a physical fact, and is utilised to analyse material behaviour at the microscopic scale. However, for applied engineering applications, the burden falls on the use of a continuum mechanical approach — whereby the mechanical behaviour of materials is modelled assuming continuity in the spread of particles throughout the material volume. This rather than qualifying and quantifying mechanical behaviour by focusing on each discrete molecule/atom in the material structure. Therefore, by this continuum mechanics approach, the material is assumed to be continuous and mathematical descriptions established as a consequence of this apply everywhere in the material body. Moreover, the continuum approach allows for a frame-independent overview of the physical properties and thus, behaviour of a material on the mesoscale and microscale.

The study of continuum mechanics, and the study of materials using this method, employs several aspects that are fundamental to determining a suitable mathematical description of the material's mesoscopic phenomena. First is *kinematics*, which entails the study of the motion and deformation of a body in any spatial reference frame and in time [14]. The second is *stress*, and the study and description of forces acting within a continuous material body. Lastly are the balance equations, which are fundamental laws of physics such as the *balance of momentum*, *balance of mass*, *energy conservation*, and *irreversibility of entropy production* principles that govern the motion and deformation of the material body [18] — in particular the 1<sup>st</sup> and 2<sup>nd</sup> *laws of thermodynamics*. From the appropriate application of these concepts is derived the thermo-mechanical constitutive equations required to describe the continuum, and the solutions that evaluate the material or continuum mechanical phenomena.

It must be noted that for the entirety of this description, the three-dimensional *Euclidean* vector space is used as the spatial reference frame, denoted as  $\mathbb{E}(3)$ . The term deformation will be used to refer to all manner of deformation and motion of the continuum: shape change, orientation change and spatial translation.

Any continuum whose mass  $m$  interacts with energy, either by dissipating mechanical work done by externally applied or internal body loads, may be classed in this paper as a *thermodynamic continuum*, *thermo-mechanic continuum*, *continuum*, *material* or *material body/volume*. All these terms are interchangeable. Furthermore, this study assumes that mechanical processes are isothermal and involve no heat supply (heat flux) or temperature changes — the only thermodynamic effects observed are those that arise from the mechanical phenomena.

Lastly, in other literature, the identity matrix in mathematics and mechanics applications is termed as  $\mathbf{1}$ ; for this paper, the identity matrix is termed  $\mathbf{I}$ . Therefore,  $\mathbf{1}$  is an all-ones matrix. Essentially, the two are defined as

$$\mathbf{I} = \mathbf{1}(\mathbf{e}_i \otimes \mathbf{e}_j) \quad (2.1)$$

$$\mathbf{1} = \mathbf{1}(\mathbf{e}_i \otimes \mathbf{e}_i). \quad (2.2)$$

## 2.2 Continuum configurations

From the adoption of the continuum approach, it is evident that a suitable theory is required whereby the configurations of the continuum or material are defined [29]. These configurations represent the state of a material at any point in time for which its physical quantities may be observed or recorded. If it is assumed that any material body  $\mathcal{B}$  has a continuous distribution of matter and mass in any reference frame in space and in time, then it can be postulated that the material is completely comprised of a continuously non-discrete set of material points  $P \in \mathcal{B}$  [14]. These material points contain several particles in the locality of the material point but are not inherently small enough to be analysed with the discrete approach.

Considering that the continuum is a three-dimensional material body,  $\mathcal{B}$  in the *Euclidean* vector space  $\mathbb{E}(3)$  at a fixed instance of time  $t_0$ . A material reference frame composed of orthonormal basis vectors  $\mathbf{e}_i$ ,  $i = [1, 2, 3]$  with an origin point  $O$  may be used to describe the position of each material point in the continuum — shown in Figure 2.1. Any reference state of the continuum at time  $t = 0$ , is known as the *material/reference configuration*. If any motion or deformation is

imposed on the material from its reference state, with time having elapsed to a time  $t$ , then it can be expected that the continuum then holds a different spatial position relative to its reference configuration. Consequently, every material point now occupies a continuous spatial point or region in space, the collection of these spatial regions is known as the *deformed/current configuration* of the material body [19].

It follows that there may be infinitely many deformed configurations of the material, only discernible by their exact corresponding reference in time  $t$ . Each material point  $P \in \mathcal{B}$  is represented by position vector  $\mathbf{X} = X_i \mathbf{e}_i$  in the reference configuration and by spatial coordinate vectors  $\mathbf{x} = x_i \mathbf{e}_i$  in the deformed configuration with  $i = [1, 2, 3]$  as per the  $\mathbb{E}(3)$ .

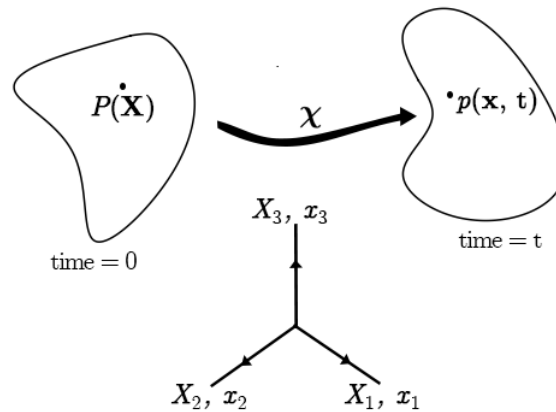


**Figure 2.1:** Configurations of a continuum under deformation [14]. The reference configuration defines the continuum  $\mathcal{B}$  at time  $t = 0$ , whilst the current configuration defines the continuum at time  $t$ .  $P = P(\mathbf{X})$  and  $p = P(\mathbf{x}, t)$ .

## 2.3 Kinematics

### 2.3.1 Differentiation of quantities

We consider an arbitrary, but smooth tensorial quantity  $\mathbf{W}$  in providing the fundamental differentiation concepts for tensor fields in the study of continuum mechanics and in this study overall. We also consider an arbitrary vector  $\mathbf{w}$  to provide the same context but for vector fields. With all concepts discussed in this section, the time derivatives, gradient fields and divergence fields are all derived with respect to each continuum configuration.

### 2.3.1.1 Time derivatives

We postulate that the tensor  $\mathbf{W}$  has derivatives defined in the current configuration as  $\dot{\mathbf{W}}_t$  and in the reference configuration as  $\dot{\mathbf{W}}_0$ , its *material time derivative* is expressed as

$$\dot{\mathbf{W}}_0 = \frac{D\mathbf{W}}{Dt} \quad (2.3)$$

for which the material position  $\mathbf{X}$  is held fixed as the field quantity changes with time [14]. Similarly, for vector fields such as  $\mathbf{w}$

$$\dot{\mathbf{w}}_0 = \frac{D\mathbf{w}}{Dt}. \quad (2.4)$$

The spatial time derivative is defined as the rate of change of a field with respect to time while the spatial position  $\mathbf{x}$  is held fixed. This leads to the following expressions for the spatial time derivative of vectors and tensors:

$$\dot{\mathbf{W}}_t = \frac{d\mathbf{W}}{dt} \quad (2.5)$$

$$\dot{\mathbf{w}}_t = \frac{d\mathbf{w}}{dt} \quad (2.6)$$

### 2.3.1.2 Gradient operator

In contrast to the time derivative, the gradient is interpreted as being the partial derivative of the tensor/vector field with respect to the position it holds in whichever description of the continuum —  $\mathbf{X}$  for the material description and  $\mathbf{x}$  for the spatial description. Importantly, time is considered constant. Thus, we define the *material gradient field* as

$$\text{Grad}(\mathbf{W}) = \frac{\partial \mathbf{W}}{\partial \mathbf{X}} \quad (2.7)$$

$$\text{Grad}(\mathbf{w}) = \frac{\partial \mathbf{w}}{\partial \mathbf{X}}. \quad (2.8)$$

The *spatial gradient field* is expressed as

$$\text{Grad}(\mathbf{W}) = \frac{\partial \mathbf{W}}{\partial \mathbf{x}} \quad (2.9)$$

$$\text{Grad}(\mathbf{w}) = \frac{\partial \mathbf{w}}{\partial \mathbf{x}}. \quad (2.10)$$

### 2.3.1.3 Divergence

The divergence quantifies the outward flux vector field  $\mathbf{w}$  at a point — with the assumption of that the vector field is the source of that outward flux. It also quantifies the flux density of the source of any arbitrary Tensor field  $\mathbf{W}$ . It reduces the order of the field by 1 [38], thus a tensor field reduces to a vector field and a vector field reduces to a scalar field. Divergence is defined in the reference configuration as

$$\text{Div}(\mathbf{W}) = \text{Grad}(\mathbf{W}) : \mathbf{I} \quad (2.11)$$

$$\text{Div}(\mathbf{w}) = \text{Grad}(\mathbf{w}) : \mathbf{I} \quad (2.12)$$

termed the *material divergence*. Furthermore, it is expressed in the current configuration as the *spatial divergence*

$$\text{Div}(\mathbf{W}) = \text{grad}(\mathbf{W}) : \mathbf{I} \quad (2.13)$$

$$\text{Div}(\mathbf{w}) = \text{grad}(\mathbf{w}) : \mathbf{I} \quad (2.14)$$

## 2.3.2 Deformation gradient

From Figure 2.2 it is evident that the deformation denoted by  $\chi$  maps the material point  $P \in \mathcal{B}_0$  in the reference configuration onto its corresponding spatial position in the deformed configuration  $P \in \mathcal{B}_t$  —  $\chi : \mathcal{B}_0 \rightarrow \mathcal{B}_t$ . Therefore

$$\mathbf{x} = \chi(\mathbf{X}, t). \quad (2.15)$$

Furthermore, the deformation  $\chi$  is uniquely invertible [14]. The inverse motion is one that returns the current configuration to its previous reference configuration.

$$\mathbf{X} = \chi^{-1}(\mathbf{x}, t). \quad (2.16)$$

Consider an infinitesimal line  $d\mathbf{X}$  between a point  $P$  and  $Q$  in the reference state of the continuum  $\mathcal{B}_0$ . It is mapped onto a corresponding line  $d\mathbf{x}$  in  $\mathcal{B}_t$  by the deformation  $\chi$  — there exists an invertible tangent map such that  $d\mathbf{x} = \text{Grad}(\chi) d\mathbf{X}$ . We introduce a quantity called the deformation gradient  $\mathbf{F}$ , which is the primary measure of deformation in continuum mechanics, and it is such it maintains the invertible tangent map of the deformation:

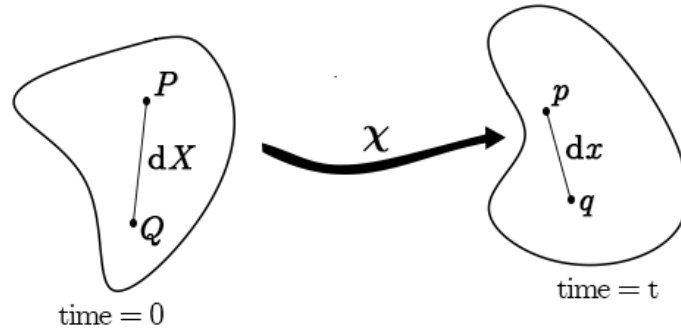


**Figure 2.2:** Deformation of the continuum with deformation of  $\chi$ . The reference configuration defines the continuum  $\mathcal{B}$  at time  $t = 0$ , whilst the current configuration defines the continuum at time  $t$ .  $P = P(\mathbf{X})$ ,  $p = P(\mathbf{x}, t)$  and  $Q = Q(\mathbf{X})$ ,  $q = Q(\mathbf{x}, t)$ .

$$\mathbf{F} = \text{Grad}(\chi) = \frac{d\mathbf{x}}{d\mathbf{X}} \quad (2.17)$$

In fact, continuum motion/deformation is described by the deformation gradient — a representation of the change of spatial position with respect to each material particle position in the continuous medium. In the vector space  $\mathbb{E}(3)$  used for this paper and the model presented later on,  $\mathbf{F}$  is a  $2^{nd}$  order tensor which characterises the deformation of the continuum for each material point. Lastly, the Jacobian describes a relative change in volume between the reference and current configurations such that

$$J = \frac{dv}{dV} \quad (2.18)$$

$$J = \det(\mathbf{F}). \quad (2.19)$$

Finally, the following identity exists for the deformation gradient tensor:

$$\mathbf{F}\mathbf{F}^{-1} = \mathbf{I}. \quad (2.20)$$

### 2.3.3 Strain tensors

The right *Cauchy-Green* tensor  $\mathbf{C}$  is often utilised in continuum mechanics applications to characterise material strain. It is a symmetric tensor composed of the deformation gradient tensor  $\mathbf{F}$  and is important in characterising strain in the material configuration (reference configuration) [14]. For each point  $P \in \mathcal{B}_0$ , whereby  $\mathcal{B}_0$  is the reference configuration of the continuum, the symmetric right *Cauchy-Green* tensor  $\mathbf{C}$  is defined as



$$\mathbf{C} = \mathbf{F}^T \mathbf{F}. \quad (2.21)$$

$\mathbf{C}$  is a  $2^{nd}$  order tensor, and is positive-definite — all the *eigenvalues* of  $\mathbf{C}$  are positive. It is possible to define the right *Cauchy-Green* tensor as composed by its symmetric right stretch tensor  $\mathbf{U}$  [19] as

$$\mathbf{C} = \mathbf{U}^2. \quad (2.22)$$

From [11] and Eq. (2.21), it is also possible to state that

$$\det(\mathbf{C}) = \det(\mathbf{F})^2 = J^2. \quad (2.23)$$

### 2.3.4 Strain-rate tensors

The rate of deformation is vital in studying deformation with respect to time evolution. For any deformation  $\boldsymbol{\chi}$ , there may be an associated translation, rotation or change in dimensions of the material body.

In the deformed configuration, the *spatial velocity gradient* tensor  $\mathbf{l}$  is a physical quantity of the continuum related to the rate of change of deformation around spatial points  $P \in \mathcal{B}_t$ . This is defined as

$$\mathbf{l} = \frac{\partial}{\partial t} \left( \frac{\partial \boldsymbol{\chi}}{\partial \mathbf{x}} \right) = \frac{\partial}{\partial \mathbf{x}} \left( \frac{\partial \boldsymbol{\chi}}{\partial t} \right) \quad (2.24)$$

$$\mathbf{l} = \frac{\partial \mathbf{v}}{\partial \mathbf{x}} = \text{grad}(\mathbf{v}) \quad (2.25)$$

whereby  $\mathbf{v} = \mathbf{v}(\mathbf{x}, t)$  is the *spatial velocity vector*.

For the reference configuration, the *material velocity gradient* tensor  $\mathbf{L}$  is also known as the *strain-rate* tensor throughout this study. It describes the rate of change of deformation of the continuum around a point  $P \in \mathcal{B}_0$ . From [38], the *material velocity gradient/strain-rate* tensor is defined as

$$\mathbf{L} = \frac{\partial \mathbf{v}_0}{\partial \mathbf{X}} = \text{Grad}(\mathbf{v}_0), \quad (2.26)$$

whereby throughout this study,  $\mathbf{v}_0 = \mathbf{v}(\mathbf{X})$  is the *material velocity vector*. Finally, this means that the *material time derivative* of the deformation gradient  $\mathbf{F}$  may also be shown as a tensor constructed with the *strain-rate* tensor or spatial velocity gradient:

$$\dot{\mathbf{F}} = (\mathbf{1F}) = (\mathbf{FL}). \quad (2.27)$$

It is noted that the *material velocity gradient* is interpreted as being a pull-back operation on the *spatial velocity gradient*, i.e if  $f : \mathbf{L} \rightarrow \mathbf{l}$  then  $f^{-1} : \mathbf{l} \rightarrow \mathbf{L}$ .

## 2.4 Stress concepts

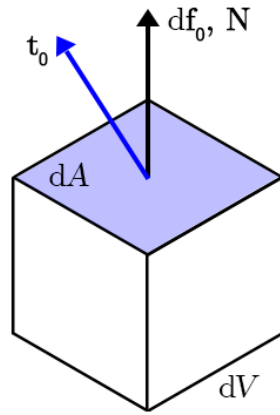


**Figure 2.3:** Schematic representation of 3D infinitesimal stress block showing the external force vector and the surface traction vector.

If one may consider an arbitrary forcing action (force)  $\mathbf{f}_0 = \mathbf{f}(\mathbf{X})$  acting on a three-dimensional infinitesimal stress block  $\mathcal{B}_0$  with volume  $dV$  and over a plane surface area  $dA$ , then the force causes stress in the block which may be visualised as being defined in infinitely many orientations in the  $\mathbb{E}(3)$  space. This is shown in Figure 2.3. However, for every point  $P \in \mathcal{B}_0$ , the arbitrary forces are represented by the differential force vector  $d\mathbf{f}_0$ . Surface traction is considered as the force acting per unit surface area [14], thus for every local point the infinitesimal stress block the *Piola-Kirchhoff* traction vector  $\mathbf{t}_0$  is defined as

$$\mathbf{t}_0 = \frac{d\mathbf{f}_0}{dA}. \quad (2.28)$$

The *Cauchy* traction vector may be split into two main components on the tangential plane to the surface of the block — normal traction,  $\mathbf{t}_{0,n}$  and shear traction,  $\mathbf{t}_{0,s}$  [18]. Furthermore, there must exist a unique  $2^{nd}$  order tensor  $\mathbf{P}$  in the reference configuration that captures information about the three-dimensional stress state in the material, such that it relates to the surface traction and the normal vector  $\mathbf{N}$  as

$$\mathbf{t}_0 = \mathbf{P}\mathbf{N}. \quad (2.29)$$

The 2<sup>nd</sup> order tensor  $\mathbf{P}$  the 1<sup>st</sup> Piola-Kirchhoff stress tensor, and it defines any three-dimensional internal stress state in the deformed configuration in relation to the reference volume. Furthermore, there are several other stress measures that are utilised in describing the internal stress response of the continuum namely the 2<sup>nd</sup> Piola-Kirchhoff stress  $\mathbf{S}$  [29]. The 2<sup>nd</sup> Piola-Kirchhoff stress defines any three-dimensional internal stress state in the reference configuration in relation to the reference volume. After tensorial analysis, the following relation(s) hold for the aforementioned stress tensors:

$$\mathbf{P} = \mathbf{F}\mathbf{S}. \quad (2.30)$$

## 2.5 Balance and conservation equations

The balance equations in the solid mechanics context of this study are tied to the conservation of mass, and momentum, and energy for each point  $P \in (\mathcal{B}_0, \mathcal{B}_t)$ . Given the material body is considered as being continuous, then the fundamental physical properties such as mass and volume follow in similar suit. Furthermore, the system that contains the continuum is considered a closed system as there is no mass supply. The balance equations are summarised as below and are adapted from various literature: [14], [47] in [29]. The balance equations apply for any part/local point in a continuum body, which is considered a closed system in these formulations, unless stated otherwise.

### 2.5.1 Balance of mass

The *law of conservation of mass* in physics states that for any closed system, the mass of the system may not change as time evolves. Essentially, "mass cannot be destroyed or created" for as long as the physical description of such mass  $m$  is non-relativistic [14]. For a closed system, the continuum body  $\mathcal{B}_t \in \mathbb{E}(3)$  that constitutes that system is assumed to have mass  $m$  at any point in time  $t$ . The continuum is defined as a collection of spatial points  $P \in \mathcal{B}_t$ , thus the continuum mass quantity may be defined as

$$m = \int_{\mathcal{B}_t} \rho(\mathbf{x}, t) dv \quad (2.31)$$

whereby  $v$  is the deformed volume of the continuum, and  $\rho_t$  is the deformed density of a point  $P \in \mathcal{B}_t$  with spatial coordinates  $\mathbf{x}$  at time  $t$  such that

$$\rho_t = \rho(\mathbf{x}, t). \quad (2.32)$$

It is established that mass is conserved, consequently, this means there is zero flux of matter in or out at any point on the boundary surface  $\partial\mathcal{B}$  on the continuum body in either the reference or deformed configurations [47]. Hence the material time derivative of  $m$  is

$$\dot{m} = \frac{Dm}{Dt} = \frac{D}{Dt} \int_{\mathcal{B}_t} \rho_t(\mathbf{x}, t) dv = 0. \quad (2.33)$$

This relation holds at every point in the continuum at all times. It is thus the *global* form of the mass balance in the deformed configuration as mass is a conserved quantity. The mass in the reference configuration, time  $t = 0$  is defined as

$$m = \int_{\mathcal{B}_0} \rho_0 dV, \quad (2.34)$$

whereby the density term  $\rho_0$  represents the density of a material point  $P$  with coordinates  $X$  at time  $t = 0$  such that

$$\rho_0 = \rho(\mathbf{X}). \quad (2.35)$$

We have established for a closed system without mass supply, mass is conserved under deformation/motion. Therefore, the following relation holds

$$\int_{\mathcal{B}_t} \rho_t dv = \int_{\mathcal{B}_0} \rho_0 dV. \quad (2.36)$$

From the definition of the deformation gradient in Section 2.3.2, it is seen that the reference and deformed volume are related as

$$dv = J dV \quad (2.37)$$

for a continuum undergoing deformation of  $\chi : \mathcal{B}_0 \rightarrow \mathcal{B}_t$ . Therefore, using Eq. (2.36), it is possible to deduct that

$$\int_{\mathcal{B}_0} [\rho_t J dV - \rho_0 dV] = 0, \quad (2.38)$$

which is the *global* form of the continuity mass equation — it represents the conservation of mass in the continuum in the material description [29]. Thus it is possible to obtain the *local* form of the *continuity mass equation* from an arbitrary domain in the continuum as

$$\rho_t J = \rho_0, \quad (2.39)$$

whereby  $J = \det(\mathbf{F}) > 0$ .

## 2.5.2 Balance of linear momentum

We consider a material body in the reference state,  $\mathcal{B}_0$ , undergoing deformation  $\chi_0$  — the deformation is caused by a combination of an external force  $\mathbf{f}_0$  and internal body force  $\mathbf{b}_0 = \mathbf{b}(\mathbf{X})$ . This material body has an arbitrary boundary surface  $\partial\mathcal{B}_0$  with an arbitrary but continuous distribution of material points on the boundary surface [14]. If an external force  $\mathbf{f}_0$  acts upon  $\partial\mathcal{B}_0$ , then it is clear that this may be represented by the aforementioned *Piola-Kirchhoff* traction vector  $\mathbf{t}_0$  (Section 2.4). Thus the total force  $\mathbf{f}$  acting on the material body may be represented as

$$\mathbf{f} = \int_{\mathcal{B}_0} \mathbf{b}_0 \, dV + \int_{\partial\mathcal{B}_0} \mathbf{t}_0 \, dA, \quad (2.40)$$

whereby  $dA$  is the differential area in the reference configuration. The material body  $\mathcal{B}_0$  is a closed system, and under deformation, each material point holds a velocity represented by the *material velocity vector*  $\mathbf{v}_0 = \mathbf{v}(\mathbf{X})$ . Thus, the total linear momentum  $\mathbf{p}$  in the continuum at time  $t = 0$  is defined as

$$\mathbf{p} = \int_{\mathcal{B}_0} \rho_0 \mathbf{v}_0 \, dV. \quad (2.41)$$

The *law of conservation of linear momentum* states that "If the net external force acting on a system of bodies is zero, then the momentum of the system remains constant". In [14], it is postulated that the rate change of momentum is equal to the total/resultant force acting on  $\mathcal{B}_t \mid t \in [0, \dots, t]$ . As per the notation introduced in this paper, this is

$$\dot{\mathbf{p}} = \mathbf{f}. \quad (2.42)$$

The left-hand side is a time derivative, and in the material description this will be considered the material time derivative of the total linear momentum  $\mathbf{p}$ . In conjunction, Eq. (2.40) and Eq. (2.41) are fed into Eq. (2.42) and it expands into the following integral form

$$\frac{D}{Dt} \int_{\mathcal{B}_0} \rho_0 \mathbf{v}_0 \, dV = \int_{\mathcal{B}_0} \mathbf{b}_0 \, dV + \int_{\partial\mathcal{B}_0} \mathbf{t}_0 \, dA. \quad (2.43)$$

For the traction term on the right-hand side in Eq. (2.43), it is possible to replace the *Piola-Kirchhoff* traction vector with a term containing the 2<sup>nd</sup> *Piola-Kirchhoff* stress tensor:-

$$\int_{\partial\mathcal{B}_0} \mathbf{t}_0 \, dA = \int_{\partial\mathcal{B}_0} \mathbf{F}\mathbf{S}\mathbf{N} \, dA, \quad (2.44)$$

whereby  $\mathbf{N}$  is the normal vector to any arbitrary boundary surface  $\partial\mathcal{B}_0$  that bounds the continuum body in its reference state. Use of the *divergence theorem* is employed to reach a final form for the traction term as

$$\int_{\partial\mathcal{B}_0} \mathbf{t}_0 \, dA = \int_{\mathcal{B}_0} \text{Div}(\mathbf{F}\mathbf{S}) \, dV. \quad (2.45)$$

For the rate change of linear momentum term on the left-hand side in Eq. (2.43), the following relations are true:-

$$\frac{D}{Dt} \int_{\mathcal{B}_0} \rho_0 \mathbf{v}_0 \, dV = \int_{\mathcal{B}_0} \rho_0 \dot{\mathbf{v}}_0 \, dV. \quad (2.46)$$

Using these derived relations, and Eq. (2.43), the integral form of the momentum balance requirement equation breaks down to

$$\int_{\mathcal{B}_0} \rho_0 \dot{\mathbf{v}}_0 \, dV = \int_{\mathcal{B}_0} [\mathbf{b}_0 + \text{Div}(\mathbf{F}\mathbf{S})] \, dV \quad (2.47)$$

$$\rightarrow \int_{\mathcal{B}_0} [\rho_0 \dot{\mathbf{v}}_0 - \mathbf{b}_0 - \text{Div}(\mathbf{F}\mathbf{S})] \, dV = 0, \quad (2.48)$$

where  $\dot{\mathbf{v}}_0 = \dot{\mathbf{v}}(\mathbf{X})$ . Thus, the local form of the linear momentum balance equation in the reference configuration is

$$\text{Div}(\mathbf{F}\mathbf{S}) + \mathbf{b}_0 = \rho_0 \dot{\mathbf{v}}_0, \quad (2.49)$$

which is also known as the *equation of motion* [29]. The acceleration field is often negligible and thus the equation of motion may be written as

$$\text{Div}(\mathbf{F}\mathbf{S}) + \mathbf{b}_0 = 0. \quad (2.50)$$

### 2.5.3 Balance of rotational momentum

Rotational momentum  $\mathbf{J}$  is the moment of the angular (rotational) momentum, it is defined as the cross product of the linear momentum,  $\mathbf{p}$  and the position vector

$\mathbf{x}$  of a point  $P \in \mathcal{B}_0$ . This quantity is considered to be conserved in a closed system. The rate of change of angular momentum is required to equal the sum of torque actions (turning moments) in the continuum, which is

$$\dot{\mathbf{J}} = \mathbf{M} \quad (2.51)$$

whereby the rate of change of rotational momentum  $\dot{\mathbf{J}}$  is the material time derivative of the total rotational momentum contained by the continuum at time  $t = t$  in the current configuration:

$$\dot{\mathbf{J}} = \frac{D}{Dt} \int_{\mathcal{B}_t} \mathbf{x} \times \rho(\mathbf{x}, t) \mathbf{v}(\mathbf{x}, t) dv \quad (2.52)$$

which, if taken for the material configuration, is then of the integral form as follows:

$$\dot{\mathbf{J}} = \frac{D}{Dt} \int_{\mathcal{B}_0} \mathbf{x} \times \rho_0 \mathbf{v}_0 dV, \quad (2.53)$$

$$\rightarrow \dot{\mathbf{J}} = \int_{\mathcal{B}_0} \mathbf{x} \times \rho_0 \frac{D\mathbf{v}_0}{Dt} dV. \quad (2.54)$$

$$\rightarrow \dot{\mathbf{J}} = \int_{\mathcal{B}_0} \mathbf{x} \times \rho_0 \dot{\mathbf{v}}_0 dV. \quad (2.55)$$

The total moment acting on the continuum is evaluated as the rotational equivalent of applied force  $\mathbf{f}$ , which in the reference configuration is

$$\mathbf{M} = \int_{\partial\mathcal{B}_0} \mathbf{x} \times \mathbf{t}_0 dA_0 + \int_{V_0} \mathbf{x} \times \mathbf{b}_0 dV_0. \quad (2.56)$$

$\mathbf{b}_0 = \mathbf{b}(\mathbf{X})$  is the reference body force and  $\mathbf{t}_0$  is the *Piola-Kirchhoff* traction vector. When working in the reference configuration, it is often that either the 1<sup>st</sup> or 2<sup>nd</sup> *Piola-Kirchhoff* stress tensor is used to store information about the material's stress response. Thereby the traction term in Eq. (2.56) becomes

$$\int_{\partial\mathcal{B}_0} \mathbf{x} \times \mathbf{t}_0 dA = \int_{\mathcal{B}_0} \mathbf{x} \times \text{Div}(\mathbf{FS}) dV + \int_{\mathcal{B}_0} \boldsymbol{\epsilon} : (\mathbf{FS})^T dV, \quad (2.57)$$

whereby  $\boldsymbol{\epsilon}$  is the *permutation tensor* - i.e  $\mathbf{x} \times \mathbf{t}_0 = \epsilon_{ijk} x_i(t_0)_j \mathbf{e}_k$ . Thus, the equation for the total moment  $\mathbf{M}$  is

$$\mathbf{M} = \int_{\mathcal{B}_0} [(\mathbf{x} \times [\text{Div}(\mathbf{FS}) + \mathbf{b}_0]) + \boldsymbol{\epsilon} : (\mathbf{FS})^T] dV. \quad (2.58)$$

The final form of the balance equation  $\dot{\mathbf{J}} = \mathbf{M}$  may be obtained for the reference configuration which, when relativistic effects are ignored as is the scope of this work, may not have a non zero volume, thus

$$\int_{\mathcal{B}_0} \mathbf{x} \times [\text{Div}(\mathbf{FS}) + \mathbf{b}_0 - \rho_0 \dot{\mathbf{v}}_0] dV = \int_{\mathcal{B}_0} \boldsymbol{\epsilon} : (\mathbf{FS})^T dV, \quad (2.59)$$

which is the actual integral form of the *balance of rotational momentum* equation. By analysing the *equation of motion* from Section 2.5.2, one can obtain

$$\text{Div}(\mathbf{FS}) + \mathbf{b}_0 - \rho_0 \dot{\mathbf{v}}_0 = 0. \quad (2.60)$$

From this, it is evident that both sides of the integral form of the *balance of rotational momentum* equation in Eq. (2.59) equate to 0. Which leads to the following condition for the right-hand side of that equation

$$\int_{\mathcal{B}_t} \boldsymbol{\epsilon} : (\mathbf{FS})^T dV = 0 \quad (2.61)$$

$$\rightarrow \boldsymbol{\epsilon} : (\mathbf{FS})^T = 0. \quad (2.62)$$

Some identities for the *Piola-Kirchhoff* stress measures follow directly from Eq. (2.62):

$$(\mathbf{FS})^T = \mathbf{S}^T \mathbf{F}^T, \quad (2.63)$$

which gives

$$\mathbf{S} = \mathbf{S}^T. \quad (2.64)$$

The 2<sup>nd</sup> *Piola-Kirchhoff* stress measure is crucial in this study as will be seen later in this document.

## 2.5.4 Balance of mechanical energy

The *law of conservation of energy* states that "the total energy of an isolated system is conserved over time, energy may be converted from one form to another but may not be created nor destroyed". Initially, the material body  $\mathcal{B}_0$  undergoing a deformation  $\boldsymbol{\chi}$  from its reference state to its deformed state is considered once again. This material body in the reference configuration has an arbitrary collection of particles that form an arbitrary boundary surface  $\partial\mathcal{B}_0$  on the material body.



To balance the mechanical energy in the continuum body, the amount of external work  $\mathcal{W}_{ext}$  introduced to the continuum must equate to the amount of work absorbed and converted to internal energy during the deformation  $\boldsymbol{\chi}$  — internal energy  $e = e(\mathbf{C})$ . Thus the balance of mechanical energy may be represented mathematically:

$$e = \mathcal{W}_{ext}. \quad (2.65)$$

As the deformation of the continuum occurs over time  $t \in [0, \dots, t]$ , it is more suitable to define the balance of mechanical energy principles in terms of work done per unit time (power) as

$$\dot{\mathcal{K}} + \mathcal{P}_{int} = \mathcal{P}_{ext}, \quad (2.66)$$

whereby  $\mathcal{P}_{int}$  introduces the internal mechanical power and  $\mathcal{P}_{ext}$  are external power. The time rate of change of the kinetic energy, given as  $\dot{\mathcal{K}}$  in Eq. (2.66), is simply the material time derivative of the kinetic energy when considered in the material configuration, which is the entire basis of this study. Thus,

$$\dot{\mathcal{K}} = \frac{D\mathcal{K}}{Dt}. \quad (2.67)$$

Furthermore, the integral form of  $\mathcal{K}$  may be described from the principles of thermodynamics, in that the kinetic energy is a product of the mass and velocity of a point/particle in a material. Thus, for the continuum  $\mathcal{B}_0$  with material velocity field  $\mathbf{v}_0 = \mathbf{v}(\mathbf{X})$ , the material time derivative of the kinetic energy is

$$\frac{D\mathcal{K}}{Dt} = \frac{D}{Dt} \int_{\mathcal{B}_0} \frac{1}{2} \rho_0 \mathbf{v}_0^2 \, dV, \quad (2.68)$$

and may also be shown as

$$\dot{\mathcal{K}} = \frac{D}{Dt} \int_{\mathcal{B}_0} \rho_0 \left( \frac{1}{2} \mathbf{v}_0 \cdot \mathbf{v}_0 \right) \, dV. \quad (2.69)$$

According to [38], the internal mechanical power term  $\mathcal{P}_{int}$  is the stress power. The stress power is consequent of work done to induce stress in the material body. The 2<sup>nd</sup> Piola-Kirchhoff stress tensor is used in the formulation of the stress power as in Eq. (2.70) —

$$\mathcal{P}_{int} = \int_{\mathcal{B}_0} \mathbf{FS} : \dot{\mathbf{F}} \, dV. \quad (2.70)$$

The external mechanical power  $\mathcal{P}_{ext}$  is combination of the work produced by the internal body forces  $\mathbf{b}_0 = \mathbf{b}(\mathbf{X})$ , and the work produced from the external applied force on the arbitrary boundary surfaces to the continuum, envisioned by the *Piola-Kirchhoff* traction vector  $\mathbf{t}_0$ . It is thus defined according to [27] as

$$\mathcal{P}_{ext}(t) = \int_{\partial\mathcal{B}_0} \mathbf{t}_0 \cdot \mathbf{v}_0 \, dA + \int_{\mathcal{B}_0} \mathbf{b}_0 \cdot \mathbf{v}_0 \, dV. \quad (2.71)$$

Therefore, the integral form of the mechanical energy balance equation in the material description, also known as the *1<sup>st</sup> law of thermodynamics* is

$$\begin{aligned} \frac{D}{Dt} \int_{\mathcal{B}_0} \rho_0 \left( \frac{1}{2} \mathbf{v}_0 \cdot \mathbf{v}_0 \right) \, dV + \int_{\mathcal{B}_0} \mathbf{FS} : \dot{\mathbf{F}} \, dV \\ = \int_{\partial\mathcal{B}_0} \mathbf{t}_0 \cdot \mathbf{v}_0 \, dA + \int_{\mathcal{B}_0} \mathbf{b}_0 \cdot \mathbf{v}_0 \, dV. \end{aligned} \quad (2.72)$$

### 2.5.5 Balance of thermal energy

In order to derive an entropy-related inequality in the proceeding sections (such as to not reverse the production of entropy in a continuum), the derivation of balance equations for conservation of thermal energy is important. As entropy is a thermal concept, we describe the *balance of thermal energy* from the *1<sup>st</sup> law of thermodynamics* as being

$$\rho_0 \dot{e} = \mathcal{P}_{int} + \mathcal{Q}, \quad (2.73)$$

in which  $\dot{e}$  is the material rate of the internal energy and  $\mathcal{P}_{int}$  is defined as the stress power and  $\mathcal{Q}$  as the thermal power.  $\mathcal{P}_{int}$  has its global form defined in Eq. (2.70), but takes the following pointwise form:

$$\mathcal{P}_{int} = \mathbf{FS} : \dot{\mathbf{F}}. \quad (2.74)$$

We define the global form of the thermal power in the material configuration as

$$\mathcal{Q} = \int_{\partial\mathcal{B}_0} Q_N \, dA + \int_{\mathcal{B}_0} \dot{Q} \, dV, \quad (2.75)$$

whereby  $Q_N$  is a scalar function of the heat flux through an arbitrary boundary surface on the material body, and  $\dot{Q}$  denotes the *rate of heat supply* term (heat supply per unit time). *Stoke's heat flux theorem* provides that the scalar function  $Q_N$  is

$$Q_N = -\mathbf{Q} \cdot \mathbf{N}, \quad (2.76)$$

for which  $\mathbf{N}$  is the outward facing unit normal from an arbitrary boundary surface  $\partial\mathcal{B}_0$  and  $\mathbf{Q} = \mathbf{Q}(\mathbf{X})$  — the *Piola-Kirchhoff* heat flux vector [14]. Thus Eq. (2.75) is

$$\mathcal{Q} = - \int_{\partial\mathcal{B}_0} \mathbf{Q} \cdot \mathbf{N} \, dA + \int_{\mathcal{B}_0} \dot{Q} \, dV. \quad (2.77)$$

The *divergence theorem* is employed on the heat flux term and thus the thermal power takes the form

$$\mathcal{Q} = \int_{\mathcal{B}_0} \left[ \dot{Q} - \text{Div}(\mathbf{Q}) \right] \, dV, \quad (2.78)$$

which may then be expressed in the local form as

$$\mathcal{Q} = \dot{Q} - \text{Div}(\mathbf{Q}). \quad (2.79)$$

It is then possible to derive a local form for the balance of thermal energy as postulated in Eq. (2.73) as

$$\rho_0 \dot{e} = \mathbf{FS} : \dot{\mathbf{F}} + \dot{Q} - \text{Div}(\mathbf{Q}). \quad (2.80)$$

### 2.5.6 Irreversibility of entropy production

Mathematically, if there exists a state of the material such that any arbitrary material point  $P \in \mathcal{B}_0$  at time  $t = 0$  has a pointwise entropy density of  $\vartheta_0 = \vartheta(\mathbf{X})$  and its corresponding spatial point  $P \in \mathcal{B}_t$  has a pointwise entropy density of  $\vartheta_t = \vartheta(\mathbf{x}, t)$ , then the entropy held by a material point is

$$\eta = \vartheta_0. \quad (2.81)$$

Therefore, the material rate change of entropy is

$$\dot{\eta} = \frac{D\eta}{Dt} \quad (2.82)$$

from the definition of the material time derivative of a quantity (see Section 2.3.1.1). The *2<sup>nd</sup> law of thermodynamics* states that the material rate change of entropy relates to the material rate supply of entropy  $\tilde{Q} = \tilde{Q}(\mathbf{X})$  as

$$\dot{\eta} \geq \tilde{\mathcal{Q}}. \quad (2.83)$$

We define the global form of the material rate supply of entropy as being composed of the *Piola-Kirchhoff* entropy flux  $\mathbf{H} = \mathbf{H}(\mathbf{X})$  and the entropy supply per unit time  $\dot{\tilde{\mathcal{Q}}}$ :

$$\tilde{\mathcal{Q}} = - \int_{\partial \mathcal{B}_0} \mathbf{H} \cdot \mathbf{N} \, dA + \int_{\mathcal{B}_0} \dot{\tilde{\mathcal{Q}}} \, dV. \quad (2.84)$$

Furthermore, in the thermodynamics of solid bodies, it is common knowledge that

$$\dot{\tilde{\mathcal{Q}}} = \frac{\dot{\mathcal{Q}}}{\Theta}, \quad (2.85)$$

and

$$\mathbf{H} = \frac{\mathbf{Q}}{\Theta}, \quad (2.86)$$

in which  $\mathbf{Q}$ ,  $\dot{\mathcal{Q}}$  were described in Section 2.5.5 and  $\Theta = \Theta(\mathbf{X})$  is the smooth absolute temperature function of each material point. Thus, it is also straightforward to visualise the corollary between the material rate supply of entropy  $\tilde{\mathcal{Q}}$  and the thermal power  $\mathcal{Q}$  (Eq. (2.79)) as

$$\tilde{\mathcal{Q}} = \frac{\mathcal{Q}}{\Theta}. \quad (2.87)$$

It is understood that for purely mechanical isothermal processes,  $\Theta$  is a constant scalar function. thus we define the local form of the material rate supply of entropy:

$$\tilde{\mathcal{Q}} = \frac{1}{\Theta} \left[ \dot{\mathcal{Q}} - \text{Div}(\mathbf{Q}) \right]. \quad (2.88)$$

Therefore, the *2<sup>nd</sup> law of thermodynamics* decomposes to

$$\dot{\eta} \geq \frac{1}{\Theta} \left[ \dot{\mathcal{Q}} - \text{Div}(\mathbf{Q}) \right]. \quad (2.89)$$

Due to the nature of elastoplastic deformations in a continuum, elastic deformations do not produce entropy over time (constant temperature, heat flux and heat supply). Inelastic deformations produce entropy via dissipation and this production of entropy is irreversible. Thus, the entropy held at any point in a continuum becomes a combination of the reversible  $\eta_{rev}$  and inelastic  $\eta_{pl}$  forms

$$\eta = \eta_{el} + \eta_{pl}, \quad (2.90)$$

where

$$\dot{\eta}_{el} = \frac{1}{\Theta} \left[ \dot{Q} - \text{Div}(\mathbf{Q}) \right] \quad (2.91)$$

is true and this indicates that

$$\dot{\eta}_{pl} \geq 0. \quad (2.92)$$

The 1<sup>st</sup> law of thermodynamics is also represented in terms of the entropy as

$$\rho_0 \dot{e} = \mathbf{FS} : \dot{\mathbf{F}} + \Theta \dot{\eta}. \quad (2.93)$$

We apply a *Legendre* transformation on the rate of internal energy  $\dot{e}$  and this introduces the *Helmholtz* free-energy function  $\Psi$ :

$$\rho_0 \Psi_{int} = \rho_0 e - \Theta \eta, \quad (2.94)$$

whereby  $\Psi_{int} = \Psi_{int}(\mathbf{C}, \eta)$  is the local (pointwise) internal potential. In continuum mechanics and in this study, the *Helmholtz* free-energy function is utilised to quantise the useful work obtainable in a continuum body [47]. Taking the material time derivative of both sides of Eq. (2.94) yields

$$\rho_0 \dot{\Psi}_{int} = \rho_0 (\dot{e} - \dot{\Theta} \eta - \Theta \dot{\eta}), \quad (2.95)$$

if for an isothermal process  $\dot{\Theta} = 0$ , then

$$\rho_0 \dot{\Psi}_{int} = \mathbf{FS} : \dot{\mathbf{F}} + \Theta \dot{\eta} - \Theta \dot{\eta}, \quad (2.96)$$

which provides the local form of the *dissipation inequality* as

$$\eta_{pl} = \mathbf{FS} : \dot{\mathbf{F}} - \rho_0 \dot{\Psi}_{int} \geq 0. \quad (2.97)$$

Since all dissipative mechanisms are in the inelastic regime of deformation, then we generalise the entropy inequality as the *dissipation inequality*  $\mathcal{D}$  as follows:

$$\mathcal{D} = \mathbf{FS} : \dot{\mathbf{F}} - \rho_0 \dot{\Psi}_{int} \geq 0. \quad (2.98)$$

This holds for mechanical processes — the stress term is the internal *stress power*  $\mathcal{P}_{int}$  and the  $\dot{\Psi}_{int}$  term represents the sum of non-mechanical forms of internal power.

# Chapter 3

## Material damage theory

### 3.1 Damage phenomenology

Damage is the progressive creation and growth of micro-defects at the microscale of a continuum (material body). These micro-defects nucleate as networks of cracks and form discontinuities that manifest themselves as cracks growing at the macroscale. This is the microscopic to macroscopic onset of material damage. Notably, Lemaitre [24] identifies several mechanisms by which microscale damage may occur in several types of materials: damage in polymers occurs when long-chain bonds are broken and damage in concrete occurs whereby decohesion between the aggregate and the cement matrix or by creation of micro-voids in the solid cement matrix. Damage in ductile materials occurs by large deformation effects which cause instability in the vicinity of crystalline defects and dislocations [23].

However, the basis of this study is the mesoscale to macroscale damage progression, where the microscopic discontinuities nucleate to initiate local discontinuities (mesoscale discontinuities) which then evolve to form macro-cracks by growth and networking of the local cracks under load/deformation. This is the idea of smeared damage – local discontinuities that represent the local damaged state of material points are then smeared over the volume containing those particles.

Furthermore, damage as a mechanical concept reduces the load-carrying capacity of a point or collection of points in the material volume, as will be shown in Section 3.3. The phenomena of damage is dissipative and thermodynamically irreversible, and damage thereby is related to plasticity. In analysing irreversible thermodynamic processes, there is a requirement for thermodynamic state variables (state variables), which define the present state of any corresponding physical mechanism and the thermodynamic state potential, which defines the state of the process itself and is essential in defining the energetic variables associated with the state variables [24]. The energetic variables are important in characterizing the manner in which energy is dissipated in the continuum. Outlined in the following sections are the essential concepts involved in describing material damage.

### 3.2 Isotropic damage variable

From the definition of material damage, it is observed that damage is inherently linked to the micro-structural configuration of a continuum — whereby bonds are broken to form dislocations and these dislocations grow irreversibly to form cracks [23]. For any two-dimensional surface  $\delta A_S$  within which there exists micro-voids and micro-cracks, the cumulative quantity of all micro-cracks and micro-voids is assumed to be the combined surface area  $\delta A_{S,M}$  of the intersections of all these flaws in the continuum as shown in Figure 3.1.

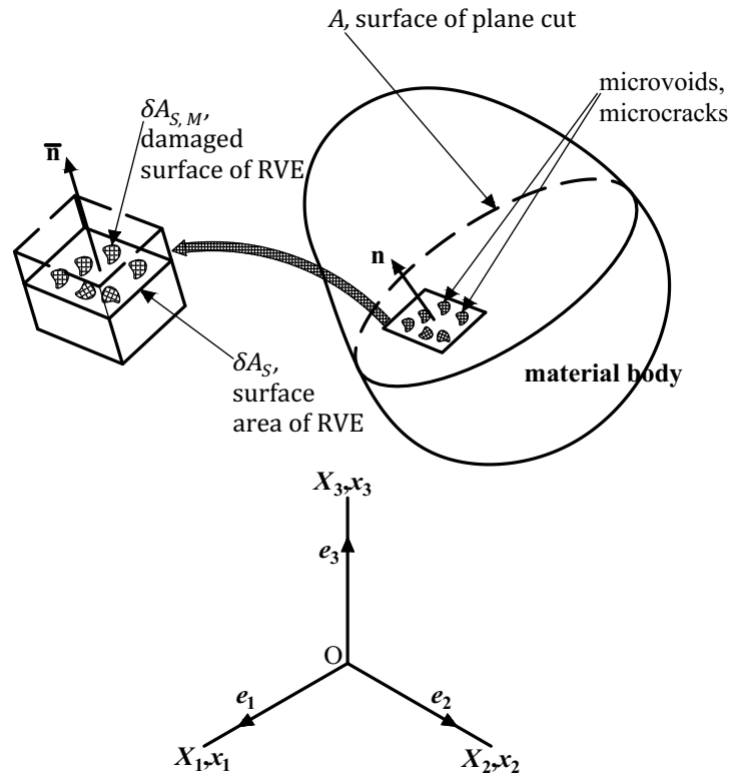


**Figure 3.1:** Material damage theory represented in a material body. Showing microvoid presence [24].

Therefore, the three-dimensional extrapolation of this concept in the continuum  $\mathcal{B}_0$  is that the combined volume of micro-defects constitutes the cumulative quantity of all micro-defects [25]. This is similar to the theory of plasticity, in which the plastic strain is a representation of the accumulated irreversible deformation in the material.

For any plane that cuts through the material continuum  $\mathcal{B}_0$  as shown in Figure 3.1, there exists an area swept through by the plane (the cross-sectional) area  $\delta A_S$  and an effective surface area of the micro-defects  $\delta A_{S,M}$ . The total volume of micro-voids is the integration of micro-defect surface area throughout the entire

continuum volume  $V$  [23]. Consequently, an isotropic damage variable  $M$  is introduced in Eq. (3.1) and Eq. (3.2).  $M$  is a local quantity that represents the ratio of the cumulative quantity of micro-defects to the undamaged quantity of matter.

$$M = \frac{\delta A_{S,M}}{\delta A_S} \rightarrow \frac{A_M}{A} \quad (3.1)$$

$$M = \frac{V_M}{V}. \quad (3.2)$$

If the entirety of the volume is occupied by micro-cracks, then the material continuum is said to be cracked at the macroscale,  $M = 1$ . Furthermore, at the mesoscale, local material points may be cracked if they assume the value of  $M = 1$  before macroscopic damage occurs. In fact, it is most likely that the mesoscale cracking occurs before macroscopic cracking through the smeared approach. However, the opposite of this is the scenario whereby  $M = 0$ , and no damage has occurred. Therefore, the physical mechanism of damage is bound by these limits

$$0 \leq M \leq 1. \quad (3.3)$$

The state of internal fracture in the continuum may be described by an arbitrary value  $M_{cr}$ , which is the cracking limit for different materials, especially for ductile materials for which cracking may occur at lower values of the damage variable  $M$ . The behaviour of the material after the point of failure is outside the scope of this study.

### 3.3 Effective stress concept

The constitutive relations between stress and strain from elasticity theory, make use of the elastic modulus and *Poisson's* ratio, which are material properties that govern the internal stress response to applied loads/deformation. In plasticity theory, the strain and stress are related by way of the *yield criteria* — detailed in Section 4.7. The concept of stress in a continuum was described in Section 2.4, where the *Piola-Kirchhoff* traction vector for any surface in a continuum body  $\mathcal{B}_0$  is

$$\mathbf{t}_0 = \frac{\mathbf{f}_0}{A} \quad (3.4)$$

$$\rightarrow \mathbf{t}_0 = \mathbf{PN}, \quad (3.5)$$



whereby the relation between the 1<sup>st</sup> and 2<sup>nd</sup> Piola-Kirchhoff stress:  $\mathbf{FS} = \mathbf{P}$  hold, such that

$$\mathbf{t}_0 = \mathbf{FSN}. \quad (3.6)$$

The continuum in this case is a square block as in Figure 3.2, which has an applied force  $\mathbf{f}_0$  that causes the traction on the model.

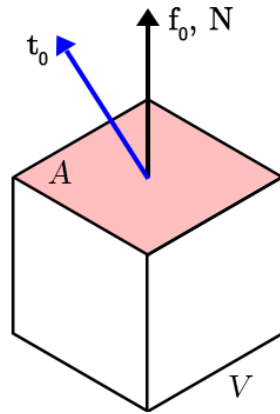


**Figure 3.2:** Schematic representation of a loaded square block showing the external force vector and the surface traction vector.

The isotropic damage variable  $M$  stores approximate information about the quantity of discontinuities with respect to the entire continuum. Therefore, if there exists any micro-voids  $A_M$  in the material — the effective load-carrying area is reduced to  $(A - A_M)$ . The effective surface traction is related to this effective load-carrying area as

$$\tilde{\mathbf{t}}_0 = \frac{\mathbf{f}_0}{A - A_M} \quad (3.7)$$

then

$$\tilde{\mathbf{t}}_0 = \frac{\mathbf{f}_0}{A \left(1 - \frac{A_M}{A}\right)}, \quad (3.8)$$

the term  $A_M/A$  is the definition of the isotropic damage variable  $M$ . Thus,

$$\tilde{\mathbf{t}}_0 = \frac{\mathbf{t}_0}{1 - M} \quad (3.9)$$

which is the effective normal traction. Thus, any stress measure is scaled by the same quotient  $1/(1 - M)$  to produce the "effective" measure of stress, as the damage variable is isotropic. This is the case in tension and in compression for a material without the micro-defect closure effect. Thus

$$\tilde{\mathbf{t}}_0 = \tilde{\mathbf{P}}\mathbf{N} \quad (3.10)$$

holds for damaged materials, which provides the effective 1<sup>st</sup> and 2<sup>nd</sup> *Piola-Kirchhoff* stress measures as shown below. These stress measures will be shown to be vital in this study:

$$\tilde{\mathbf{P}} = \frac{\mathbf{P}}{1 - M}, \quad (3.11)$$

$$\tilde{\mathbf{S}} = \frac{\mathbf{S}}{1 - M}. \quad (3.12)$$

Micro-defect closure occurs in brittle materials, whereby the effective load carrying area is increased by the the compressive nature of the loading [25] and is represented by scaling down the magnitude of the damage variable in compression. In fact, the phenomenon allows for recovery of part of the the elastic stiffness of the material under compression [24]. However, this is outside the scope of this current study and is not explored throughout this paper.

### 3.4 Thermodynamic potential & dissipation potential

In the context of this study, the *Helmholtz free-energy function* applies as the thermodynamic state potential, as it defines the thermodynamic state of a system in isothermal processes — the state potential quantises the energy in the system in deforming a material body regardless of the path of the deformation.

The dissipation potential follows from the principle of *irreversibility of entropy production* in mechanical processes, this was introduced well in Section 2.5.6. This section serves to introduce these thermodynamic quantities but greater mathematical detail is provided in Section 4.

#### 3.4.1 *Helmholtz free-energy function*

The *Helmholtz free-energy function* is denoted as  $\Psi$ , is a physical quantity that measures and/or describes the total potential (useful work) — the capacity of

conservative forces to do non-mechanical and mechanical work in isothermal deformation of a continuum. Essentially, it is the combination of all contributions to the internal non-mechanical potential of a continuum and the mechanical work contributions by externally applied actions. Mathematically, the total potential is of the sum of internal non-mechanical forms  $\Psi_{int}$ , and the external potential  $\Psi^*$

$$\Psi = \Psi_{int} + \Psi^*, \quad (3.13)$$

where  $\Psi^*$  is the external potential, assumed *nil*. The internal potential,  $\Psi_{int}$ , is related to elastic energy stored and energy associated with work done to facilitate for damage and work hardening in the material body. Thus, it may also be decomposed into the elastic stored energy and the energy associated with irreversible phenomena. In this case, damage is coupled as it affects elasticity via the effective stress concept and degrades the elastic modulus, and is coupled to the work-hardening term as well as

$$\Psi_{int} = \Psi_{int}(\mathbf{C}_{el}, M) + \Psi_{int}(Z, M). \quad (3.14)$$

When damage evolution is decoupled from plastic behaviour, then damage and work hardening terms in Eq. (3.14) are represented independently. Therefore the the total non-mechanical work forms are represented as

$$\Psi_{int} = \Psi_{int}(\mathbf{C}_{el}) + \Psi_{int}(Z) + \Psi_{int}(M). \quad (3.15)$$

Here,  $\mathbf{C}_{el}$  is the elastic right *Cauchy-Green* deformation,  $M$  is the local damage variable and  $Z$  is the local isotropic hardening variable which will be expanded when further thermodynamic descriptions in pertinence to this study are shown in Chapter 4. The *Helmholtz free-energy function* will be used as the thermodynamic state potential throughout this paper.

### 3.4.2 Entropy and dissipation

The concept of irreversibility of entropy production directly lead onto the *dissipation inequality*, which plays an important role in formulating constitutive relations. In isothermal mechanical processes, the temperature is always locally and statically defined, thereby dissipation is the energy converted to heat and other entropy producing forms at a certain temperature by irreversible deformations. The *dissipation inequality* defines the potential for dissipation. This was introduced in Section 2.5.6 for generalised continua as

$$\mathcal{D} = \mathbf{F}\mathbf{S} : \dot{\mathbf{F}} - \rho_0 \dot{\Psi}_{int} \geq 0. \quad (3.16)$$

Therefore, from Eq. (3.15) — with  $\mathcal{P}_{int}$  being the stress power:

$$\mathcal{D} = \mathcal{P}_{int} - \rho_0 \left( \dot{\Psi}_{int}(\mathbf{E}_{el}M) + \dot{\Psi}_{int}(Z) + \dot{\Psi}_{int}(M) \right). \quad (3.17)$$

Essentially, this is the actual dissipation inequality function of a mechanical process including local damage and work hardening. It may be interpreted physically as the difference between the internal stress power (due to inducing a stress response in the material), captured by the  $\mathcal{P}_{int}$  term in this case, and the power dissipated by dissipative mechanisms.

Further details on dissipation are provided in Section 4.5 — where the full context of the proposed model (the terms and variables used in formulating the model) is taken into account.

# Chapter 4

## Modelling local elastoplastic-damage

### 4.1 The general approach

The model follows directly from the concepts of non-linear continuum mechanics (Chapter 2), and material damage theory (Chapter 3). In continuum mechanics, any material body is assumed continuous throughout its volume, and its material points assumed to be distributed in a homogeneous manner. Material damage theory employs the use of an isotropic damage variable  $M$  to characterise the gradual loss of load-carrying capacity due to progressive damage in a material continuum.

This framework uses the *Lagrangian* approach, which indicates that all constitutive formulations are applied on a continuum in its reference configurations,  $\mathcal{B}_0$ . Using the deformed configuration would require the use of re-meshing techniques in the finite element framework. The *Lagrangian* approach initialises by discretising a local material point  $P \in \mathcal{B}_0$  in the reference configuration and defines all *internal state variables* and their *associated energetic variables* forthwith. The scale is known as the mesoscale [23].

It must be mentioned that this constitutive framework stores deformation information in the right *Cauchy-Green* tensor  $\mathbf{C}$  which - the *Lagrangian* approach. This is work-conjugate to the 2<sup>nd</sup> *Piola-Kirchhoff* stress tensor  $\mathbf{S}$  [38]. It is observable that

$$\mathcal{P}_{int} = \mathbf{P} : \dot{\mathbf{F}} = \mathbf{S} : \frac{1}{2}\dot{\mathbf{C}}. \quad (4.1)$$

The primary objective of this study is to model damage in an isothermal context, therefore all thermodynamic balance equations are considered at static temperature. This being the case, the model description will commence with a summary of its thermodynamic state variables, then proceeds from there to describe the constitutive relations and mechanics of the model.

## 4.2 Large deformation elastoplasticity

Large deformation elastoplasticity follows from the kinematics defined in Section 2.3. Large deformation elastoplasticity suitably accounts for deformations in a wide scope of applications: from small-strain applications where minimal shape change or length changes are observed, to large deformation situations such as those seen in laboratory material strength testing. Furthermore, large deformation elastoplasticity accounts for plastic (irreversible) deformations by employing a plastic portion for the finite deformation quantities such as the deformation gradient,  $\mathbf{F}$ , the right *Cauchy-Green* tensor  $\mathbf{C}$ , and the *strain-rate* tensor  $\mathbf{L}$  [26].

### 4.2.1 Multiplicative decomposition of deformation gradient

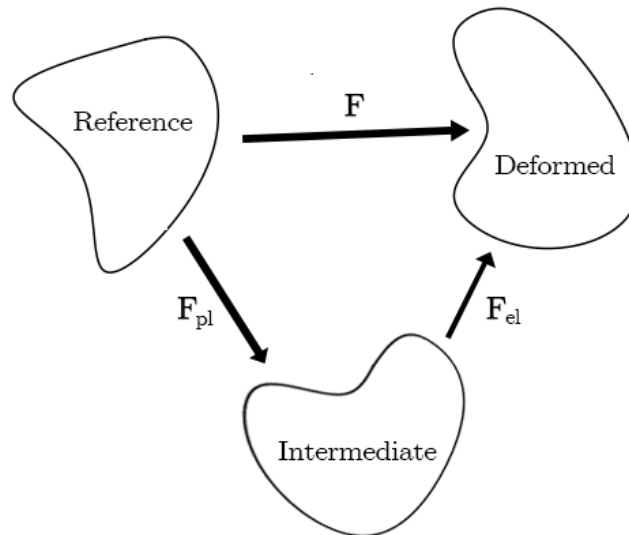


**Figure 4.1:** Schematic diagram showing the multiplicative decomposition of deformation gradient  $\mathbf{F}$ . The intermediate configuration shows the split between elasticity and plasticity.

The deformation gradient  $\mathbf{F}$  characterises the local material deformation of a point in a continuum. In generalised elastoplasticity theory, the deformation must consist of both an elastic response to stress and a inelastic portion [26]. For small-strain deformation,  $\mathbf{F}$  is additively decomposed:

$$\mathbf{F} = \mathbf{F}_{el} + \mathbf{F}_{pl}. \quad (4.2)$$

However, damage and cracking of a material typically involves large deformations. Therefore, the the simple assumption of additive decomposition of the deformation quantities is abandoned for a multiplicatively decomposed deformation gradient:

$$\mathbf{F} = \mathbf{F}_{el}\mathbf{F}_{pl}. \quad (4.3)$$

The inelastic portion  $\mathbf{F}_{pl}$  is intrinsic to the configurations for which the deformation is being characterised i.e. the deformed/reference configurations of the material. Furthermore, the inelastic portion captures damage and plasticity. In Figure 4.1, the intermediate configuration represents a stress-free state of the material. Further mathematical relations pertaining to deformation gradient are summarised as follows for the elastic portion:

$$\dot{\mathbf{F}}_{el}\mathbf{F}_{el}^{-1} + \mathbf{F}_{el}\dot{\mathbf{F}}_{el}^{-1} = \mathbf{0} \quad (4.4)$$

then, for the plastic portion:

$$\dot{\mathbf{F}}_{pl}\mathbf{F}_{pl}^{-1} + \mathbf{F}_{pl}\dot{\mathbf{F}}_{pl}^{-1} = \mathbf{0}, \quad (4.5)$$

whereby in all both these equations, the following important relations also hold as per the definition of the *strain-rate* tensor  $\mathbf{L}$  in Section 2.3.4 -

$$\dot{\mathbf{F}}^{-1} = -\mathbf{L}\mathbf{F}^{-1}. \quad (4.6)$$

#### 4.2.2 Cauchy-Green strain

The right *Cauchy-Green* tensor  $\mathbf{C}$  is essential for this theory. It describes the strain in the reference configuration, and thus can be used in conjunction with the 2<sup>nd</sup> *Piola-Kirchhoff* stress tensor  $\mathbf{S}$ , which is also defined in the material configuration. In Eq. (2.21),  $\mathbf{C} = \mathbf{F}^T\mathbf{F}$  holds and this breaks down to

$$\mathbf{C} = \mathbf{F}_{pl}^T\mathbf{F}_{el}^T\mathbf{F}_{el}\mathbf{F}_{pl} \quad (4.7)$$

$$\rightarrow \mathbf{C} = \mathbf{F}_{pl}^T\mathbf{C}_{el}\mathbf{F}_{pl}, \quad (4.8)$$

which follows from derivations by Lubliner [26]. From Eq. (2.21), the following relations also hold:

$$\mathbf{C}_{el} = \mathbf{F}_{el}^T\mathbf{F}_{el} \quad (4.9)$$

$$\mathbf{C}_{pl} = \mathbf{F}_{pl}^T\mathbf{F}_{pl}. \quad (4.10)$$

### 4.2.3 Plastic *strain-rate*

In finite strain kinematics, the *strain-rate* is recorded in the *material velocity gradient* tensor  $\mathbf{L}$ . this tensor is defined in the reference configuration,  $\mathcal{B}_0$ . The total *strain-rate* tensor decomposes into the elastic and plastic portions as follows:

$$\mathbf{L} = \mathbf{L}_{el} + \mathbf{F}_{el} \mathbf{L}_{pl} \mathbf{F}_{el}^{-1} \quad (4.11)$$

It is consequent that that the plastic *strain-rate* tensor,  $\mathbf{L}_{pl}$  is related to the to the total *strain-rate*,  $\mathbf{L}$  as

$$\mathbf{L} = \mathbf{L}_{el} + \mathbf{F}_{el} \mathbf{L}_{pl} \mathbf{F}_{el}^{-1}, \quad (4.12)$$

It also follows that the following relations also apply as a consequence of Eq. (2.26):

$$\mathbf{L}_{el} = \mathbf{F}_{el}^{-1} \dot{\mathbf{F}}_{el} \quad (4.13)$$

$$\mathbf{L}_{pl} = \mathbf{F}_{pl}^{-1} \dot{\mathbf{F}}_{pl}. \quad (4.14)$$

## 4.3 *Mandel* stress measure

In this section, the thermodynamics of the stress response to deformation are discussed in order to qualify the concepts of stress in the elastoplastic-damage application of this study. Firstly, a stress measure known as the *Mandel* stress, denoted  $\Sigma$  is introduced such that it is conjugate to the total *strain-rate* tensor  $\mathbf{L}$  [28]. This stress tensor is defined with respect to an intermediate configuration and is not symmetric, unlike the 2<sup>nd</sup> *Piola-Kirchhoff* stress tensor.

The *strain-rate* tensor  $\mathbf{L}$  is critical to this study, as it the state variable used to characterise deformation with respect to time. In fact, the mechanical stress power  $\mathcal{P}^{int}$  in a continuum undergoing forced deformation over any time interval  $t \in [0, \dots, t]$  may be expressed in terms of  $\Sigma$  and  $\mathbf{L}$  as

$$\mathcal{P}_{int} = \Sigma : \mathbf{L}, \quad (4.15)$$

This will be proven in the proceeding equations. Using Eq. (2.26), where  $\mathbf{L} = \mathbf{F}^{-1} \dot{\mathbf{F}}$ , the mechanical stress power is of the form

$$\mathcal{P}_{int} = \Sigma : \mathbf{F}^{-1} \dot{\mathbf{F}} = \mathbf{F}^{-T} \Sigma : \dot{\mathbf{F}}. \quad (4.16)$$



This is similar to the stress power term introduced in Section 2.5 using the 2<sup>nd</sup> *Piola-Kirchhoff* stress tensor:

$$\mathcal{P}_{int} = \mathbf{F}^{-T} \boldsymbol{\Sigma} : \dot{\mathbf{F}} = \mathbf{F} \mathbf{S} : \dot{\mathbf{F}}, \quad (4.17)$$

which represents the local formulations of mechanical stress power. The left-hand of the tensor double-dot product operator on both sides may be equated, hence

$$\mathbf{F}^{-T} \boldsymbol{\Sigma} = \mathbf{F} \mathbf{S} \quad (4.18)$$

holds, and when the *Mandel* stress tensor is made the subject of the equation by multiplying sides with  $\mathbf{F}^T$ , Eq. (4.18) becomes

$$\boldsymbol{\Sigma} = \mathbf{F}^T \mathbf{F} \mathbf{S}. \quad (4.19)$$

It has been established that  $\mathbf{C} = \mathbf{F}^T \mathbf{F}$  in Section 2.3.3, thus

$$\boldsymbol{\Sigma} = \mathbf{C} \mathbf{S}. \quad (4.20)$$

Finally, the *Mandel* stress tensor may be split it into the deviatoric and spherical portions (frame-invariant):

$$\boldsymbol{\Sigma} = \text{dev}(\boldsymbol{\Sigma}) + \frac{1}{3} \text{tr}(\boldsymbol{\Sigma}) \mathbf{I}, \quad (4.21)$$

this split is crucial to the composition of tensors in the algorithmic implementation of this mode discussed later in Section 5.5.

## 4.4 Thermodynamic state variables

State variables refer to the mathematical descriptions of physical quantities as observed in a continuum body  $\mathcal{B}_0$  undergoing deformation. Thus, they are in accordance with the outwardly observable and internal mechanisms of deformation. Furthermore, each state variable has a corresponding *associated energetic variable* which as a whole defines the dissipative and non-dissipative thermodynamic mechanisms taking place.

#### 4.4.1 Observed state variables

Observed state variables are measurable by physical means, whereby no extra mathematical analysis is needed beyond dimensional apportioning of the measured quantities. In the coupled isothermal analysis of either ductile damage or brittle damage, the observed variables are

- The total deformation is represented by the right *Cauchy-Green* tensor  $\mathbf{C}$ , as observed during the change of shape of the material body from one configuration to another. Change of position is captured by  $\mathbf{u}$ .
- Temperature  $\Theta$ , which for an isothermal process will not vary and is considered inconsequential for constitutive modelling purposes. However, temperature affects the internal material properties and total dissipative power of irreversible mechanisms, since they produce entropy at the current temperature.

#### 4.4.2 Internal state variables

The internal state variables are associated with a corresponding thermodynamic state potential and thermodynamic process. For instance, elasticity is a thermodynamic process that converts mechanical work into potential energy in the form of elastic stored energy. These internal state variables are as follows:

- Elastic portion of total deformation, represented by  $\mathbf{C}_{el}$  or the logarithmic (*Hencky*) strain tensor  $\boldsymbol{\alpha}$  as a result of the total stress response of the material.
- Plastic portion of total deformation, represented by  $\mathbf{C}_{pl}$  or by the *rate of plastic deformation* tensor  $\mathbf{L}_{pl}$  as a result of the plastic response of the material.
- Isotropic hardening state variable  $Z$ , associated with the yield criterion and the accumulated plastic strain  $p$  affected by the isotropic hardening mechanism during the plastic phase of the strain response.
- Isotropic damage variable  $M$ , associated with the thermo-mechanical process of damage.

#### 4.4.3 Associated energetic variables

The energetic variables are associated with the dissipative mechanisms that alter the thermodynamic state of the continuum  $\mathcal{B}_0$ . With inelastic deformations, the energetic variables deal with entropy production in that they record the rate at which the internal energy of the continuum is dissipated by material damage and other dissipative mechanisms.

- In the reference configuration, the deformation  $\mathbf{C}$ ,  $\mathbf{C}_{el}$  are in association with the total stress  $\mathbf{S}$  developed in the material,  $\mathbf{S}$  is the 2<sup>nd</sup> Piola-Kirchhoff stress.
- In the intermediate configuration, the Mandel stress  $\Sigma$  characterises stress and is associated with the inelastic phenomena — the plastic *strain-rate* tensor  $\mathbf{L}_{pl}$ .
- The isotropic hardening state variable  $Z$  is in association with the isotropic hardening potential,  $R$ .
- The damage potential, otherwise known as the damage energy density release rate  $Y$  is associated with the isotropic damage variable  $M$ . It is a stress-like variable describing the dissipation of work through damage.

## 4.5 Free-energy and dissipation

The stress power is described mathematically as

$$\mathcal{P}_{int} = \Sigma : \mathbf{L}. \quad (4.22)$$

In any case where work is done on the continuum/material by external actions, then the stress power is non-trivial —  $\mathcal{P}_{int} > 0$ . It follows from the 2<sup>nd</sup> law of thermodynamics that there exists an entropy dissipation requirement which compares the mechanical stress power to the internal free energy power. The local form of the entropy inequality principle is introduced in Section 3.4.2

$$\mathcal{D} = \mathcal{P}_{int} - \rho_0 \dot{\Psi}_{int}. \quad (4.23)$$

Substituting Eq. (4.22) into Eq. (4.23), the following is obtained:

$$\mathcal{D} = \Sigma : \mathbf{L} - \rho_0 \dot{\Psi}_{int}. \quad (4.24)$$

The dissipation potential is positive-valued i.e.  $\mathcal{D} \geq 0$ ; it follows from the principle of irreversibility of entropy that the direction of local entropy production is always positive [47]. The internal potential,  $\Psi_{int}$  comprises of the elastic stored energy and the energy associated with strain hardening and damage. The local form of the internal potential is

$$\Psi_{int} = \Psi_{int}(\mathbf{C}_{el}, M) + \Psi_{int}(Z) + \Psi_{int}(M). \quad (4.25)$$

It must be noted that since the elastic *Cauchy-Green* tensor term represents the stored elastic strain energy and is related to the elastic properties of the mate-

rial; elastic properties these are locally degraded by the isotropic damage variable  $M$ . After employing the *chain rule* on the local form of  $\Psi_{int}$ , the *material time derivative* of the internal potential function is mathematically derived as

$$\dot{\Psi}_{int} = (1 - M) \frac{\partial \Psi_{int}}{\partial \mathbf{C}_{el}} : \dot{\mathbf{C}}_{el} + \frac{\partial \Psi_{int}}{\partial Z} \cdot \dot{Z} + \frac{\partial \Psi_{int}}{\partial M} \cdot \dot{M} \quad (4.26)$$

$$\rightarrow \dot{\Psi}_{int} = 2(1 - M) \mathbf{C} \mathbf{F}_{pl}^{-1} \frac{\partial \Psi_{int}}{\partial \mathbf{C}_{el}} \mathbf{F}_{pl}^{-T} : (\mathbf{L} - \mathbf{L}_{pl}) + \frac{\partial \Psi_{int}}{\partial Z} \cdot \dot{Z} + \frac{\partial \Psi_{int}}{\partial M} \cdot \dot{M}. \quad (4.27)$$

When Eq. (4.27) is substituted into Eq. (4.24), the dissipation inequality decomposes to

$$\begin{aligned} \mathcal{D} = \boldsymbol{\Sigma} : \mathbf{L} - 2\rho_0(1 - M) \mathbf{C} \mathbf{F}_{pl}^{-1} \frac{\partial \Psi_{int}}{\partial \mathbf{C}_{el}} \mathbf{F}_{pl}^{-T} : (\mathbf{L} - \mathbf{L}_{pl}) \\ - \rho_0 \frac{\partial \Psi_{int}}{\partial Z} \cdot \dot{Z} - \rho_0 \frac{\partial \Psi_{int}}{\partial M} \cdot \dot{M} \geq 0 \end{aligned} \quad (4.28)$$

$$\begin{aligned} \rightarrow \mathcal{D} = \left( \boldsymbol{\Sigma} - 2\rho_0(1 - M) \mathbf{C} \mathbf{F}_{pl}^{-1} \frac{\partial \Psi_{int}}{\partial \mathbf{C}_{el}} \mathbf{F}_{pl}^{-T} \right) : \mathbf{L} \\ + 2\rho_0(1 - M) \mathbf{C} \mathbf{F}_{pl}^{-1} \frac{\partial \Psi_{int}}{\partial \mathbf{C}_{el}} \mathbf{F}_{pl}^{-T} : \mathbf{L}_{pl} \\ - \rho_0 \frac{\partial \Psi_{int}}{\partial Z} \cdot \dot{Z} - \rho_0 \frac{\partial \Psi_{int}}{\partial M} \cdot \dot{M} \geq 0. \end{aligned} \quad (4.29)$$

This is all extended from the dissipation relation in [40]. The evolution of plasticity, damage and elasticity are independent of each other and so are the phenomenological rate variables  $\mathbf{L}$ ,  $\dot{Z}$  and  $\dot{M}$ . Thus, the constitutive formulation of the *Mandel* stress tensor may be derived from Eq. (4.29) as

$$\boldsymbol{\Sigma} = 2\rho_0(1 - M) \mathbf{C} \mathbf{F}_{pl}^{-1} \frac{\partial \Psi_{int}}{\partial \mathbf{C}_{el}} \mathbf{F}_{pl}^{-T}, \quad (4.30)$$

and given the identity in Eq. (4.8), it is determined that

$$\mathbf{C} = \mathbf{F}_{pl}^T \mathbf{C}_{el} \mathbf{F}_{pl}, \quad (4.31)$$

$$\mathbf{C} \mathbf{F}_{pl}^{-1} = \mathbf{F}_{pl}^T \mathbf{C}_{el}. \quad (4.32)$$

This yields the following form for the constitutive formulation of  $\boldsymbol{\Sigma}$ :

$$\boldsymbol{\Sigma} = 2\rho_0(1 - M)\mathbf{F}_{pl}^T \mathbf{C}_{el} \frac{\partial \Psi_{int}}{\partial \mathbf{C}_{el}} \mathbf{F}_{pl}^{-T}. \quad (4.33)$$

This is adopted from [39]. We define the following associated thermodynamic quantities for the isotropic hardening parameter  $Z$  and isotropic damage variable  $M$  from the dissipation inequality  $\mathcal{D}$  as

$$R = -\rho_0 \frac{\partial \Psi_{int}}{\partial Z}, \quad (4.34)$$

$$Y = -\rho_0 \frac{\partial \Psi_{int}}{\partial M}, \quad (4.35)$$

respectively. From this, it is shown that the local form of the dissipation inequality function may be expressed as

$$\mathcal{D} = \boldsymbol{\Sigma} : \mathbf{L}_{pl} + R \cdot \dot{Z} + Y \cdot \dot{M} \geq 0 \quad (4.36)$$

for this material model. This will be important in establishing the *associative flow rule* and *yield criteria* later on. If each term represents different inelastic phenomena, then it may further be simplified as

$$\mathcal{D} = \mathcal{P}_{int}(\mathbf{L}_{pl}) - \dot{\Psi}_{int}(Z) - \dot{\Psi}_{int}(M) \geq 0. \quad (4.37)$$

## 4.6 Elasticity and strain

### 4.6.1 *Hencky* strain measure

The *Hencky* strain, denoted in this study as  $\boldsymbol{\alpha}$ , defined and in [12] is a logarithmic strain measure — an alternative to conventional strain measures seen in solid mechanics frameworks such as the standard linear elastic strain model where the *Green-Lagrange* strain  $\mathbf{E}$  is used. The *Hencky* logarithmic strain tensor is related closely to the elastic right *Cauchy-Green* tensor  $\mathbf{C}_{el}$  and its stretch tensor  $\mathbf{U}_{el}$ ;  $\boldsymbol{\alpha}$  is defined as

$$\boldsymbol{\alpha} = \ln(\mathbf{C}_{el}), \quad (4.38)$$

which may be expressed as a tensor composed of the logarithmic of the principal values bases of  $\mathbf{C}_{el}$ , with its principal bases being invariant to the logarithmic operation:

$$\boldsymbol{\alpha} = \sum_{i=1}^3 \ln(C_{el})_i (\mathbf{p}_i \otimes \mathbf{p}_i). \quad (4.39)$$

The opposite is also true —

$$\mathbf{C}_{el} = \exp(\boldsymbol{\alpha}), \quad (4.40)$$

$$\rightarrow \mathbf{C}_{el} = \sum_{j=1}^3 \exp(\alpha_j) (\mathbf{p}_j \otimes \mathbf{p}_j). \quad (4.41)$$

Adkins & Davidson [1] define a how matrix exponential may be expressed as a power series of the matrix exponential. That definition may be applied to the relation in Eq. (4.40) as follows:

$$\exp(\boldsymbol{\alpha}) = 1 + \boldsymbol{\alpha} + \frac{\boldsymbol{\alpha}^2}{2!} + \frac{\boldsymbol{\alpha}^3}{3!} + \dots \quad (4.42)$$

Furthermore, another important relation between the right *Cauchy-Green* tensor and the *Hencky* logarithmic strain tensor follows from the following property: "the derivative of an exponential function maintains the exponential function in each iteration of the derivative when taken with respect to its independent variable" adopted from [21]. The chain rule when applied to Eq. (4.38) yields

$$\frac{\partial \Psi_{int}(\boldsymbol{\alpha})}{\partial \boldsymbol{\alpha}} = \mathbf{C}_{el} \frac{\partial \Psi_{int}(\mathbf{C}_{el})}{\partial \mathbf{C}_{el}}. \quad (4.43)$$

The *Mandel* stress  $\boldsymbol{\Sigma}$ , as introduced in Section 4.3 and further detailed in Section 4.5 relates to the plastic deformation gradient  $\mathbf{F}_{pl}$  and the internal free energy  $\Psi_{int}$ . Furthermore, it follows from the relations in Eq. (4.43) that

$$\boldsymbol{\Sigma} = 2\rho_0(1 - M) \mathbf{F}_{pl}^T \frac{\partial \Psi_{int}(\boldsymbol{\alpha})}{\partial \boldsymbol{\alpha}} \mathbf{F}_{pl}^{-T}. \quad (4.44)$$

Using the *Hencky* logarithmic strain tensor and Eq. (4.44), the distorted *Hencky* logarithmic strain tensor,  $\bar{\boldsymbol{\alpha}}$  is defined as

$$\bar{\boldsymbol{\alpha}} = \mathbf{F}_{pl}^T \boldsymbol{\alpha} \mathbf{F}_{pl}^{-1} [39], \quad (4.45)$$

whereby the following also holds:

$$\frac{\partial \Psi_{int}(\bar{\boldsymbol{\alpha}})}{\partial \bar{\boldsymbol{\alpha}}} = \mathbf{F}_{pl}^T \frac{\partial \Psi_{int}(\boldsymbol{\alpha})}{\partial \boldsymbol{\alpha}} \mathbf{F}_{pl}^{-1}. \quad (4.46)$$

Hence, it is then derived from the identity of the *Hencky* logarithmic strain tensor in Eq. (4.40) that

$$\bar{\mathbf{C}}_{el} = \exp(\bar{\boldsymbol{\alpha}}) = \mathbf{F}_{pl}^T(\exp(\boldsymbol{\alpha}))\mathbf{F}_{pl}^{-1}, \quad (4.47)$$

and the local form of the thermodynamic relation of the *Mandel* stress and the distorted *Hencky* strain is straightforward:

$$\boldsymbol{\Sigma} = 2\rho_0(1 - M) \frac{\partial \Psi_{int}(\bar{\boldsymbol{\alpha}})}{\partial \bar{\boldsymbol{\alpha}}}. \quad (4.48)$$

$$\rightarrow \boldsymbol{\Sigma} = 2\rho_0 \frac{\partial \Psi_{int}(\bar{\boldsymbol{\alpha}}, M)}{\partial \bar{\boldsymbol{\alpha}}}. \quad (4.49)$$

#### 4.6.2 Elastic constitutive relations

The *Mandel* stress and the *Hencky* logarithmic strain are thermodynamically related as was outlined in Eq. (4.48). The mechanical constitutive relation of the *Mandel* stress and the distorted *Hencky* logarithmic strain tensor may be expressed as being

$$\boldsymbol{\Sigma} = (1 - M) [K \operatorname{tr}(\bar{\boldsymbol{\alpha}}^T)\mathbf{I} + G \operatorname{dev}(\bar{\boldsymbol{\alpha}}^T)] \quad (4.50)$$

where the material properties  $G$  and  $K$  are the shear modulus and bulk modulus respectively. This linear relation between  $\boldsymbol{\Sigma}$  and  $\bar{\boldsymbol{\alpha}}$  is chosen for computational simplicity in this isotropic damage model. The *effective Mandel* stress is defined as

$$\tilde{\boldsymbol{\Sigma}} = K \operatorname{tr}(\bar{\boldsymbol{\alpha}}^T)\mathbf{I} + G \operatorname{dev}(\bar{\boldsymbol{\alpha}}^T) \quad (4.51)$$

whereby,

$$\operatorname{dev}(\bar{\boldsymbol{\alpha}}^T) = \bar{\boldsymbol{\alpha}}^T - \frac{1}{3} \operatorname{tr}(\bar{\boldsymbol{\alpha}}^T)\mathbf{I} \quad (4.52)$$

$$\bar{\boldsymbol{\alpha}}^T = \ln(\mathbf{C}\mathbf{C}_{pl}^{-1}). \quad (4.53)$$

This was adapted from [39] and modified to incorporate local damage. However, it must be noted that the *Mandel* stress is related to the *Hencky* logarithmic strain in the intermediate configuration, which is a function the right *Cauchy-Green* tensor. These quantities are important since the model utilises the intermediate and reference configurations.

## 4.7 Plasticity and damage evolution

### 4.7.1 *von Mises* Yield criterion

The *von Mises* yield surface [45] is used for this implementation:

$$f = \frac{\sqrt{3J_2}}{1 - M} - (\sigma_y - R) \quad (4.54)$$

whereby  $\sigma_y$  is the initial yield strength, assuming material isotropy. Furthermore, the that yield strength is not specific to a particular stress regime (tensile or compressive).  $J_2$  is the 2<sup>nd</sup> invariant of the deviatoric portion of the *Mandel* stress tensor:

$$J_2 = \frac{1}{2} \|\text{dev}(\boldsymbol{\Sigma})\|^2. \quad (4.55)$$

Furthermore,  $R$  is the energetic stress-like variable associated with isotropic strain hardening, as is derived in Section 4.5.  $R$  is power conjugate to the internal isotropic hardening state variable  $Z$ . Therefore, it redefines the yield equation as

$$f = \frac{\|\text{dev}(\boldsymbol{\Sigma})\|}{1 - M} - \sqrt{\frac{2}{3}}(\sigma_y - R) \quad (4.56)$$

Notable in this yield function is how the damage associate energetic variable  $Y$  is not included in the yield criteria as it does not affect the onset of plasticity.

### 4.7.2 Damage energy density

In Section 4.5 it was discussed that the damage energy density release rate  $Y$ , which is a stress-like variable defining the rate at which mechanical work is dissipated by non-linear material damage mechanisms, is related to the internal work  $\Psi_{int}$  as

$$Y = -\rho_0 \frac{\partial \Psi_{int}}{\partial M}, \quad (4.57)$$

and for this framework, a term for  $Y$  is a decomposed formulation of the equations found in [17] and [25] — it is represented as

$$Y = \frac{\|\text{dev}(\boldsymbol{\Sigma})\|^2}{4G(1 - M)^2} + \frac{[\text{tr}(\boldsymbol{\Sigma})]^2}{2K(1 - M)^2}. \quad (4.58)$$



### 4.7.3 Non-linear isotropic hardening

Isotropic hardening represents work-hardening mechanisms in this model. The internal stress-like variable  $R$  that defines the state potential of isotropic hardening mechanisms in a material is related to the internal work  $\Psi_{int}$  as

$$R = -\rho_0 \frac{\partial \Psi_{int}}{\partial Z}, \quad (4.59)$$

For the *von Mises* yield criteria in Eq. (4.56), the non-linear exponential hardening law [46] is chosen

$$R = -HZ - (\sigma_\infty - \sigma_y) [1 - \exp(-\eta Z)], \quad (4.60)$$

where  $H$  represents the hardening modulus,  $\sigma_y$  represents the initial yield strength of the material,  $\sigma_\infty$  is the ultimate yield strength (rupture stress) and  $\eta$  is the hardening saturation parameter.

### 4.7.4 Phenomenological evolution laws

This model uses the *associative flow rule*, for which the yield function is regarded as the plastic potential and it is consequent from the concepts regarding the associative flow rule in [26] and [39] that the following relations hold:

$$\mathbf{L}_{pl} = \lambda \frac{\partial f}{\partial \boldsymbol{\Sigma}}, \quad (4.61)$$

whereby  $\lambda$  is the plastic multiplier and  $f$  represents the yield function as introduced in Section 4.7.1. This is known as the associated flow rule [26]. It corresponds to the normality rules, in that the derivative of the yield function with respect to the stress variable is the gradient vector of the yield surface, which is also the normal of that surface. Thus, the plastic *strain-rate* tensor is written as

$$\mathbf{L}_{pl} = \lambda \frac{\text{dev}(\boldsymbol{\Sigma})^T}{(1 - M) \|\text{dev}(\boldsymbol{\Sigma})\|} = \lambda \mathbf{N}^T, \quad (4.62)$$

in which  $\mathbf{N}$  is the normal to the yield surface and is known qualitatively as the *flow vector*. Furthermore, the following relations for the plastic multiplier,  $\lambda$  exist:

$$\lambda = \begin{cases} > 0 & \text{if } (f = 0) \\ = 0 & \text{if } (f < 0). \end{cases}$$

The evolution of accumulated plastic strain is defined within this framework as

$$\dot{p} = \sqrt{\frac{2}{3}} \|\mathbf{L}_{pl}\|. \quad (4.63)$$

The following *Kuhn-Tucker* loading/unloading conditions also apply in this sense as per the consistency requirements

$$\lambda \geq 0 \quad (4.64)$$

$$f \leq 0 \quad (4.65)$$

$$\lambda f = 0. \quad (4.66)$$

The consistency requirement is

$$\lambda \dot{f} = 0. \quad (4.67)$$

It follows from the the relations between the associated energetic variables and the state variables in Section 4.4 that

$$\dot{Z} = \lambda \frac{\partial f}{\partial R} = \sqrt{\frac{2}{3}} \lambda, \quad (4.68)$$

and

$$\dot{M} = \sqrt{\frac{2}{3}} \lambda \frac{1}{1-M} \left( \frac{Y}{S} \right)^s, \quad (4.69)$$

where  $s$  and  $S$  are entropy- and temperature-related parameters;  $s$  is the damage evolution law exponent — determined from experimentation but often  $s = 1$ ,  $S$  is the energetic damage law parameter — usually determined by several trial-and-error or other identification methods. However, these are considered constants as it pertains to this implementation, i.e.  $s = s_0$ ,  $S = S_0$ .

Intuitively, a material is said to undergo damage when it exhibits a loss of stress-carrying capacity, this may occur concurrently or independently to the plastic phase of material behaviour. Theoretically, the introduction of a damage variable may require a damage threshold, which is compared to the accumulated plastic strain,  $p$  such that material damage evolves upon overage of this threshold. The following definitions are of the accumulated plastic strain  $p$ , and the equivalent critical damage strain  $p_M$

$$p = \int_{t_{yield}}^t \dot{p} dt = \int_{t_{yield}}^t \sqrt{\frac{2}{3}} \|\mathbf{L}_{pl}\| dt \quad (4.70)$$

$$p_M = \epsilon_M \quad (4.71)$$

whereby  $\epsilon_M$  is the value of the critical damage strain, which is interpreted and implemented as a scalar as per the isotropic assumptions of the material behaviour in this proposed model. Thus  $p_M = \epsilon_M$ . From the same concepts, the damage evolution law is presented as per Lemaitre & Chaboche [23] and de Souza Neto et al. [5] who show that damage may only evolve if the damage strain threshold has been exceeded by the accumulated plastic strain, and only in the plastic zone as we know, thereby

$$\dot{M} = \sqrt{\frac{2}{3}} \lambda \frac{\hat{H}(p - p_M)}{1 - M} \left(\frac{Y}{S_0}\right)^{s_0} \quad (4.72)$$

whereby  $\hat{H}$  represents the *Heaviside* step function. This is a logical step in the characterisation of damage. If the accumulated plastic strain is greater than the equivalent critical damage strain (damage threshold) then the material is said to have been damaged to an extent governed by the stress-like quantity  $Y$ , and the thermo-mechanic material properties  $S_0$  and  $s_0$ . Therefore

$$\dot{M} = \sqrt{\frac{2}{3}} \lambda \frac{\hat{H}(p - p_M)}{1 - M} \left(\frac{Y}{S_0}\right)^{s_0} = \begin{cases} 0 & \text{for } p < p_M \\ \sqrt{\frac{2}{3}} \frac{\lambda}{1 - M} \left(\frac{Y}{S_0}\right)^{s_0} & \text{for } p \geq p_M \end{cases}$$

is the general damage evolution law. Furthermore, the local damage variable  $M_{sm}$  may never exceed the value of 1.0 as that would constitute mesoscale fracture [48]. However, it would be more feasible to assume that internal fracture may occur before  $M = 1.0$ , thus a material property known as the *internal critical damage threshold* otherwise known as the *cracking threshold* may be represented as  $M_{cr}$ , thus the following also holds:

$$0 < M \leq M_{cr} \quad (4.73)$$

Global fracture may occur before all local integration points in the continuum have undergone cracking, due to the interconnectivity of certain cracked points. Thus, the smeared damage value  $M_{sm}$  is also introduced to represent global damage - computed by SESKA independently as a consequence of the geometry of local integration points.

# Chapter 5

## Computational methods

### 5.1 Summary of the material damage model

Drawing from the previous chapter, where the model is introduced, the equations that describe this model are defined as below. The continuum is assumed to deform as is defined in conventional continuum mechanics as is in Chapter 2 and undergoes a combined inelastic response to applied loading, the plastic response and the damage response and the constitutive relations of the model are summarised here:

#### (i) The damage and plasticity-related thermodynamic quantities

$$Y = \frac{\|\text{dev}(\boldsymbol{\Sigma})\|^2}{4G(1-M)^2} + \frac{[\text{tr}(\boldsymbol{\Sigma})]^2}{2K(1-M)^2}$$

$$R = -HZ - (\sigma_\infty - \sigma_y) [1 - \exp(-\eta Z)].$$

#### (ii) The elastic constitutive law

$$\boldsymbol{\Sigma} = (1-M) [K \text{tr}(\bar{\boldsymbol{\alpha}}^T) \mathbf{I} + G \text{dev}(\bar{\boldsymbol{\alpha}}^T)].$$

#### (iii) Yield (damage) function

$$f = \frac{\|\text{dev}(\boldsymbol{\Sigma})\|}{1-M} - \sqrt{\frac{2}{3}} (\sigma_y - R).$$

#### (iv) Evolution equations for all state variables ( $\mathbf{L}_{pl}$ , $Z$ and $M$ )

$$\mathbf{L}_{pl} = \lambda \frac{\partial f}{\partial \boldsymbol{\Sigma}} = \lambda \frac{\text{dev}(\boldsymbol{\Sigma})^T}{(1-M)\|\text{dev}(\boldsymbol{\Sigma})\|} = \lambda \mathbf{N}^T$$

$$\dot{Z} = \lambda \frac{\partial f}{\partial R} = \sqrt{\frac{2}{3}} \lambda$$

$$\dot{M} = \sqrt{\frac{2}{3}} \lambda \frac{\hat{H}(p - p_M)}{1-M} \left( \frac{Y}{S_0} \right)^{s_0}.$$

#### (v) Consistency conditions

$$\lambda \geq 0, f \leq 0, \lambda f = 0.$$

## 5.2 The computational work-flow

The work-flow within each simulation step maybe understand as preceding as in the work-flow chart below follows:

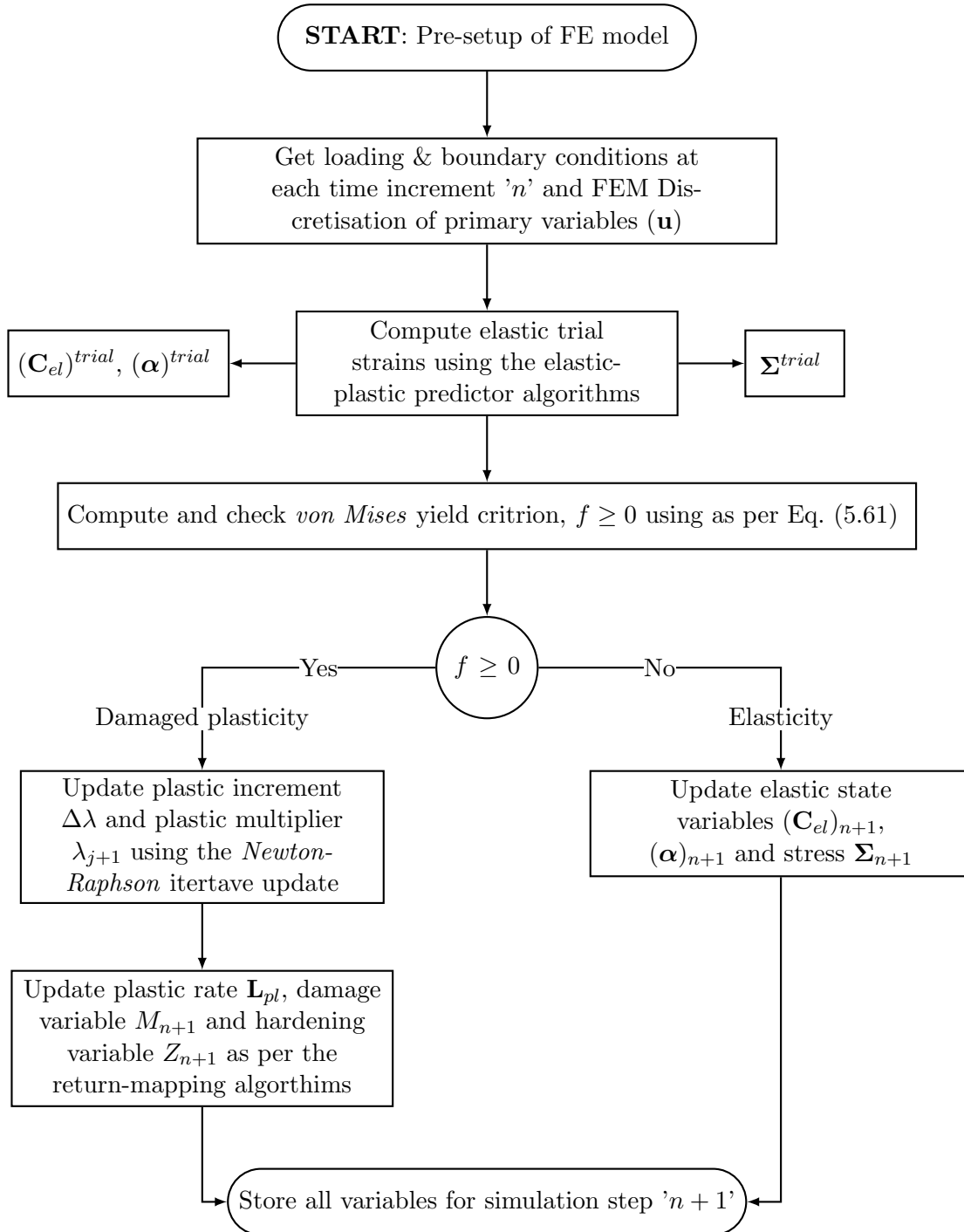


**Figure 5.1:** Work-flow chart within simulation step

## 5.3 Finite element formulations

This section will show the weak forms used in the finite element framework of SESKA. These principles are similar to those authors such as Omatuku-Ngongo [32] and Hopkins [16]. The most relevant weak form to the context of this paper is the momentum balance equation introduced in Section 2.5.3 which involves the primary kinematic fields of displacement  $\mathbf{u}$ , deformation measure  $\mathbf{F}$ , and other fields such as the *Piola-Kirchhoff* traction  $\mathbf{t}_0$  and stresses  $\mathbf{S}$ ,  $\mathbf{P}$ .

### 5.3.1 Weak form of momentum balance

In the computational sense, similar to the discussions in Section 4.2.1, the continuum/material at time  $t = 0$  is the material configuration at the start of a global simulation step  $n + 1$  and the continuum at time  $t = t$  is the current configuration at the end of the step. The intermediate configuration captures the continuum under finite elastoplastic deformation at each iteration step  $j + 1$  within a global simulation step. From the context provided in Section 2.5.2, the global form of the linear momentum balance equation for the reference continuum  $\mathcal{B}_0$  in this case, undergoing deformation  $\chi$  is

$$p_0^{global} = \int_{\mathcal{B}_{t_0}} \{ \text{Div}(\mathbf{FS}) - \mathbf{b}_{t_0} - \rho_{t_0} \dot{\mathbf{v}}_{t_0} \} dV = 0 \quad (5.1)$$

where  $dV$  represents an infinitesimal volume in the reference configuration. It must be mentioned that for purposes of structural analysis, kinematic effects are ignored and any volume changes occur gradually such that the velocity/acceleration term in Eq. (5.1) is ignored; thus  $\dot{\mathbf{v}}_{t_0} \rightarrow 0$ . The following relations also hold:

$$\mathbf{FS} = \mathbf{P}. \quad (5.2)$$

If the arbitrary test function  $\delta\mathbf{u}$  is applied to Eq. (5.1), it yields the modified global form as

$$p_0^{global} = \int_{\mathcal{B}_0} \{ \text{Div}(\mathbf{P}) \cdot \delta\mathbf{u} - \mathbf{b}_0 \cdot \delta\mathbf{u} \} dV = 0. \quad (5.3)$$

The test function  $\delta\mathbf{u}$  in any sense pertains to the variation of the *Dirichlet* boundary conditions such that  $\mathbf{u} = \hat{\mathbf{u}}$  on  $\partial\mathcal{B}_{0(D)}$ . In general, we define the variational form of any variable field  $(\bullet)$  as

$$\delta(\bullet) := \frac{\partial(\bullet)}{\partial\mathbf{u}} \delta\mathbf{u}. \quad (5.4)$$

It is clear that the weak form  $p_0^{weak}$  may be obtained once the *divergence theorem* and *Green's formula* are applied to Eq. (5.3). Thus, the weak form of this balance law is

$$p_0^{weak} = \int_{\mathcal{B}_0} \mathbf{P} : \text{Grad}(\delta \mathbf{u}) \, dV - \int_{\mathcal{B}_0} \mathbf{b}_0 \cdot \delta \mathbf{u} \, dV - \int_{\partial \mathcal{B}_0} \mathbf{PN} \cdot \delta \mathbf{u} \, dA = 0. \quad (5.5)$$

It may be decomposed further due to the *Piola-Kirchhoff* traction vector being defined in the reference configuration as  $\mathbf{t}_0 = \mathbf{PN}$ ;  $\mathbf{t}_0$  represents the *Nuemann* boundary conditions. Thus, the weak form of the momentum balance equation is

$$p_0^{weak} = \int_{\mathcal{B}_0} \mathbf{P} : \delta \mathbf{F} \, dV - \int_{\mathcal{B}_0} \mathbf{b}_0 \cdot \delta \mathbf{u} \, dV - \int_{\partial \mathcal{B}_0(N)} \mathbf{t}_0 \cdot \delta \mathbf{u} \, dA = 0. \quad (5.6)$$

We must consider that there are multiple equivalent forms of the stress power term — shown in Eq. (4.1). The weak form of the momentum balance using the *2<sup>nd</sup> Piola-Kirchhoff* stress tensor may thus be represented as

$$p_0^{weak} = \int_{\mathcal{B}_0} \frac{1}{2} \mathbf{S} : \delta \mathbf{C} \, dV - \int_{\mathcal{B}_0} \mathbf{b}_0 \cdot \delta \mathbf{u} \, dV - \int_{\partial \mathcal{B}_0(N)} \mathbf{t}_0 \cdot \delta \mathbf{u} \, dA = 0. \quad (5.7)$$

All the presented expressions of this form is independent of a separate damage term. However, damage is considered in the computation of the *2<sup>nd</sup> Piola-Kirchhoff* stress from the *Mandel* stress and will be shown later in this chapter. Furthermore,

$$\delta \mathbf{C} = \delta(\mathbf{F}^T \mathbf{F}) = \text{Grad}^T(\delta \mathbf{u}) \mathbf{F} + \mathbf{F}^T \text{Grad}(\delta \mathbf{u}). \quad (5.8)$$

### 5.3.2 Spatial discretisation principles

For a continuum body of  $n_e$  finite elements, its discretised form is written

$$\mathcal{B}_0 \approx \bigcup_{i=1}^{n_e} \mathcal{B}_{0(j)}, \quad (5.9)$$

with  $\mathcal{B}_{0(i)}$  being the material description of each element such that  $\mathcal{B}_{0(i)} \in \mathcal{B}_0$ . Thus, the boundary of the body  $\mathcal{B}_0$  is comprised of the areas of elements, since these elements do not overlap then the boundaries are connected by either points, lines or surfaces [47].

In this study, the spatial discretisation is such that the material configuration  $\mathcal{B}_0$  is mapped onto its corresponding finite elements through the general isoparametric

spatial discretisation concept. With isoparametric discretisation, the same arbitrary shape/interpolation functions  $N_I$  used to define the geometric shape of the elements are utilised in approximating the displacement field  $\mathbf{u}$ , its variational form  $\delta\mathbf{u}$  and incremental form  $\Delta\mathbf{u}$  in all configurations of the continuum [47]. Thus, we define the following interpolation formulae for  $\mathbf{u}$ ,  $\delta\mathbf{u}$  and  $\Delta\mathbf{u}$  as

$$\mathbf{u}_h = \sum_{I=1}^{N_e} N_I \mathbf{u}_I, \quad \text{Grad}(\mathbf{u}_h) = \sum_{I=1}^{N_e} \frac{\partial N_I}{\partial \mathbf{X}} \mathbf{u}_I, \quad (5.10)$$

$$\delta\mathbf{u}_h = \sum_{I=1}^{N_e} N_I \delta\mathbf{u}_I, \quad \text{Grad}(\delta\mathbf{u}_h) = \sum_{I=1}^{N_e} \frac{\partial N_I}{\partial \mathbf{X}} \delta\mathbf{u}_I \quad (5.11)$$

$$\Delta\mathbf{u}_h = \sum_{I=1}^{N_e} N_I \Delta\mathbf{u}_I, \quad \text{Grad}(\Delta\mathbf{u}_h) = \sum_{I=1}^{N_e} \frac{\partial N_I}{\partial \mathbf{X}} \Delta\mathbf{u}_I, \quad (5.12)$$

in which the iterative subscript  $I \in [1, 2, \dots, N_e]$  such that  $N_e$  is the number of nodes per element. This is defined in the material configuration.

In Eq. (5.9),  $\bigcup$  is an assembly operator — it indicates the union of finite entities. Consequently, this concept is utilised to discretise the displacement field and its dependent relations as

$$\mathbf{u} = \bigcup_{i=1}^{n_e} \mathbf{u}_{h(i)}, \quad (5.13)$$

$$\delta\mathbf{u} = \bigcup_{i=1}^{n_e} \delta\mathbf{u}_{h(i)}, \quad (5.14)$$

and

$$\Delta\mathbf{u} = \bigcup_{i=1}^{n_e} \Delta\mathbf{u}_{h(i)}. \quad (5.15)$$

### 5.3.3 Linearisation of the weak form

In order to provide a more compact form of the weak formulation of momentum balance in non-linear finite deformation applications, we utilise the spatial discretisation principles and the original variational statement Eq. (5.5). Thus, for each iteration step  $j + 1$  within a global simulation step  $n + 1$ , the linearised form of the momentum balance is obtained using a first-order *Taylor*-expansion [47] approximated with the solution of the displacement field  $(\mathbf{u}^j)_{n+1}$  from the



previous iteration step. Thus, the linearised form is the function of  $\mathbf{p}_0^{weak}$  at this displacement solution is

$$\mathbf{p}_0^{weak}(\mathbf{u}^{j+1})_{n+1} = \mathbf{p}_0^{weak}(\mathbf{u}^j + \Delta\mathbf{u}^{j+1})_{n+1} \quad (5.16)$$

$$\rightarrow \mathbf{p}_0^{weak}(\mathbf{u}^{j+1})_{n+1} = \mathbf{p}_0 \mathbf{p}_0^{weak}(\mathbf{u}^j)_{n+1} + \frac{\partial \mathbf{p}_0^{weak}}{\partial \mathbf{u}} \Big|_{\mathbf{u}_{n+1}^j} (\Delta\mathbf{u}^{j+1})_{n+1}. \quad (5.17)$$

The incremental form of any primary variable field is described as

$$\Delta(\bullet) := \frac{\partial(\bullet)}{\partial \mathbf{u}} \Delta\mathbf{u}, \quad (5.18)$$

thus we may obtain an expanded form of Eq. (5.17) as follows:

$$\begin{aligned} \mathbf{p}_0^{weak}(\mathbf{u}^{j+1})_{n+1} &= \int_{\mathcal{B}_0} \mathbf{F}\mathbf{S} : \text{Grad}(\delta\mathbf{u}) \, dV \\ &+ \int_{\mathcal{B}_0} \mathbf{D}\mathbf{F} \text{Grad}(\Delta\mathbf{u}) : \mathbf{F} \text{Grad}(\delta\mathbf{u}) \, dV + \int_{\mathcal{B}_0} \text{Grad}(\Delta\mathbf{u}) \mathbf{S} : \text{Grad}(\delta\mathbf{u}) \, dV \\ &- \int_{\mathcal{B}_0} \mathbf{b}_0 \cdot \delta\mathbf{u} \, dV - \int_{\partial\mathcal{B}_0} \mathbf{t}_0 \cdot \delta\mathbf{u} \, dA = 0, \end{aligned} \quad (5.19)$$

whereby  $\mathbf{D}$  is the tangent operator and is computed in the constitutive model (see Section 5.5.4). Then

$$\begin{aligned} \mathbf{p}_0^{weak}(\mathbf{u}^{j+1})_{n+1} &= \int_{\mathcal{B}_{0(e)}} \mathbf{F}\mathbf{S} : \frac{\partial N_I}{\partial \mathbf{X}} \delta\mathbf{u}_I \, dV \\ &+ \int_{\mathcal{B}_{0(e)}} \mathbf{F}^T \mathbf{D}\mathbf{F} \frac{\partial N_I}{\partial \mathbf{X}} \Delta\mathbf{u}_I : \frac{\partial N_I}{\partial \mathbf{X}} \delta\mathbf{u}_I \, dV + \int_{\mathcal{B}_{0(e)}} \frac{\partial N_I}{\partial \mathbf{X}} \Delta\mathbf{u}_I \mathbf{S} : \frac{\partial N_I}{\partial \mathbf{X}} \delta\mathbf{u}_I \, dV \\ &- \int_{\mathcal{B}_{0(e)}} \mathbf{b}_0 \cdot N_I \delta\mathbf{u}_I \, dV - \int_{\partial\mathcal{B}_{0(e)}} \mathbf{t}_0 \cdot N_I \delta\mathbf{u}_I \, dA = 0. \end{aligned} \quad (5.20)$$

is produced when the interpolated forms of the displacement field Eq. (5.10), and its variational Eq. (5.11) and incremental forms Eq. (5.12) are subsequently substituted into Eq. (5.19). This is evaluated at each element  $e$  adjacent to node  $I$

The condition  $\mathbf{p}_0^{weak} = 0$  leads to Eq. (5.20) taking the form of a discrete equation system:

$$(\mathbf{K}^{j+1})_{n+1}(\Delta \mathbf{u}^{j+1})_{n+1} = (\mathbf{f}_{ext}^{j+1})_{n+1} - (\mathbf{f}_{int}^{j+1})_{n+1}, \quad (5.21)$$

whereby  $(\mathbf{f}_{ext}^{j+1})_{n+1}$  is related to the step-wise incremental, or static externally applied loads,  $(\mathbf{f}_{int}^{j+1})_{n+1}$  is the stress response, and  $(\mathbf{K}^{j+1})_{n+1}$  is the stiffness matrix. The residual vector  $\mathbf{r}$  is introduced which is interpreted as the net force vector:

$$(\mathbf{r}^{j+1})_{n+1} = (\mathbf{f}_{ext}^{j+1})_{n+1} - (\mathbf{f}_{int}^{j+1})_{n+1}. \quad (5.22)$$

All of the above formulations and equations consequently result in a discrete expression for the iterative solution scheme of the displacement field  $\mathbf{u}$  as

$$(\Delta \mathbf{u}^{j+1})_{n+1} = (\mathbf{K}^{j+1})_{n+1}^{-1} (\mathbf{r}^{j+1})_{n+1}, \quad (5.23)$$

which is additively updated at the end of each iteration step  $j + 1$  as

$$(\mathbf{u}^{j+1})_{n+1} = (\mathbf{u}^j + \Delta \mathbf{u}^{j+1})_{n+1}. \quad (5.24)$$

It must be noted that

$$(\mathbf{K}^{j+1})_{n+1} = \int_{\mathcal{B}_{0(e)}} \mathbf{F}^T \mathbf{D} \mathbf{F} \frac{\partial N_I}{\partial \mathbf{X}} : \frac{\partial N_I}{\partial \mathbf{X}} dV + \int_{\mathcal{B}_{0(e)}} \frac{\partial N_I}{\partial \mathbf{X}} \mathbf{S} : \frac{\partial N_I}{\partial \mathbf{X}} dV, \quad (5.25)$$

$$(\mathbf{f}_{ext}^{j+1})_{n+1} = \int_{\mathcal{B}_{0(e)}} \mathbf{b}_0 \cdot N_I dV + \int_{\partial \mathcal{B}_{0(e)}} \mathbf{t}_0 \cdot N_I dA, \quad (5.26)$$

and

$$(\mathbf{f}_{int}^{j+1})_{n+1} = \int_{\mathcal{B}_{0(e)}} \mathbf{F} \mathbf{S} : \frac{\partial N_I}{\partial \mathbf{X}} dV. \quad (5.27)$$

The norm of the residual vector  $\mathbf{r}$  is then checked for convergence to ensure an appropriately precise approximation and a smooth transition to consequent simulation steps:

$$\| (\mathbf{r}^{j+1})_{n+1} \| < 1.0 \times 10^{-8}. \quad (5.28)$$

## 5.4 Numerical treatment

### 5.4.1 Principles of the *Newton-Raphson* method

The *Newton-Raphson* method is a fast gradient method, which facilitates for estimating an unknown root solution  $(\bullet)_{i+1}$  of an arbitrary, known real-valued function  $\mathbf{f}(\bullet)$  of variable(s)  $(\bullet)$  given an initial value  $(\bullet)_i$ . The method is shown schematically in Figure 5.2.

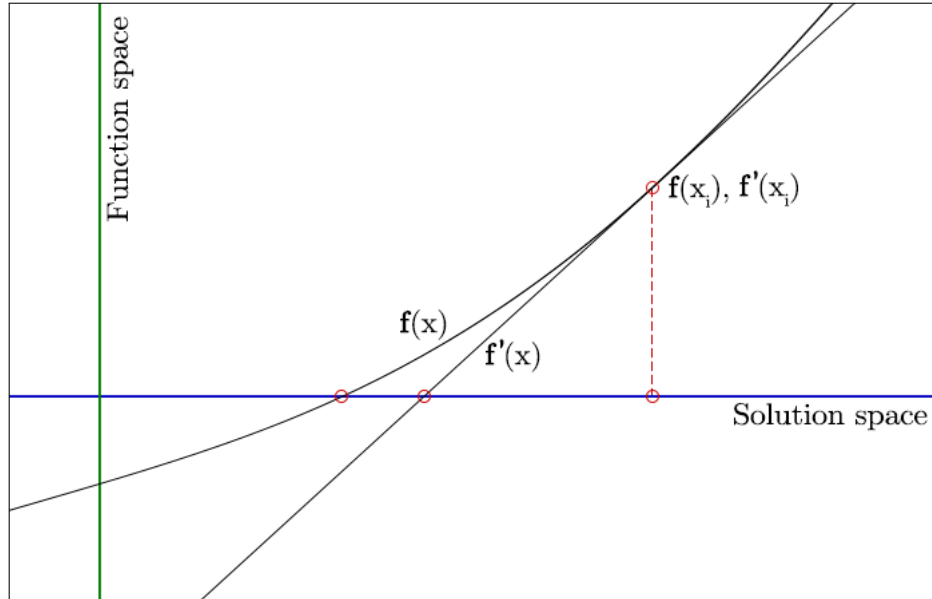


**Figure 5.2:** Newton-Raphson method. The function space contains the possible values a function may take and the solution space the possible values the inputs to the function may take.

If both the unknown root solution and the initial value lie in the same 1D solution space, the function tangent  $\mathbf{f}'(\bullet)_j$  is then used to estimate the value of the unknown root solution at the point at which the function tangent crosses the solution space from the initial value  $(\bullet)_j$ . It is illustrated mathematically as

$$(\bullet)_{j+1} = (\bullet)_j - \frac{\mathbf{f}(\bullet)_j}{\mathbf{f}'(\bullet)_j}. \quad (5.29)$$

The initial step is only a rough approximation. Therefore, it requires further  $j \in \mathbb{Z}$  local iterations within each global *Newton-Raphson* step  $n + 1$  to achieve a finer approximation of the true root value  $(\bullet)_{n+1}^r$  of the function  $\mathbf{f}(\bullet)$  [9]. Furthermore, the residual  $R$  must be of acceptably low value between iterations to ensure an accurate refinement. Thus, for each global simulation step  $n + 1$ ,

$$\underline{\text{For each}(n + 1) \mid R < 1.0}$$

$$\rightarrow (\bullet)_{n+1}^r = \underset{j \in \mathbb{Z}}{\text{iter}} \left[ (\bullet)_{j+1} - \frac{\mathbf{f}(\bullet)_j}{\mathbf{f}'(\bullet)_j} \right]. \quad (5.30)$$

This iterative method is highly suitable for pure plasticity and damaged plasticity applications as it is fast to iterate and fast to converge whenever there is the non-linear phenomena of plasticity and this method is used directly for calculating the plastic multiplier for each iteration. The fast convergence is dependent on the increment of the load-factor.

### 5.4.2 Local time discretisation

During any time-dependent computational analysis, the time  $t$  controls the loading and boundary condition information available as inputs into the equation solver. Thus, as time elapses the material is continually loaded and deformed. If the procedure in retrieving a solution in a simulation is time-dependent, there are a possible  $n \mid n \geq 0$  simulation steps within a time interval and then the time increment for each simulation step is considered as being

$$\Delta t = t_{n+1} - t_n. \quad (5.31)$$

Knowing this, the time integration of all secondary field quantities denoted with placeholder  $\mathbf{a}$  (such as  $\mathbf{F}_{pl}, \mathbf{L}, \boldsymbol{\alpha}$ ) or scalar quantities denoted  $b$  (such as  $M$  or  $Z$ ) proceeds in the following general format [42]:

$$\Delta \mathbf{a} = \Delta t \dot{\mathbf{a}}, \quad \Delta b = \Delta t \dot{b}, \quad (5.32)$$

in which each of these rate  $(\dot{\mathbf{a}}, \dot{b})$  are directly solved as per each quantities algorithmic implementation. These quantities update in each simulation step  $n \mid n \geq 0$  as follows:

$$(\mathbf{a})_{n+1} = (\mathbf{a})_n + \Delta \mathbf{a}, \quad (5.33)$$

$$b_{n+1} = b_n + \Delta b. \quad (5.34)$$

In this study, primary field quantities are the quantities discretised by the finite element techniques whilst secondary quantities are updated algorithmically by the constitutive model.

### 5.4.3 Local iterative update of plastic multiplier

The plastic increment  $\Delta\lambda$  may be defined as the incremental quantity governing the evolution of all non-recoverable material deformation. The plastic multiplier  $\lambda$  is the state of the plastic behaviour in the continuum. This study is focused towards a *Newton-Raphson* based implementation, a gradient solution method. This is in stark contrast to the types of direct solution techniques usually employed for damage models in [5] and [30].

The plastic multiplier  $\lambda$  is dependent on the calculated stresses and strains in the plastic range, which depend on the amount of deformation at a particular material point within a simulation step  $n$ . The evolution of the plastic multiplier, is the plastic increment and for rate-independent *von Mises*-based plasticity models it may be computed using the *von Mises* yield function for which as follows:

$$\Delta\lambda = -\frac{f}{\left(\frac{\partial f}{\partial \lambda}\right)}. \quad (5.35)$$

Thus, the above equation is used in conjunction with Eq. (5.30) to produce the update of the plastic multiplier as

$$\lambda_{j+1} = \lambda_j + \Delta\lambda. \quad (5.36)$$

This update mechanism depended on the return mapping algorithms for each of the yield function and the the tangent of the yield function with respect to the plastic multiplier, which are shown in Section 5.5.

## 5.5 Algorithmic implementation

### 5.5.1 Elastic-plastic predictor algorithms

#### *Strain and strain-rate*

The deformation gradient is a field quantity in this framework, and is decomposed multiplicatively at all instances in time (see Section 4.2.1). This is because the continuum  $\mathcal{B}$  at any simulation step  $n$  is considered a reference configuration with respect to the next simulation step  $n + 1$  - a *Lagrangian* approach. Therefore, the plastic deformation gradient update is a mathematical consequence of this and is

$$(\mathbf{F}_{pl})_{n+1} = (\mathbf{F}_{pl})_n \Delta \mathbf{F}_{pl}. \quad (5.37)$$

It follows that in an isochoric (volume-preserving) finite inelastic deformation of a material continuum  $\mathcal{B}_n \rightarrow \mathcal{B}_{n+1}$ , the incompressibility constraint must always apply on the plastic deformation gradient at this simulation step as follows

$$\det(\mathbf{F}_{pl}) = J_{pl} = 1. \quad (5.38)$$

This directly implies that all plastic deformations are incompressible as well, i.e.  $\det(\mathbf{F}_{pl})_n = 1$ ,  $\det(\mathbf{F}_{pl})_{n+1} = 1$ , and  $\det(\Delta\mathbf{F}_{pl}) = 1$ . It is clear that these matrices are all elements of the special linear *Lie* group  $SL(3, \mathbb{R})$  — which is a set of square invertible matrices with determinant = 1 [7].

Using the time discretisation concepts of field quantities outlined in Eq. (5.33) with the relation in Eq. (2.27), it may be seen that the the rate term,  $\Delta\mathbf{F}_{pl}$ , in Eq. (5.37) decomposes as

$$\Delta\mathbf{F}_{pl} = \Delta\dot{\mathbf{F}}_{pl}\mathbf{L}_{pl} \quad (5.39)$$

$$\Delta\mathbf{F}_{pl} = \Delta t\mathbf{F}_{pl}\mathbf{L}_{pl} \quad (5.40)$$

$$\Delta\mathbf{F}_{pl} = \mathbf{F}_{pl}\Delta t\mathbf{L}_{pl}. \quad (5.41)$$

Since  $\det(\Delta\mathbf{F}_{pl}) = 1$ , then the important consequence is that  $\det(\mathbf{L}_{pl}) = 1$ ;  $\mathbf{L}_{pl}$  is an element of the lie algebra of  $SL(3, \mathbb{R})$  and is trace-independent i.e.  $\text{tr}(\mathbf{L}_{pl}) = 0$  [39]. Thus, the exponential time-integration mapping is utilised for the plastic *strain-rate*  $\mathbf{L}_{pl}$  such that

$$\Delta\mathbf{F}_{pl} = \exp(\Delta t\mathbf{L}_{pl}), \quad (5.42)$$

holds since  $\det(\Delta\mathbf{F}_{pl}) = 1$ . It also holds that  $\det(\exp(\mathbf{L}_{pl}))$ ,  $\det(\exp(\Delta t\mathbf{L}_{pl})) = 1$ . This information is fed into the relation in Eq. (5.37) and produces an algorithmic update equation for the plastic deformation gradient as

$$(\mathbf{F}_{pl})_{n+1} = (\mathbf{F}_{pl})_n \exp(\Delta t\mathbf{L}_{pl}). \quad (5.43)$$

Similarly, from the definition of the distorted *Hencky* strain measure  $\bar{\boldsymbol{\alpha}} = \ln(\mathbf{C}_{pl}^{-1}\mathbf{C})$ , it follows that the plastic *Cauchy-Green* tensor is of the follow form:

$$(\mathbf{C}_{pl}^{-1})_{n+1} = \Delta\mathbf{F}_{pl}^{-1}(\mathbf{C}_{pl}^{-1})_n\Delta\mathbf{F}_{pl}^{-T}. \quad (5.44)$$

It is trivial to the formulate the following equation regarding the plastic *Cauchy-Green* tensor as

$$(\mathbf{C}_{pl}^{-1})_{n+1} = \exp(-\Delta t \mathbf{L}_{pl})(\mathbf{C}_{pl}^{-1})_n \exp(-\Delta t \mathbf{L}_{pl}^T). \quad (5.45)$$

Therefore,

$$(\mathbf{C}\mathbf{C}_{pl}^{-1})_{n+1} = (\mathbf{C})_{n+1} \exp(-\Delta t \mathbf{L}_{pl})(\mathbf{C}_{pl}^{-1})_n \exp(-\Delta t \mathbf{L}_{pl}^T), \quad (5.46)$$

which directly leads to an elastic-plastic corrector step algorithm for the *Hencky* strain as outlined in [39]

$$(\bar{\boldsymbol{\alpha}}^T)_{n+1} = \ln[(\mathbf{C}\mathbf{C}_{pl}^{-1})_{n+1}] \quad (5.47)$$

$$(\bar{\boldsymbol{\alpha}}^T)_{n+1} = \ln[(\mathbf{C})_{n+1} \exp(-\Delta t \mathbf{L}_{pl})(\mathbf{C}_{pl}^{-1})_n \exp(-\Delta t \mathbf{L}_{pl}^T)] \quad (5.48)$$

$$(\bar{\boldsymbol{\alpha}}^T)_{n+1} = \ln[(\mathbf{C})_{n+1}(\mathbf{C}_{pl}^{-1})_n \exp(-2\Delta t \mathbf{L}_{pl}^T)] \quad (5.49)$$

$$(\bar{\boldsymbol{\alpha}}^T)_{n+1} = (\bar{\boldsymbol{\alpha}}^T)^{trial} - 2\Delta t \mathbf{L}_{pl}^T. \quad (5.50)$$

The plastic rate of deformation tensor,  $\mathbf{L}_{pl}$  is derived using the time integration principles in Section 5.4.2 and the plastic *strain-rate* tensor as per the associative flow rule and is presented algorithmically as

$$\mathbf{L}_{pl} = \lambda_{j+1} \frac{\text{dev}(\boldsymbol{\Sigma}^{trial})^T}{(1 - M)_{n+1} \|\text{dev}(\boldsymbol{\Sigma}^{trial})\|} = \lambda_{j+1} \mathbf{N}^T. \quad (5.51)$$

### **Mandel stress**

As the assumption of full isotropy of the material body is maintained, the *Hencky* strain and its corresponding *Mandel* stress measure are co-axial. This is similar to the manner in the *Green-Lagrange* strain tensor and the *Cauchy* stress tensor are interpreted.

Therefore, the *Mandel* stress tensor may be updated as in Eq. (5.52) — it must be taken into account that the material stiffness and strength moduli are degraded uniformly as damage evolves. The damage residual  $(1 - M)_{n+1}$  is incorporated into the equation as per the elastic constitutive relations in Section 4.3.

$$\boldsymbol{\Sigma}_{n+1} = (1 - M)_{n+1} [K \text{tr}(\bar{\boldsymbol{\alpha}}^{trial})^T \mathbf{I} + G \text{dev}(\bar{\boldsymbol{\alpha}}^{trial})^T - 2G\Delta t \mathbf{L}_{pl}^T] \quad (5.52)$$

which decomposes into

$$\boldsymbol{\Sigma}_{n+1} = \boldsymbol{\Sigma}^{trial} - 2G(1 - M)_{n+1} \Delta t \lambda_{j+1} \mathbf{N} \quad (5.53)$$

and then

$$\boldsymbol{\Sigma}_{n+1} = \boldsymbol{\Sigma}^{trial} - 2G\Delta t\lambda_{j+1} \frac{\text{dev}(\boldsymbol{\Sigma}^{trial})}{\|\text{dev}(\boldsymbol{\Sigma}^{trial})\|}. \quad (5.54)$$

since the flow vector  $\mathbf{N}$  is computed as

$$\mathbf{N} = \frac{\text{dev}(\boldsymbol{\Sigma}^{trial})}{(1 - M)_{n+1}\|\text{dev}(\boldsymbol{\Sigma}^{trial})\|}. \quad (5.55)$$

Therefore for all computations requiring the plastic rate of deformation tensor shall also require the trial stress to be computed and used in the equations therefore. All the tensors computed using the return-mapping algorithms are further decomposed into *index* notation in Appendix A.

## 5.5.2 Return mapping algorithms

### *Inelasticity*

The return mapping algorithms for the internal state variables: damage and plastic hardening, depend directly on the plastic increment as is shown in Section 4.7.4. The plastic hardening state variable  $Z$ , is a scalar function of the the plastic multiplier,  $\lambda$  updates as

$$Z_{n+1} = Z_n + \sqrt{\frac{2}{3}}\Delta t\lambda_{j+1}, \quad (5.56)$$

$$\frac{\partial Z_{n+1}}{\partial \lambda} = \sqrt{\frac{2}{3}}\Delta t. \quad (5.57)$$

In a similar vein, the damage variable  $M$ , with its evolution as shown in Section 4.7.4 may be updated as in accordance with the time integration principles as per this study:

$$M_{n+1} = M_n + \sqrt{\frac{2}{3}} \frac{\Delta t\lambda_{j+1}}{(1 - M)_{n+1}} \left( \frac{Y_{n+1}}{S_0} \right)^{s_0} \text{ for } p > p^M. \quad (5.58)$$

Furthermore, the *damage variable tangent* may be defined as follows:



$$\begin{aligned} \frac{\partial M_{n+1}}{\partial \lambda} = \sqrt{\frac{2}{3}} \Delta t \left[ \frac{1}{(1-M)_{n+1}} \left( \frac{Y_{n+1}}{S_0} \right)^{s_0} + \frac{\left( \frac{\partial M}{\partial \lambda} \right)_{n+1} \lambda_{j+1}}{(1-M)_{n+1}^2} \left( \frac{Y_{n+1}}{S_0} \right)^{s_0} \right. \\ \left. + \frac{s_0}{S_0} \frac{\lambda_{j+1}}{(1-M)_{n+1}} \left( \frac{Y_{n+1}}{S_0} \right)^{s_0-1} \frac{\partial Y_{n+1}}{\partial \lambda} \right]. \end{aligned} \quad (5.59)$$

This tangent is incorporated in the yield function tangent update which is then utilised in the *Newton-Raphson* scheme. Following the computation of the material stress, the modified *von Mises* yield equation may be represented thereof. The hardening state variable  $Z$  is represented by  $Z_{n+1}$  in the yield equations:

$$f = \frac{\|\text{dev}(\boldsymbol{\Sigma}_{n+1})\|}{(1-M)_{n+1}} - \sqrt{\frac{2}{3}} (\sigma_y - R_{n+1}) = 0 \quad (5.60)$$

then, the yield equation takes the form of

$$f = \frac{\|\text{dev}(\boldsymbol{\Sigma}^{\text{trial}})\| - 2G\Delta t \lambda_{j+1}}{(1-M)_{n+1}} - \sqrt{\frac{2}{3}} (\sigma_y - R_{n+1}) = 0. \quad (5.61)$$

As for the properties governing material hardening, these may be updated within this framework as below, whereby the hardening stress-like variable  $R$  introduced in Section 4.7.3 is

$$R_{n+1} = -HZ_{n+1} - (\sigma_\infty - \sigma_y) [1 - \exp(-\eta Z_{n+1})] \quad (5.62)$$

with its tangent with respect to plastic multiplier  $\lambda$ , vital to the algorithmic implementation, defined as

$$\frac{\partial R_{n+1}}{\partial \lambda} = \frac{\partial R_{n+1}}{\partial Z_{n+1}} \left( \frac{\partial Z_{n+1}}{\partial \lambda} \right) = -\sqrt{\frac{2}{3}} \Delta t [H + \eta(\sigma_\infty - \sigma_y) \exp(-\eta Z_{n+1})]. \quad (5.63)$$

Going back, the yield function tangent is approximated as the partial differential of the yield functions and the plastic multiplier may be expressed as

$$\frac{\partial f}{\partial \lambda} = -\frac{2G\Delta t}{(1-M)_{n+1}} - \frac{2G\Delta t \lambda_{j+1} \left( \frac{\partial M_{n+1}}{\partial \lambda} \right)}{(1-M)_{n+1}^2} + \sqrt{\frac{2}{3}} \frac{\partial R_{n+1}}{\partial \lambda}. \quad (5.64)$$

It would be useful to know the yield function tangent with respect to the *Mandel* stress tensor, as this tangent may be used in further calculations to satisfy the *Newton-Raphson* predictor update of the plastic multiplier.

$$\begin{aligned} \frac{\partial f}{\partial \boldsymbol{\Sigma}^{trial}} &= \frac{1}{(1-M)_{n+1}} \frac{\partial(\|\text{dev}(\boldsymbol{\Sigma}^{trial})\|)}{\partial \boldsymbol{\Sigma}^{trial}} \\ &- \frac{\partial \lambda}{\partial \boldsymbol{\Sigma}^{trial}} \left( \frac{2G\Delta t}{(1-M)_{n+1}} + \frac{2G\Delta t \lambda_{j+1} \left( \frac{\partial M_{n+1}}{\partial \lambda} \right)}{(1-M)_{n+1}^2} - \sqrt{\frac{2}{3}} \frac{\partial R_{n+1}}{\partial \lambda} \right), \end{aligned} \quad (5.65)$$

whereby, from Eq. (5.51), it is seen that

$$\frac{\partial(\|\text{dev}(\boldsymbol{\Sigma}^{trial})\|)}{\partial \boldsymbol{\Sigma}^{trial}} = (1-M)_{n+1} \mathbf{N}^T. \quad (5.66)$$

Thus, the following relation also holds:

$$\frac{\partial \lambda}{\partial \boldsymbol{\Sigma}^{trial}} = \frac{\mathbf{N}^T}{\left( \frac{2G\Delta t}{(1-M)_{n+1}} + \frac{2G\Delta t \lambda_{j+1} \left( \frac{\partial M_{n+1}}{\partial \lambda} \right)}{(1-M)_{n+1}^2} - \sqrt{\frac{2}{3}} \frac{\partial R_{n+1}}{\partial \lambda} \right)}. \quad (5.67)$$

### ***Damage-related variables***

From the constitutive model as summarised in Section 5.1, the stress-like variable,  $Y$ , that is associated with damage is a scalar function of the damage variable  $M$ .

$$Y_{n+1} = \frac{\|\text{dev}(\boldsymbol{\Sigma}_{n+1})\|^2}{4G(1-M)_{n+1}^2} + \frac{[\text{tr}(\boldsymbol{\Sigma}_{n+1})]^2}{2K(1-M)_{n+1}^2} \quad (5.68)$$

However, in this algorithmic implementation it is also a function of the plastic multiplier  $\lambda$  in this algorithmic implementation. We may apply the return mapping algorithm to this variable as follows:

$$\begin{aligned} Y_{n+1} &= \frac{[\|\text{dev}(\boldsymbol{\Sigma}^{trial})\|^2 - 4G\Delta t \lambda_{j+1} \|\text{dev}(\boldsymbol{\Sigma}^{trial})\| + 4(G\Delta t \lambda_{j+1})^2]}{4G(1-M)_{n+1}^2} \\ &+ \frac{[\text{tr}(\boldsymbol{\Sigma}^{trial})]^2}{2K(1-M)_{n+1}^2} \end{aligned} \quad (5.69)$$

The trace and deviatoric portion of the *Mandel* stress  $\Sigma$  are decomposed as shown in Eq. (4.21). Thus the final algorithmic implementation of the damage energy density release rate is

$$Y_{n+1} = \frac{\|\text{dev}(\Sigma^{trial})\|^2}{4G} + \frac{[\text{tr}(\Sigma^{trial})]^2}{2K} - \frac{\Delta t \lambda_{j+1} \|\text{dev}(\Sigma^{trial})\|}{(1-M)_{n+1}} + \frac{G(\Delta t \lambda_{j+1})^2}{(1-M)_{n+1}^2}. \quad (5.70)$$

its tangent may then be computed to incorporate in the damage variable tangent and thus satisfies the *Newton-Raphson* update of the plastic multiplier -

$$\frac{\partial Y_{n+1}}{\partial \lambda} = -\frac{\Delta t \|\text{dev}(\Sigma^{trial})\|}{(1-M)_{n+1}} - \frac{\left(\frac{\partial M}{\partial \lambda}\right)_{n+1} \Delta t \lambda_{j+1} \|\text{dev}(\Sigma^{trial})\|}{(1-M)_{n+1}^2} + \frac{2G(\Delta t)^2 \lambda_{j+1}}{(1-M)_{n+1}^2} + \frac{2\left(\frac{\partial M}{\partial \lambda}\right)_{n+1} G(\Delta t \lambda_{j+1})^2}{(1-M)_{n+1}^3}. \quad (5.71)$$

### 5.5.3 *Piola-Kirchhoff* stress computation

The stress update framework for this model is based on that in [39] and the finite element framework in SESKA. In this material damage model, the *Mandel* stress tensor  $\Sigma$  is computed as a function of the *Hencky* logarithmic strain  $\bar{\alpha}$ . However, such a stress tensor is only used due to its work conjugacy with the plastic *strain-rate* tensor  $\mathbf{L}_{pl}$  and that it can be pulled back to compute the 2<sup>nd</sup> *Piola-Kirchhoff* stress. In the SESKA finite element framework, the 2<sup>nd</sup> *Piola-Kirchhoff* stress tensor  $\mathbf{S}$  is used to record and characterise stresses with the *Lagrangian* approach. From Eq. (4.20),  $\mathbf{S}$  is related to the right *Cauchy-Green* tensor  $\mathbf{C}$  as

$$\mathbf{S} = \mathbf{C}^{-1} \Sigma, \quad (5.72)$$

and after substituting Eq. (5.54) into this expression, the following is true:

$$\mathbf{S} = \mathbf{C}^{-1} (\Sigma^{trial} - 2G(1-M)\Delta t \lambda \mathbf{N}^T). \quad (5.73)$$

### 5.5.4 Algorithmic tangent operator

The 2<sup>nd</sup> *Piola-Kirchhoff* stress tensor is used to characterise stresses in the reference state of a material and is work/power conjugate to the right *Cauchy-Green* tensor  $\mathbf{C}$ . The tangent operator  $\mathbf{D}$  is obtained by linearising  $\mathbf{S}$  with respect to  $\mathbf{C}$ :

$$\mathbf{D} = \frac{\partial \mathbf{S}}{\partial \mathbf{C}}. \quad (5.74)$$

The algorithmic implementation of the tangent operator for the 2<sup>nd</sup> *Piola-Kirchhoff* stress is as follows:

$$\frac{\partial \mathbf{S}}{\partial \mathbf{C}} = \frac{\partial (\mathbf{C}^{-1} (\boldsymbol{\Sigma}^{trial} - 2G(1-M)\Delta t \lambda \mathbf{N}^T))}{\partial \mathbf{C}}, \quad (5.75)$$

which is expanded and represented in tensor notation as

$$\begin{aligned} \frac{\partial \mathbf{S}}{\partial \mathbf{C}} &= \frac{\partial \mathbf{C}^{-1}}{\partial \mathbf{C}} (\boldsymbol{\Sigma}^{trial} - 2G(1-M)\Delta t \lambda \mathbf{N}) + \mathbf{C}^{-1} \frac{\partial \boldsymbol{\Sigma}^{trial}}{\partial \mathbf{C}} \\ &\quad - 2G(1-M)\Delta t \frac{\partial \lambda}{\partial \boldsymbol{\Sigma}^{trial}} \frac{\partial \boldsymbol{\Sigma}^{trial}}{\partial \mathbf{C}} \mathbf{C}^{-1} \mathbf{N}^T - 2G(1-M)\Delta t \lambda \mathbf{C}^{-1} \frac{\partial \mathbf{N}^T}{\partial \boldsymbol{\Sigma}^{trial}} \frac{\partial \boldsymbol{\Sigma}^{trial}}{\partial \mathbf{C}} \end{aligned} \quad (5.76)$$

The following relations apply for the right *Cauchy-Green* tensor, which follow from the fundamental properties of a tensor

$$\frac{\partial \mathbf{C}^{-1}}{\partial \mathbf{C}} = -\mathbf{C}^{-1} \mathbf{C}^{-1} \quad (5.77)$$

For the trial *Mandel* stress, and its derivative with respect to the right *Cauchy-Green* tensor:

$$\frac{\partial \boldsymbol{\Sigma}^{trial}}{\partial \mathbf{C}} = \frac{\partial \boldsymbol{\Sigma}^{trial}}{\partial \bar{\boldsymbol{\alpha}}} \frac{\partial \bar{\boldsymbol{\alpha}}}{\partial \mathbf{C}} = (1-M) \left[ \left( K - \frac{1}{3}G \right) \mathbf{C}^{-1} \mathbf{I} + G \mathbf{C}^{-1} \mathbf{I} \right] \quad (5.78)$$

Also, the  $\partial \lambda / \partial \boldsymbol{\Sigma}^{trial}$  term in Eq. (5.76) is previously outlined equations in Eq. (5.67). Finally, the  $\partial \mathbf{N}^T / \partial \boldsymbol{\Sigma}^{trial}$  term is

$$\frac{\partial \mathbf{N}^T}{\partial \boldsymbol{\Sigma}^{trial}} = \frac{(1-M)}{\|\text{dev}(\boldsymbol{\Sigma}^{trial})\|} \left( \mathbf{1} : \mathbf{1} - \frac{1}{3} \mathbf{1} : \mathbf{1} - \mathbf{N}^T : \mathbf{N}^T \right) \quad (5.79)$$

whereby  $\mathbf{1}$  is an *all-ones matrix* as defined in Eq. (2.2).

---

The final form of the consistent tangent operator algorithm may be produced by inserting all the derived quantities in Eq. (5.77), Eq. (5.78), Eq. (5.67) and Eq. (5.79). This final form is represented in *index* notation Appendix A.

# Chapter 6

## Results and example simulations

Running simulations using this proposed material damage model is crucial to establishing a basis for any further progress as part of this study. The proposed model is of strongly coupled elastoplasticity and ductile damage — as outlined by Skrzypek & Ganczarski [43], *strong coupling* of damage is when the damage variable affects both the constitutive formulation and the inelastic response as part of the overall numerical implementation. It is evident that the constitutive formulation ( Section 4) and subsequent implementation ( Section 5) explicitly present this model as a strongly coupled model.

Examples will be assessed per the typical material parameters of the specific materials under study. Furthermore, it will be important to provide as much analysis based on the concepts within continuum mechanics as well as structural mechanics and analysis, in assessing model predictions. Even though our framework is strictly limited to three-dimensional formulations, it shall be shown that two-dimensional examples are also well within the scope of this model. Universal assumptions made are as follows: all gravity or other body-related forces are considered annulled, all heat sources, heat fluxes are considered annulled and all kinematic effects (such as translational velocity or acceleration are considered annulled). This section intends to assess pure external loading/displacement scenarios. All problems are simulated on UCT HPC Cluster and then post-processed in SESKA, all boundary conditions are assigned in GiD<sup>1</sup>. Lastly, all examples use 1st-order (linear) shape functions for functional approximation.

### 6.1 Tip-loaded cantilever beam

A cantilever beam is a structural element most commonly used in buildings as balconies, overhangs, and bridges. Such a structural element is well-studied. The bending of a cantilever beam may be used to present the intricacies of the material damage model, and to compare and related it to undamaged plasticity. Thus, this example uses a cantilever beam specimen with both damaged and undamaged plasticity considerations.

---

<sup>1</sup>GiD is a pre- and post-processing program for finite element-based analysis. It allows for users to discretise boundary conditions, material properties and simulation parameters in conjunction with the SESKA framework.

### 6.1.1 Problem setup, meshing and boundary conditions

The beam is assumed to have a length of  $L_{beam} = 10\text{ m}$ , with depth  $h_{beam} = 1\text{ m}$  and width  $w_{beam} = 1\text{ m}$ . The free end of the cantilevered beam is subject to a surface traction loading condition. The simulation is displacement-controlled at Point  $p_0$  on the beam such that displacement is always a maximum at the free-end of the beam; the simulation is programmed to end at a  $z$ -axis displacement of  $u_{z,max} = 4.776\text{ m}$ .

The other end of the beam is fixed to a wall, and thus all degrees of freedom are assumed to be  $= 0$ . By the way of the problem set-up, setting all displacement degrees of freedom  $= 0$  thus sets all rotational degrees of freedom  $= 0$  at the fixed end in tandem.

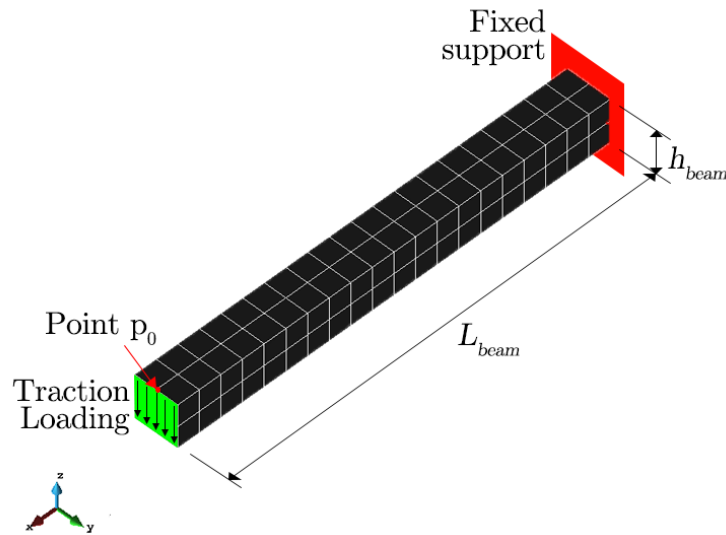


**Figure 6.1:** Mesh, problem configuration & boundary conditions. The cantilever beam model used a 3D mesh of 80 hexahedral volume elements. The fixity and loading conditions are shown.

The FEM mesh is shown as in Figure 6.1, which has 80 hexahedral volume elements and 168 quadrilateral surface elements. The mesh is fairly finer than those seen in previous literature such as [15] where they used 10 hexahedral/cubic volume elements.

To control the evolution of displacement in this model, the loading is displacement-controlled at the point  $p_0$  as shown in the cross-section of the cantilevered beam such that the displacement is always at a maximum at the loaded end of the beam. This is also the case in literature such as [15] — in a brief departure from the context of this study, a damage-free elastoplastic material model was used in Hopkin’s paper to assess a geometrically identical cantilevered beam to the one in this study.

Lastly, the load is applied statically, so much so that all analysis performed is static. Thus, allowing for a pure analysis of cumulative monotonic material behaviour.

### 6.1.2 Material properties

For the cantilever beam model, the material being analysed is steel, a ductile material for which the behaviour is well-established. Notably, for the sake of this analysis, local damage is assumed to initiate as immediately as plasticity commences. Thus, the requirement is zero accumulated plastic strain for observation of damage phenomena. This also applies to strain/work hardening, as soon as plasticity commences the material may start to harden or soften accordingly.

Thus, the material properties for the elasticity applications are shown as in Table 6.1 together with those relevant to plasticity and *Lemaitre*-based damage and non-linear exponential-based isotropic hardening are as in Table 6.1.

**Table 6.1:** Material properties of cantilever beam.

| <b>Elasticity</b>                     |             |
|---------------------------------------|-------------|
| Bulk modulus, $K$                     | 164.206 GPa |
| Shear modulus, $G$                    | 80.1938 GPa |
| <b>Yielding</b>                       |             |
| Yield stress, $\sigma_y$              | 450.0 MPa   |
| Rupture stress, $\sigma_\infty$       | 715.0 MPa   |
| <b>Hardening</b>                      |             |
| Hardening modulus, $H$                | 129.0 MPa   |
| Hardening saturation stress, $\eta$   | 16.92       |
| <b>Damage</b>                         |             |
| Damage strain threshold, $p_M$        | 0.0%        |
| Internal cracking threshold, $M_{cr}$ | 1.0         |
| Damage strength, $S_0$                | 3.5 MPa     |
| Damage energetic exponent, $s_0$      | 1.0         |

### 6.1.3 Load-deformation analysis

As a natural consequence of the applied loading, any downwards applied loading/imposed deformation causes bending of any beam. Thus, in the bending of a cantilevered beam, the applied downwards load at the free edge of the beam causes an incremental downwards displacement along the length of the beam,  $L_{beam}$ . In both the undamaged and damaged plasticity simulations, the loading causes an initial state of three-dimensional stress in the beam, as is shown in Figure 6.2 as the downwards deformation increases from  $u_z = 0 \text{ m} \rightarrow u_z = 1 \text{ m}$ .



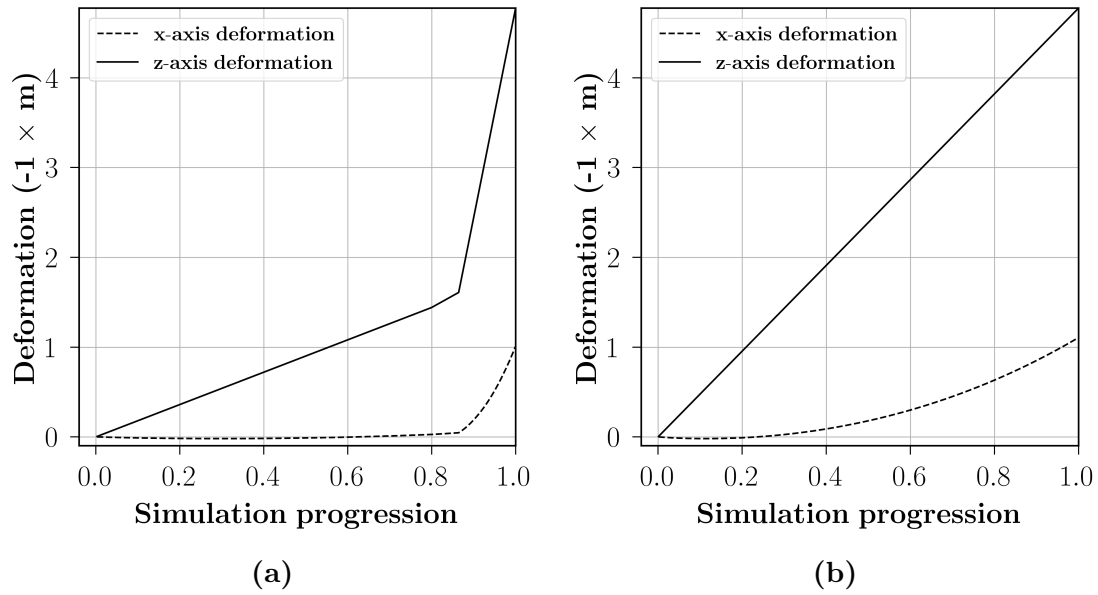


**Figure 6.2:** Deformation in the  $z$ -axis (bending) compared with deformation in the  $x$ -axis from  $u_z : 0\text{ m} \rightarrow 4.776\text{ m}$ . Left-side is the damaged plasticity simulations and right-side is the undamaged plasticity.

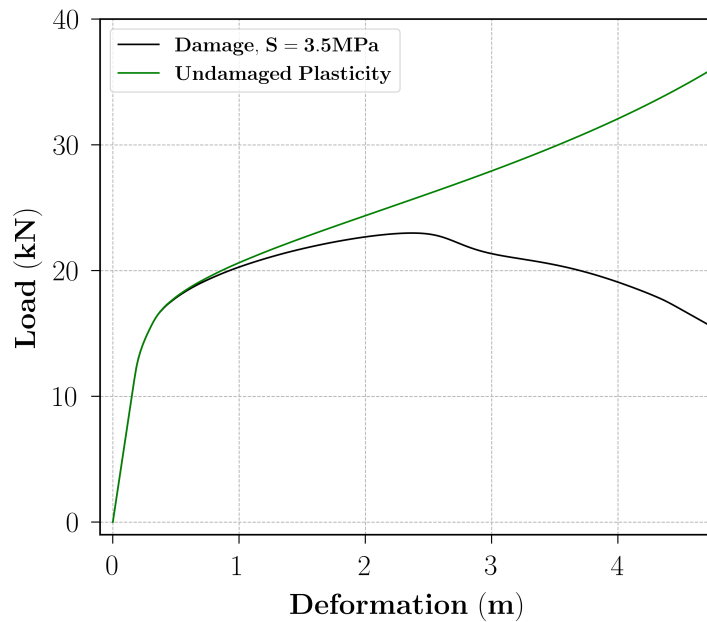


**Figure 6.3:** Damaged *vs* Undamaged Plasticity, Load *vs* Deformation in the Vertical  $z$ -axis up to vertical displacement  $u_z = 4.776\text{ m}$  at Point  $p_0$ .

As deformation in the  $z$ -axis (vertical) exceeds approximately  $1.0\text{ m}$ , a state of direct compressive deformation of the axial dimension in the beam is induced in both simulations and this is shown in Figure 6.2); both the damaged plasticity and undamaged plasticity models exhibit a considerable amount of  $x$ -axis compression (i.e. shortening along the axial dimension of the beam). Figure 6.2 also shows how the damaged simulations are generally more time-intensive — the simulation progression is scaled from start at value 0 in the graph to the end with value 1.

It is notable for the damaged simulation that there is significant damage softening behaviour in the beam as direct compressive deformation is induced, as seen by the continually decreasing  $\partial P_z/\partial u_z$  curve as  $z$ -axis displacement proceeds from a value of  $u_z \approx 2.365m$  to the end of the simulation as illustrated in Figure 6.3.

The maximum load point is also observed as occurring earlier in the damaged scenario and the damaged beam model carries less load due to the cumulative damage that occurs throughout its plastic load-deformation regime. Furthermore, the damaged simulation observes a loss in load-carrying capacity faster than it would with damage being unaccounted for. This behaviour is as expected and is shown in Figure 6.3 and Table 6.2 — in general, a damaged material carries load for shorter amounts of time than undamaged materials [25].

**Table 6.2:** Material behaviour at peak loading at Point  $p_0$ .

| Scenario           | Maximum Load, $P_{max}$ | $z$ -axis Deformation at $P_{max}$ |
|--------------------|-------------------------|------------------------------------|
| Pure Plasticity    | 36.194 kN               | 4.776 mm                           |
| Damaged Plasticity | 22.983 kN               | 2.370 mm                           |

#### 6.1.4 Analysis of stress and strain localisation

It is helpful to compare the stresses and strain developed in the material using the damaged and undamaged plasticity constitutive laws, respectively. With the cantilever beam model, the traction applied at the cross-section of the free edge causes bending, as the load and its accompanying turning effect (due to the full fixity at the fixed end of the beam) is transferred through the beam and to the support, which must then induce internal reactions at the loading/support as this load is transferred.

Thus, it is possible to observe and predict the regions in the beam that may be subject to the highest amounts of stress and strain, as well as the areas in the beam that are damaged. In Figure 6.5, it may be observed that at lower displacements, there is the prevalence of plastic/weakness zones in the structure by assessing the damage plot. Accumulated plastic strain induced in the damaged cantilever beam at  $u_z = 2.365 m$  is also shown, which indicates that the highest amount of strain is observed in the unsupported region of the beam immediately aft of the fixed end as shown in Figure 6.6.

It may also be observed that in both cases shown in Figure 6.7 and Figure 6.8, the maximum stress induced in the beam is at most proximal to the support fixity. The maximum stress must occur in the region in the beam that is immediately aft of the support, approximately within a distance of  $0.2 m$  from the support; these regions

are closest to the fixed support. This behaviour is typical of overhanging structural elements, as failure is often observed immediately aft of the support where bending moment and stresses are highest. Furthermore, the extension noticed induces the largest stresses at the support.

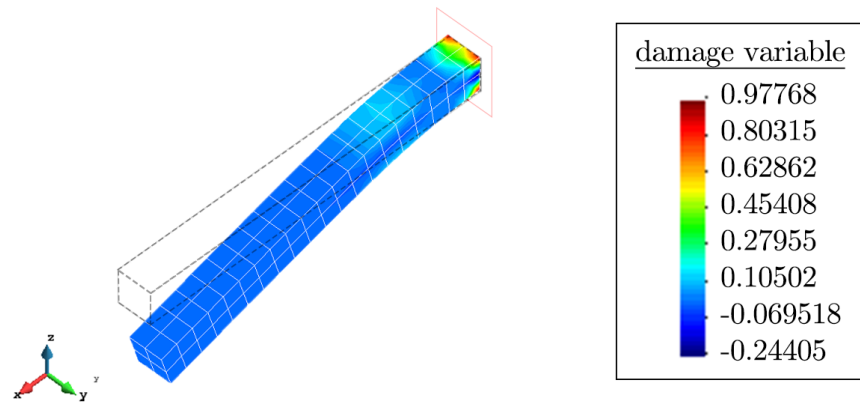


**Figure 6.4:** Smoothed damage variable contour plot for the cantilever beam model at vertical displacement  $u_z = 2.365 m$ . Damaged plasticity with isotropic hardening.

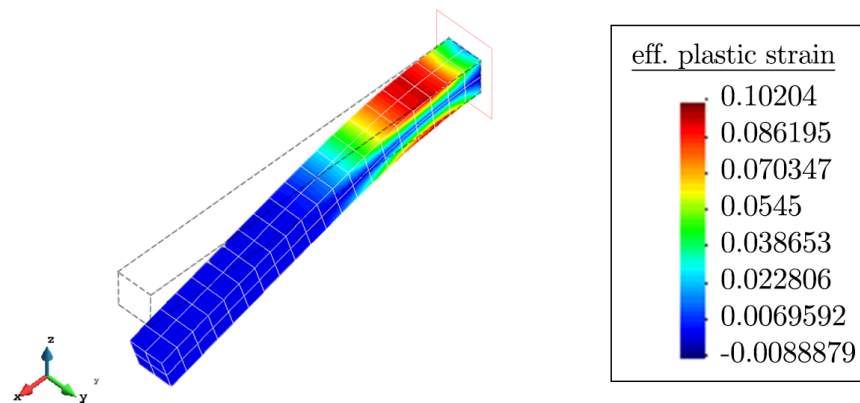


**Figure 6.5:** Equivalent plastic strain smoothed contour plot for the cantilever beam model at vertical displacement  $u_z = 2.365 m$ . Pure plasticity with isotropic hardening.

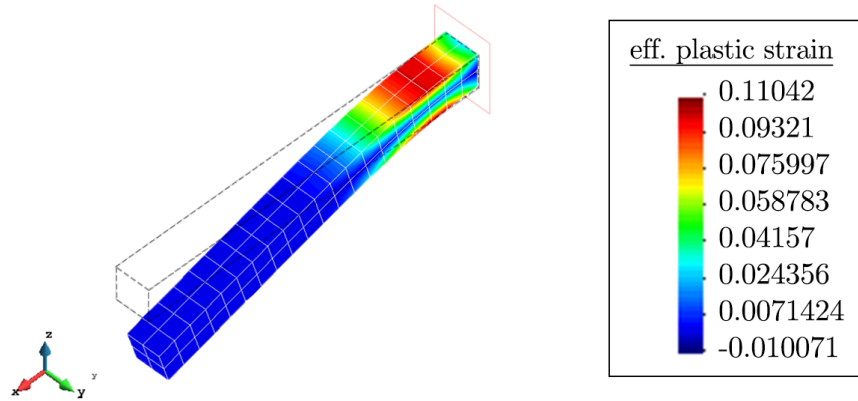


**Figure 6.6:** Equivalent plastic strain smoothed contour plot for the cantilever beam model at vertical displacement  $u_z = 2.365$  m. Damaged plasticity with isotropic hardening.

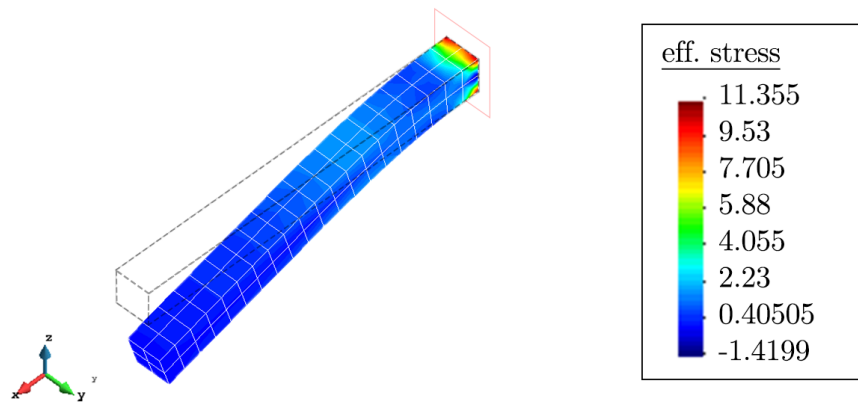


**Figure 6.7:** Effective stress plot smoothed contour plot for the cantilever beam model at vertical displacement  $u_z = 2.365$  m. Pure plasticity with isotropic hardening.

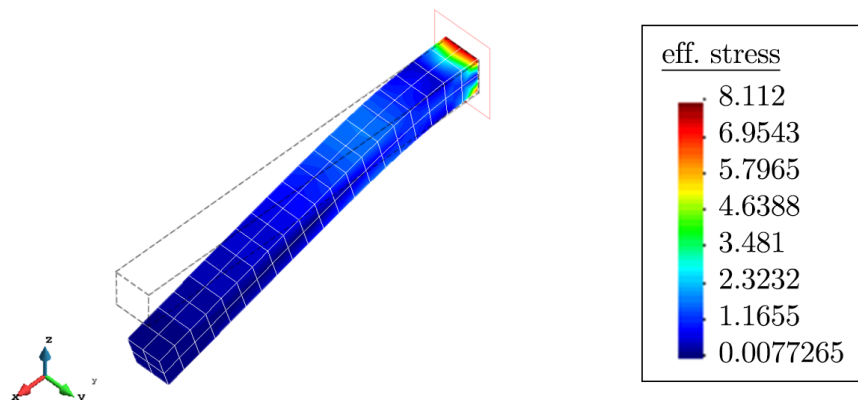


**Figure 6.8:** Effective stress plot smoothed contour plot for the cantilever beam model at vertical displacement  $u_z = 2.365$  m. Damaged plasticity with isotropic hardening.

## 6.2 3-point bending of simply supported slender square bar

### 6.2.1 Problem description

This example follows from a similar example assessed by Mohamad-Hussein & Shao [31] in which they modelled concrete. However, only the general analytical principles will be employed here; the damage laws and framework in [31] are different to that proposed in this study.

Square bars are often used as standard test specimens in the field of structural engineering to test the material properties of metallic and non-metallic components, such as mild steel, concrete and other composite materials. Thus an arbitrary metallic material is assumed as the modelled continuum in this example, and the material properties will be shown.

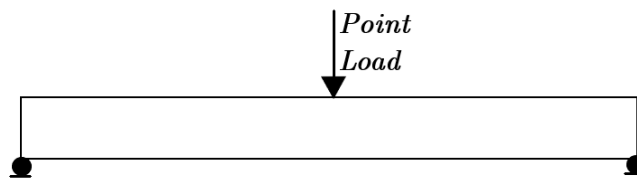


**Figure 6.9:** Schematic representation of the slender bar bending example.

Furthermore, the significance of this 3-point bending example is to compare the effect that the damage strength parameter may have on the overall load-carrying capacity of a simply supported slender bar in pure bending. In addition, the requirement and objective of simulating 3-point bending in a slender member is to provide qualitative analysis on the potential weak zones in a 3-point bending test by utilising the post-processed results of simulations run with the implemented material damage model.

The essential configuration of this example is shown in Figure 6.9 and will be further elaborated in Section 6.2.3. It must be observed that for this analysis, the damage variable remains unrestricted in its evolution.

### 6.2.2 Material properties

Ductility is ensured in that rate effects are ignored. Damage commences as soon as plasticity commences. This applies to the strain/work hardening in this scenario as well. As it pertains to elasticity, the arbitrary material has an Elastic modulus,

**Table 6.3:** Material properties of slender square bar.

| <b>Elasticity</b>                               |                 |
|---|-----------------|
| Bulk modulus, $K$                               | 38.8889 GPa     |
| Shear modulus, $G$                              | 29.1667 GPa     |
| <b>Yielding</b>                                 |                 |
| Yield stress, $\sigma_y$                        | 243.0 MPa       |
| Rupture stress, $\sigma_\infty$                 | 243.0 MPa       |
| <b>Hardening</b>                                |                 |
| Hardening modulus, $H$                          | 200.0 MPa       |
| <b>Damage</b>                                   |                 |
| Damage strain threshold, $p_M$                  | 0.0%            |
| Internal cracking threshold, $M_{cr}$           | 0.8             |
| <b>Damage strength values, <math>S_0</math></b> | <b>1.50 MPa</b> |
|   | <b>1.25 MPa</b> |
|   | <b>1.00 MPa</b> |
| Damage energetic exponent, $s_0$                | 1.0             |

$E = 70.0$  GPa and a *Poisson's* Ratio,  $\nu = 0.20$ . In this scenario, the hardening is assumed as isotropic linear hardening. The material properties for the *von Mises* elasticity applications are shown as in Table 6.3 together with those relevant to *Lemaitre*-based damage and linear isotropic hardening.

### 6.2.3 Meshing and boundary conditions

The slender square bar has length  $L_{bar} = 3000$  mm, depth  $h_{bar} = 300$  mm. The bar is roller-supported - the two opposite ends of the bar are considered fixed in the  $z$ -direction. Thus, vertical displacement is completely restricted at the ends of the bar whilst allowing motion in the  $x$ -direction. This allows for free longitudinal deformation at the supported ends and disallow excessive stretching of the bar along its length. However, rigid-body translation in the  $x$ -direction (longitudinal direction) of the entire continuum of the slender square bar is restricted by introducing a fixity at the bottom of the bar at mid-span to serve this intent. Rigid-body translation is not part of the context with this study.

The FEM mesh is shown as in Figure 6.10, with 80 hexahedral volume elements and 172 quadrilateral surface elements. Plane strain conditions are enforced by restricting all degrees of freedom in the transverse  $y$ -direction. Effectively, the part of the bar necessary for this analysis is that which is extant in the  $xz$ -plane.

To facilitate bending, a downwards vertical concentrated load is applied at the bar mid-span as shown in Figure 6.10. In order to control the evolution of displacement in this model, the FEM mesh is displacement-controlled at the load point as shown

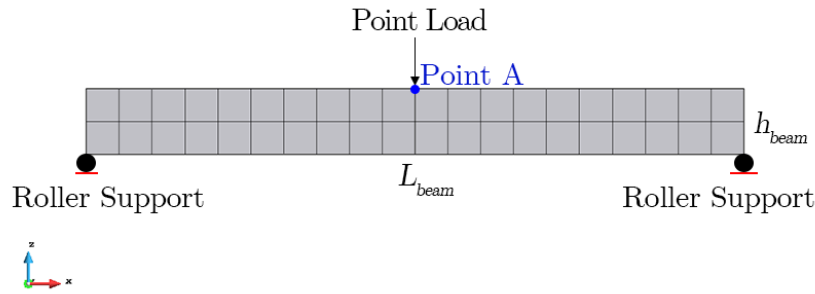


**Figure 6.10:** Mesh, problem configuration & boundary conditions. The roller-supported bar model used a 3D mesh of 80 hexahedral volume elements and 172 quadrilateral surface elements.

in the cross-section of the bar such that the displacement is always at a maximum at a point on the bottom of the member at mid-span. The problem is post-processed in SESKA, and boundary conditions are discretised in GiD.

### 6.2.4 The effect of damage energetic strength on load-carrying capacity

It is possible to assess the effect of the damage energetic strength variable,  $S_0$ . This variable is a thermodynamic property as is mentioned in Section 4.7 in that it varies with temperature. Ductile materials at higher temperatures will have lower damage strength, as material particles hold higher energy quanta and thus require little in the way of displacement to trigger micro-defect nucleation in the microstructure. However, this model is isothermal — dynamic temperature effects are ignored.

Still, this study will select values for the damage energetic strength. These were outlined in Table 6.3 as  $S_0 = 1.50$  MPa, 1.25 MPa and 1.00 MPa. By analysing the damage laws, one may predict that the lower the value of the damage strength, then the lower the overall load-carrying capacity of the bar at any given displacement within the plastic range of stress-strain and load-deformation behaviour. Furthermore, as seen in [30], 3-point beam bending yields a bell-shaped load-deformation curve; this is due to the induction of plasticity and then a gradual material softening as the deformation increases.

In Figure 6.11, the load-deformation analysis of this problem is illustrated. It is clear that as deformation increases from 25 mm, all three iterations of the model exhibit gradual plastic behaviour. However, at the top of each load-deformation plot, it is observable that a loss of load-carrying capacity is prevalent. As is

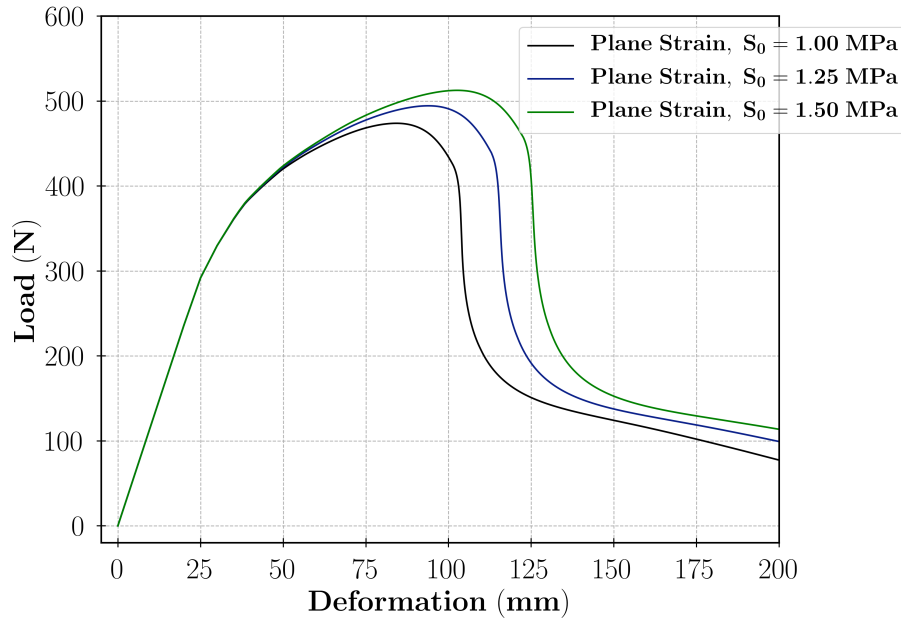


**Figure 6.11:** Damaged *vs* Undamaged Plasticity, Load *vs* Deformation in the  $z$ -axis up to vertical displacement  $u_z = 200$  mm at Point  $p_0$ .

seen with the cantilever beam tip bending example, damaged plasticity generally simulates lower loads for the same displacement.

**Table 6.4:** Material behaviour at maximum loading at Point A.

| Scenario         | Maximum Load, $P_{max}$ | $z$ -axis Deformation at $P_{max}$ |
|------------------|-------------------------|------------------------------------|
| $S_0 = 1.50$ MPa | 512.61 kN               | 102.61 mm                          |
| $S_0 = 1.25$ MPa | 494.43 kN               | 93.88 mm                           |
| $S_0 = 1.00$ MPa | 473.81 kN               | 84.22 mm                           |

With damage strength value  $S_0 = 1.50$  MPa, the damage progresses slower than the damage strength values  $S_0 = 1.25, 1.00$  MPa as is observed in Figure 6.11. That is the same for the comparison of the bending bar iteration with damage energetic strength  $S_0 = 1.25$  MPa compared to that of  $S_0 = 1.00$  MPa. Overall, the loss of load-carrying capacity is less exaggerated in materials with higher damage strength in contrast to those with lower damage strength values as would be expected as per the fundamental nature of material damage — material damage tends to progress faster in weaker materials or materials with pre-existing micro-voids when in tension or bending loading conditions.

The onset of softening is observed at different vertices for each iteration of the damage energetic strength, as is shown in Figure 6.11 and Table 6.4. In general, the behaviour predicted by the model is expected, and qualitatively, it fits in with the general pattern of the load-deformation relation in 3-point bending tests as is shown in [31].



### 6.2.5 Analysis of damage evolution and cracking

Figure 6.13 shows the *smoothed damage variable* line plot for  $S = 1.25$  MPa at Point A, which is the load point on the bar specimen undergoing 3-point bending in this model. This particular illustration indicates that damage continues to evolve from a vertical downwards displacement of 25 mm and through to the end of the simulation at 200 mm.

The *smoothed damage value*,  $M_{sm}$  is not restricted in this simulation and exceeds the value of 1.0. However, It must be noted that internal (*Gauss* integration point) cracking detection is observed at a vertical displacement of 115.16 mm — the internal cracking threshold was predefined as  $M_{cr} = 0.8$  in Table 6.3. The value of the *smoothed damage variable* holds the value of 0.9914 at this displacement at the load point (Point A).

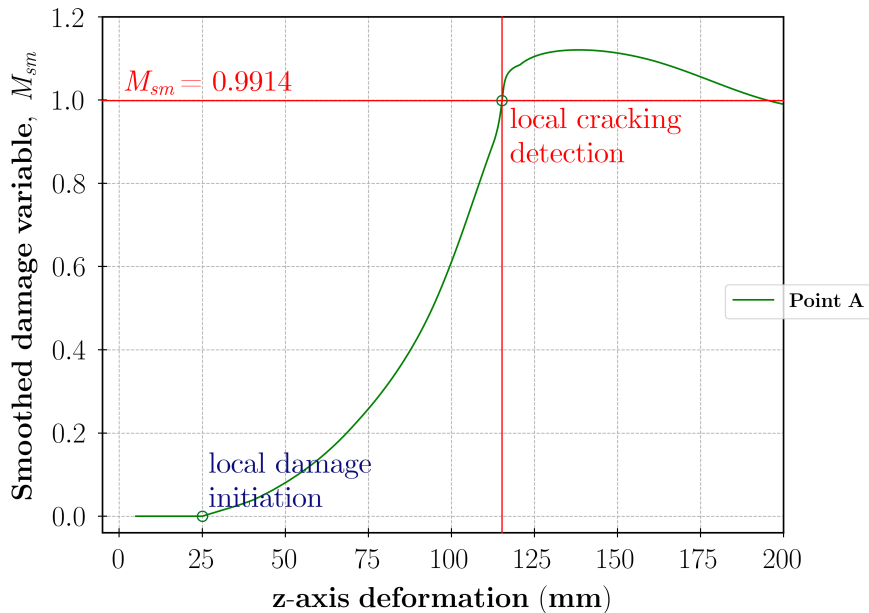


**Figure 6.12:** A line plot of the evolution of *smoothed damage variable* at Point A on the bar *vs* the *z*-axis deformation (downwards) at Point A on the bar.  $S = 1.25$  MPa.

Furthermore, Figure 6.13 shows the nature of the time-relative evolution of the vertical displacement and the *smoothed damage variable* at the load point (Point A). It is evident from this graph that the damage evolution is highly non-linear in all phases. Qualitatively, the first phase of the simulation indicates much more time-consuming *Newton-Raphson* iteration steps, where the time increment is larger in comparison to the displacement increment, and the second phase indicates the opposite. Still, the damage evolution is highly non-linear compared to the linear evolution of displacement at Point A.

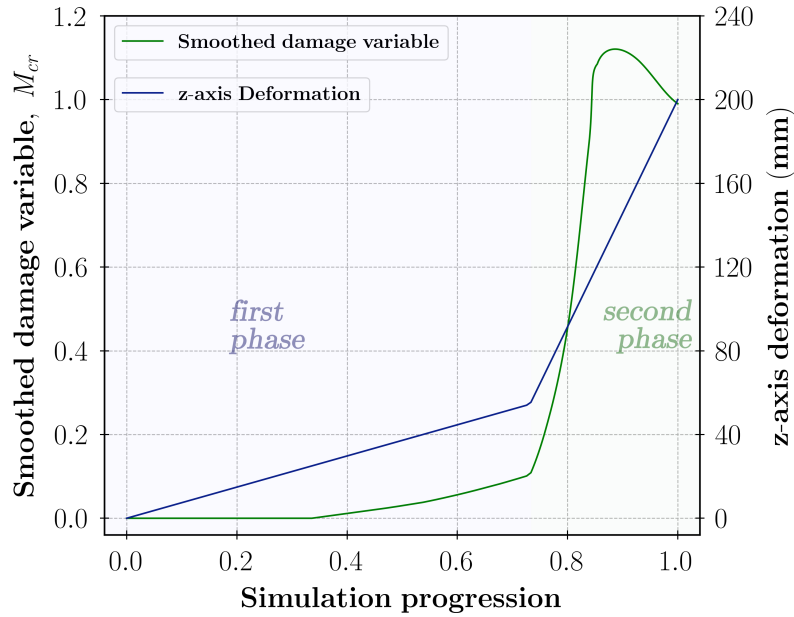


**Figure 6.13:** A line plot of the time evolution of *smoothed damage variable* and the *z-axis deformation* (downwards) at Point A on the bar.  $S = 1.25$  MPa.

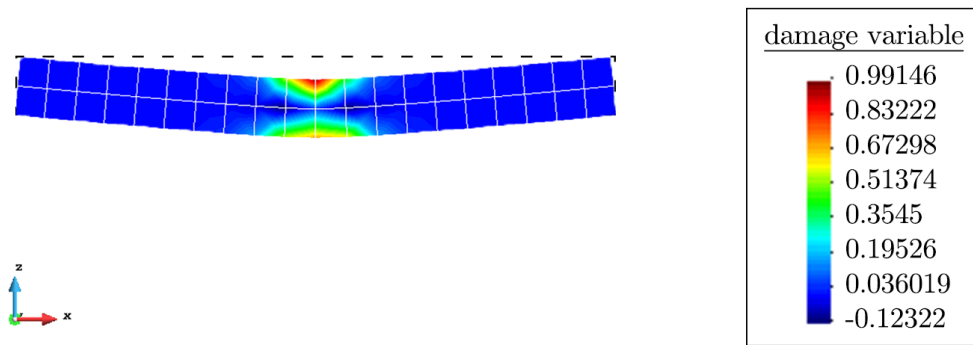


**Figure 6.14:** *Smoothed damage variable* contour plot for the simple beam model at vertical displacement  $u_z = 115.16$  mm. Damaged plasticity with  $S_0 = 1.25$  MPa.

## 6.2.6 Generalised damage distribution in the bar

The general nature of damage distribution in the bar is shown in Figure 6.15 at  $z$ -axis displacement of 100 mm and damage strength,  $S_0 = 1.00$  MPa. The material damage is highly concentrated towards the mid-span of the bar — specifically around Point A. This strongly indicates that the region around Point A is a potential failure/weakness zone. The data for damage strengths  $S_0 = 1.25$  MPa and  $S_0 = 1.50$  MPa are in Figure 6.16 and Figure 6.17, respectively.

Thus, it is possible to observe the regions in the bar that may be considered as weak zones and to compare this qualitatively to previously observed results in similar testing/simulations from literature. The plastic-damaged zones are at the load application point as there is the prevalence of plastic/weakness zones in the member by assessing the damage variable plot contour plot. This is due to the fact that the bar is in a state of compression in the top of the beam. Coincidentally, bending a bar in this manner produces tension in the bottom portion of the member. Thus, it is observable how the damaged zones are also in the bottom part of the bar at mid-span. This is in conjunction with the results in [31].

Furthermore, shown in Figure 6.18 is the line plot of the *smoothed damage variable* vs the  $x$ -axis distance from midspan. This information is retrieved for a  $z$ -axis displacement of  $u_z = 100 \text{ mm}$  in the bar. This graph also compares the damage concentration for each of the different values of  $S = 1.00, 1.25, 1.50 \text{ MPa}$  as is illustrated.

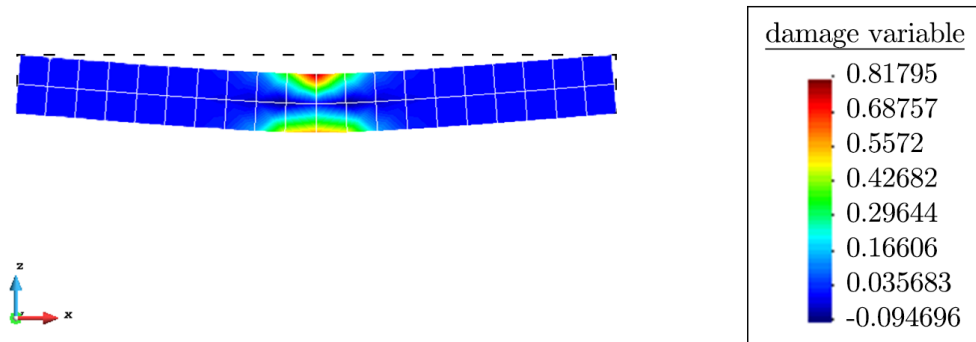


**Figure 6.15:** *Smoothed damage variable* contour plot for the 3-point bending bar model with  $S_0 = 1.00 \text{ MPa}$  at vertical displacement  $u_z = 100 \text{ mm}$ .

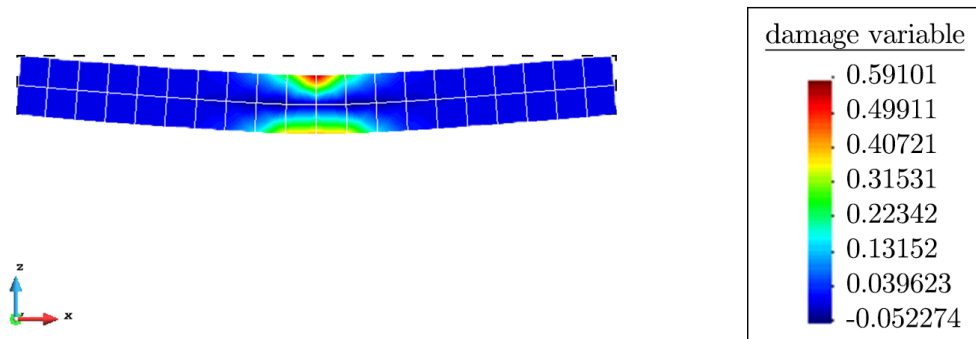


**Figure 6.16:** *Smoothed damage variable* contour plot for the 3-point bending bar model with  $S_0 = 1.25 \text{ MPa}$  at vertical displacement  $u_z = 100 \text{ mm}$ .

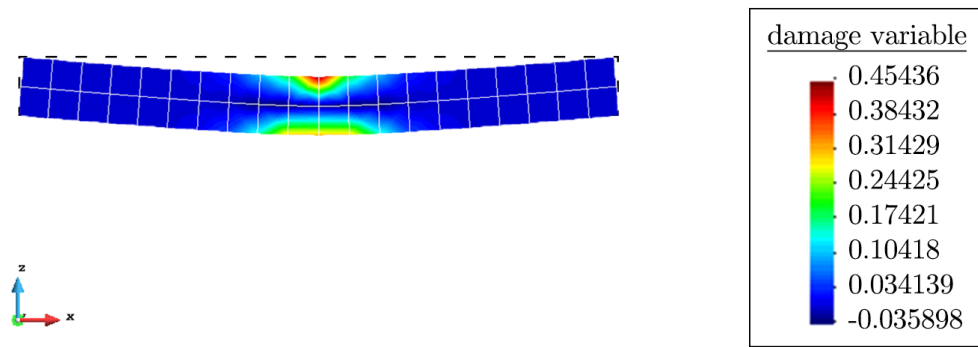


**Figure 6.17:** Smoothed damage variable contour plot for the 3-point bending bar model with  $S_0 = 1.50$  MPa at vertical displacement  $u_z = 100$  mm.

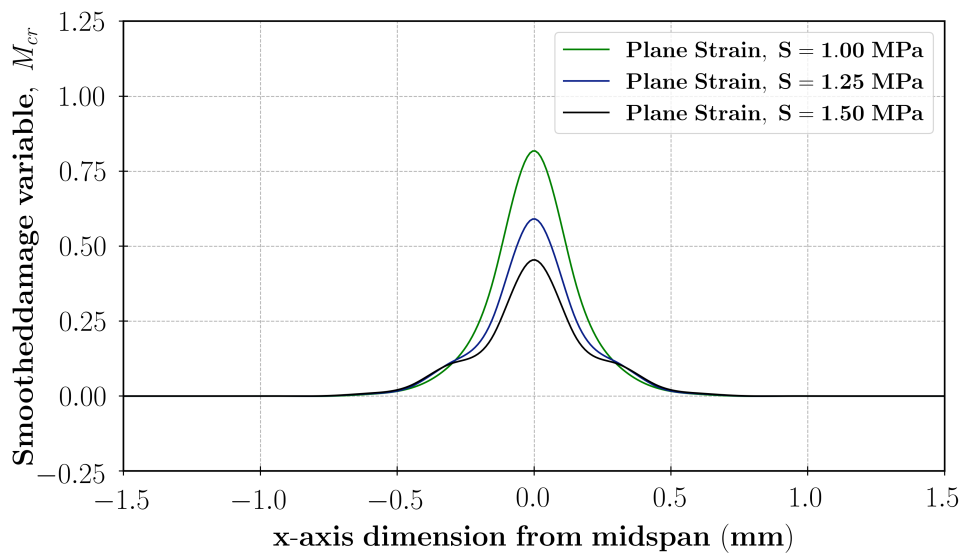


**Figure 6.18:** Smoothed damage variable line plot along the bar's  $x$ -axis dimension, with distance shown from the mid-span at vertical deflection of  $u_z = 100$  mm.

## 6.3 Uniaxial plane tension of 3D solid plates with different thickness

### 6.3.1 Problem configuration

In order to compare and contrast the specimen size dependency of this model, an example often used in literature for showcasing the capabilities of finite strain models is the uniaxial tensile testing of a plane plate. This example is similar to that in [44] and [5] which use a two-dimensional shell example to exemplify their implementation of *Lemaitre's* damage laws and use an entirely different evolution scheme damage behaviour. The example is also in [41] for viscoplastic two-dimensional shells.

Figure 6.19 provides the schematic representation of this example, which consists of a plate of height  $H_{plate} = 53.334 \text{ mm}$ , width  $W_{plate} = 12.826 \text{ mm}$ . The depth of the plate will be rendered at different values  $D_{plate} = 1.0, 2.0, 3.0 \text{ mm}$ .

Boundary conditions are as follows: both ends of the cylindrical bar are given a uniaxial displacement  $u_z$ , with no lateral constraint. Thus, there are no rigid fixities at either end. The uniaxially applied displacement is normal to the surface at each end. In order to maintain statical determinacy and remove any kinematic degrees of freedom, the plate is assumed to have rigid fixities coincident with each plane of symmetry. Thus, the vertical plane of symmetry embodies a lateral constraint, and the horizontal plane of symmetry embodies a vertical constraint on motion.

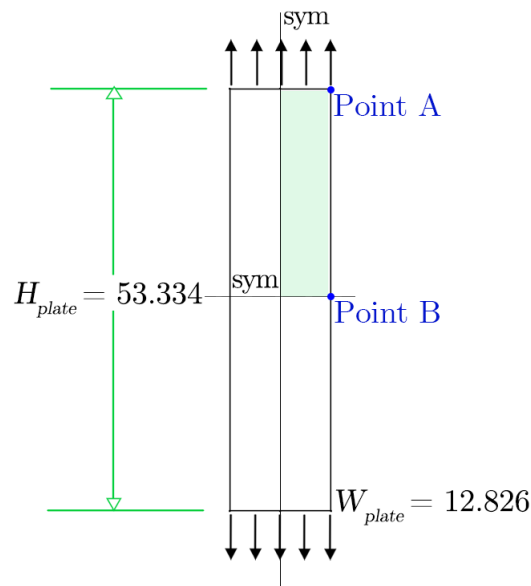


**Figure 6.19:** 2D schematic representation of the solid plane under tension example. (*Units = mm*)

### 6.3.2 Material properties

For this plate plane tension example, the material being analysed is steel, a ductile material for which the behaviour is well-established and material properties may be reasonably guessed through arbitrary methods and through literature. Damage onset is once again coincident with the onset of plastic yielding, as was the case in the examples in Section 6.1 and Section 6.2. Thus,  $p_M = 0.0\%$  for an observation of damage phenomena.

Work/strain hardening is also coincident with the onset of plastic yielding. The material properties for all iterations of this example are the same — all plate

thickness iterations have the same elasticity, plasticity and damage parameters and applications as in Table 6.5. Once more, non-linear exponential-based isotropic hardening laws are used to approximate strain hardening.

Omitted from Table 6.5 are the Elastic modulus,  $E = 206.9$  GPa and the *Poisson's* ratio,  $\nu = 0.29$ , which are not intrinsic to the implemented material model but rather are used to calculate the bulk modulus  $K$  and shear modulus  $G$  accordingly.

**Table 6.5:** Material properties of solid plate [44].

| <b>Elasticity</b>                      |             |
|--|-------------|
| Bulk modulus, $K$                      | 164.206 GPa |
| Shear modulus, $G$                     | 80.1938 GPa |
| <b>Yielding</b>                        |             |
| Yield stress, $\sigma_y$               | 450.0 MPa   |
| Rupture stress, $\sigma_\infty$        | 715.0 MPa   |
| <b>Hardening</b>                       |             |
| Hardening modulus, $H$                 | -12.924 MPa |
| Hardening saturation parameter, $\eta$ | 16.93       |
| <b>Damage</b>                          |             |
| Damage strain threshold, $p_M$         | 0.0%        |
| Internal cracking threshold, $M_{cr}$  | 1.0         |
| Damage strength, $S_0$                 | 1.25 MPa    |
| Damage energetic exponent, $s_0$       | 1.0         |

### 6.3.3 Meshing and boundary conditions

Only a quarter of the plate is discretised due to the existence of 2 planes of symmetry in Figure 6.19. Thus, the dimensions of the plate change to  $h_{plate} = 26.667$  mm, width  $w_{plate} = 6.413$  mm at the top of the the quarter portion of the plate and depth  $d_{plate}$ . Necking behaviour is expected to occur at the base of the quarter plate and thus, we induce a geometric imperfection for necking behaviour: the width is reduced to 98.1% at the base of the quarter plate. This reduction in width is applied linearly from a height of 6.413 mm above the base of the quarter plate portion and this constitutes a new problem definition and setup.

Given the new problem definition, two *Dirichlet* surface boundary conditions are applied to account for symmetry. To account for the  $xy$ -plane symmetry, a vertical ( $z$ -axis) fixity is applied at the base of the plate. A  $y$ -axis fixity is applied at the vertical face coinciding with  $yz$ -plane. The boundary conditions are shown in each figure. Furthermore, the entire volume is subject to an  $x$ -axis fixity to enable three-dimensional plane strain conditions. The tensile loading is applied by placing a *Neumann* surface traction condition at the top of the quarter plate, controlled by

vertical displacement controls at each corner of the loaded surface to assure that the entire surface is deformed uniformly.

For the scenario with  $d_{plate} = 1.0 \text{ mm}$ , the plate is meshed roughly with 50 volume elements and 135 surface elements as shown in Figure 6.20. There are 100 volume elements and 220 surface elements for the scenario with  $d_{plate} = 2.0 \text{ mm}$  which is shown in Figure 6.21. Lastly, Figure 6.22 shows the plate is meshed with 150 hexahedral volume elements and 305 surface elements for the scenario with  $d_{plate} = 3.0 \text{ mm}$ . All volume elements are hexahedrals and surface elements are quadrilaterals.

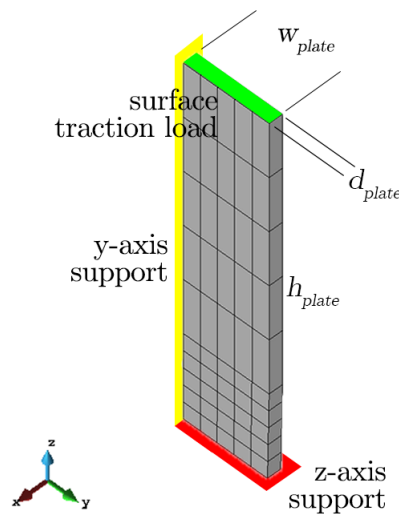


**Figure 6.20:** Mesh & boundary conditions in the quarter model of the plate in uniaxial tension with  $d_{plate} = 1.0 \text{ mm}$ . The fixity and displacement conditions are shown.

### 6.3.4 Load-deformation analysis

An applied surface tension at the top surface of the plates will cause an axial tensile deformation in the quarter plate in the  $z$ -axis. Due to the vertical  $z$ -axis constraint at the lower surface of the quarter plate and the lateral  $y$ -axis constraint, an accompanying transverse displacement is induced that varies with height along the  $z$ -axis dimension of the quarter plate. This is a virtue of the principle of incompressibility (volume preservation) of solid materials, which is the foundation of this damage implementation i.e.  $J = 1$ .

In Figure 6.23, yielding is observed at the same vertical displacement for the plate with thickness  $1.0 \text{ mm}$ ,  $2.0 \text{ mm}$  and  $3.0 \text{ mm}$ . This indicates that the axial yield strain is similar amongst all three plate thickness iterations. However, the yield stress is the same — the tensile yield load is larger with the thicker plate specimens.

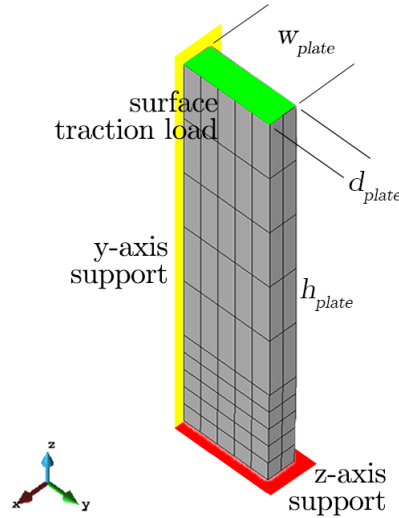


**Figure 6.21:** Mesh & boundary conditions in the quarter model of the plate in uniaxial tension with  $d_{plate} = 2.0 \text{ mm}$ . The fixity and displacement conditions are shown.

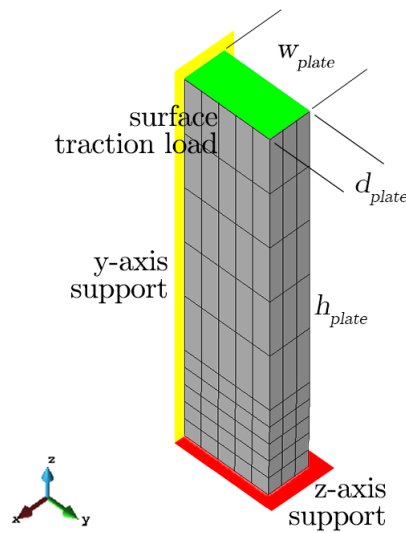


**Figure 6.22:** Mesh & boundary conditions in the quarter model of the plate in uniaxial tension with  $d_{plate} = 3.0 \text{ mm}$ . The fixity and displacement conditions are shown.

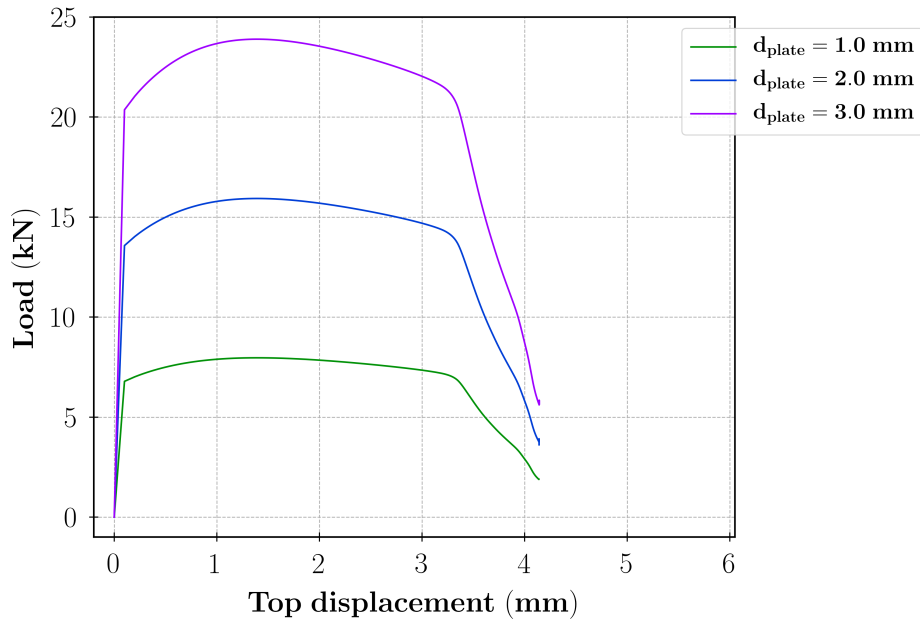
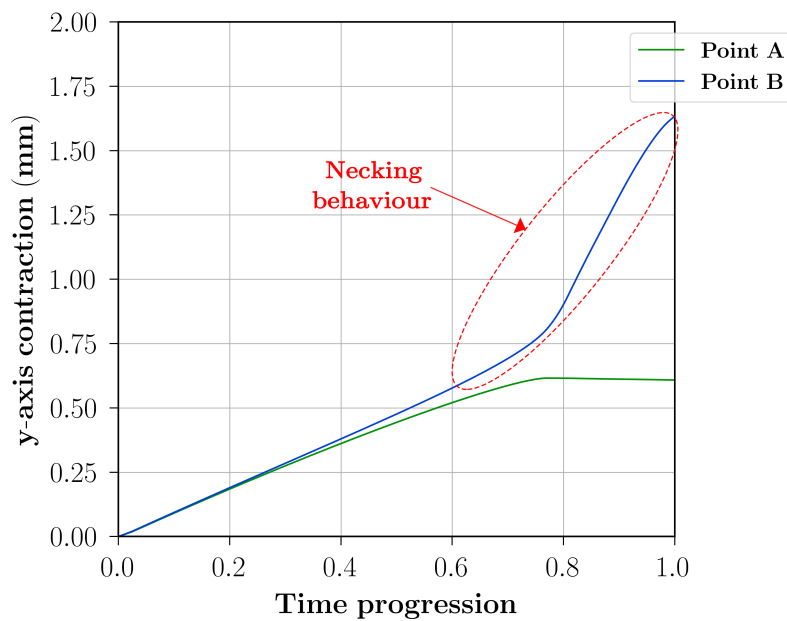
It is observable from Table 6.6 that the peak load induced in the specimen holds a larger value for the larger plate thickness  $d_{plate} = 3.0 \text{ mm}$  in contrast to the lower peak load in the smaller plates. This is in spite of the reality that the ultimate tensile strength of the material,  $\sigma_{\infty}$ , is the same for all  $d_{plate}$  iterations.

Observable in the damage softening behaviour of each plate thickness scenario is a steep drop-off in load-carrying capacity past the value of  $\approx 3.3 \text{ mm}$  vertical top displacement. Qualitatively, due to the nature of the plasticity simulation and convergence, it is not feasible to continue the simulation past a displacement value



**Table 6.6:** Material behaviour at peak axial loading.

| Scenario                      | Maximum Load, $P_{max}$ |
|-------------------------------|-------------------------|
| $d_{plate} = 1.00 \text{ mm}$ | 7.97 kN                 |
| $d_{plate} = 2.00 \text{ mm}$ | 15.93 kN                |
| $d_{plate} = 3.00 \text{ mm}$ | 23.90 kN                |

**Figure 6.23:** Load *vs* Deformation in the  $z$ -axis up to vertical displacement  $u_z = 4.14 \text{ mm}$  for a node at the loaded surface.**Figure 6.24:** Evolution of lateral displacement ( $y$ -axis displacement) showing necking behaviour at Point B at the base of the quarter plate through the simulation.

of 4.14 mm. Furthermore, there is no detectable cracking in this simulation as that is triggered automatically when a local integration point undergoes internal cracking controlled by the internal cracking threshold  $M_{cr}$  as shown in Table 6.5.

### 6.3.5 Analysis of necking and strain localisation phenomena

Necking is a mode of tensile deformation where a strain localisation is observed at relatively large deformations in a material volume [3]. Longer, slender members undergo necking due to a large length-width or length-thickness ratio; this phenomenon causes a significant reduction in the dimension of the thickness/width of the member. This phenomenon is also observed during the simulation of this solid plate model.

Figure 6.24 shows the onset of necking in the manner in which the lateral deformation at Point B ( $y$ -axis displacement) evolves through the simulation. It is clear that from a  $y$ -axis displacement of approximately 0.78 mm, the edge at the base of the aforementioned quarter plate contracts at a noticeably higher rate than the edge at the top of the modelled plate.

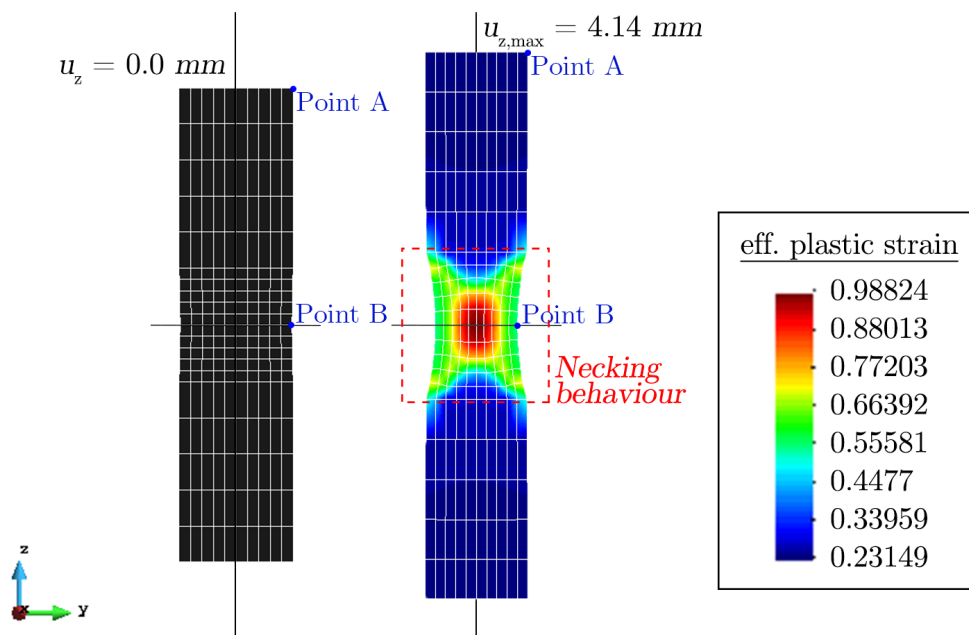


**Figure 6.25:** Deformation profile and strain localisation plot of the full solid plate model as viewed in the  $yz$ -plane. On the left is the undeformed plate and on the right, the deformed plate at  $u_{z,max} = 4.14 \text{ mm}$ .

Shown in Figure 6.25 is the profile of the full plate model. It is clearly observable that the middle portion of the plate undergoes necking phenomena, which further confirms the realisations of the data provided in Figure 6.24. It also coincides with

---

the concept of necking in that at large deformations, and there is a noticeable contraction in the "width" dimension of the plate.

Notably, due to the universal  $x$ -axis fixity, the necking observed in the plate for the different plate thickness/depth iteration 1.00 mm, 2.00 mm and 3.00 mm is identical. The entire contractile strain is applied only to the  $y$ -axis dimension. This essentially flattens the specimen, and thus the strains and stresses are identical regardless of depth/thickness. In [44], similar material behaviour is observed for two-dimensional shell plates where necking is observed at relatively high displacements.

# Chapter 7

## Discussions

### 7.1 Continuum damage mechanics framework

Continuum mechanics involves the derivation of valid fundamental formulations that characterise the material behaviour of all continuous materials [29]. These fundamental relations lead us to the constitutive formulae. As a result of the principles of continuum mechanics, field quantities such as traction and stress are represented by continuous functions within the space and the time in which they are computed.

This is clearly an issue in the case of continuum damage mechanics, which combines continuum theory and material damage theory and removes the ability of any model using these mathematical approaches to accurately model material behaviour under fracture. Furthermore, the concepts of continuity in continuum mechanics limit the scope of the proposed damage model to continuous materials; the model may is not able to discretely and physically visualise and characterise discontinuities in materials such as voids and cracks.

However, this proposed material model/implementation accounts for the fact that discontinuities are not discretely modelled, rather are smeared. In this sense, if a point in the material is damaged, then the damage is smeared onto neighbouring materials as part of the mechanical behaviour of the material [4]. This also explains a slight discrepancy in the plotting of the smoothed (smeared) damage variable  $M_{sm}$  vs the values of the local damage variable  $M$  during simulations. The damage variable is effectively smoothed over the volume elements from a combination of locally damaged material points within an element.

It must be mentioned that the damage variable is universally applied and can be universally applied to all sorts of materials, ductile, brittle or otherwise. As this study is geared towards assessing material damage and not fracture, the utilisation of a damage variable is appropriate and works as intended.

## 7.2 Constitutive damage coupling *vs.* finite element damage coupling

Material damage is strongly coupled in the constitutive framework only, in that the material stress is degraded as damage is evolved. Furthermore, the thermodynamic concept of internal potential couples the damage residual  $(1 - M)$  as part of the elastic stored energy  $\Psi_{int}(\mathbf{C}_{el}, M)$  term (see Section 4.5 and Section 4.6); the damage residual degrades the elastic modulus [25]. All this has the implication of embedding the effects of the loss in overall elastic storage energy capacity and the loss in load-carrying capacity.

In the finite element framework of SESKA, this damage residual is not included in any of the weak forms as it is already accounted for in the computation of the 2<sup>nd</sup> Piola-Kirchhoff stress and its consistent algorithmic tangent operator.

## 7.3 Yield criteria and associated flow rule

With the *von Mises* yield criterion as chosen for this implementation, the onset of plastic yielding is defined as when the  $J_2$  invariant of the *material* stress deviator exceeds the critical value — the critical value is assumed to be a function containing the yield strength and/or hardening parameter with *isotropic* and/or *kinematic* hardening [45]. This implementation uses the *Mandel* stress tensor  $\Sigma$ , for which the  $J_2$  invariant is defined in Section 4.7.1 as

$$J_2 = \frac{1}{2} \|\text{dev}(\Sigma)\|^2.$$

It is clear that the  $J_2$  invariant is independent of the hydrostatic pressure component when constructing a stress tensor — this is also known as pressure-insensitive. This has the clear drawback that the *von Mises* yield criterion cannot reasonably simulate compression and tension in tandem, as for many a material, the tensile and compressive yield strength tend to deviate from one another. Even as per this implementation, this could've been remedied by adding a tensile/compressive behaviour switch.

Furthermore, the *von Mises* yield function used in this model is also cohesion-insensitive and thus does not facilitate for analysis of materials whose material behaviour is highly cohesion-dependent such as soft rocks and soils. More suitable for such cases would be a yield function based around the *Drucker-Prager*

yield concepts, which would require quite rigorous work to fit within the *Newton-Raphson* parametric update scheme.

## 7.4 *Newton-Raphson* procedure

A potential disadvantage of the *Newton-Raphson* update scheme for the plastic multiplier as outlined in Section 5.4.3 is that the function tangent used in the *Newton-Raphson* scheme, in this case the yield function tangent  $(\partial f/\partial \lambda) < 0$ , it can never assume a null value as it would be mathematically impossible — the tangent would be horizontal and thus would not cross the solution space (Figure 5.2) for the plastic multiplier  $\lambda$  and the procedure would be unable to estimate  $\lambda$ .

Furthermore, it is physically impossible for  $(\partial f/\partial \lambda) = 0$  as it follows that for as long as the loading is applied in the inelastic regime, then the inelastic phenomena must also continue to evolve. Moreover,  $(\partial f/\partial \lambda) \not\geq 0$  as changing signs would lead to a larger than usual residual for the function in the estimation procedure. However, in the physical and phenomenological sense,  $(\partial f/\partial \lambda) > 0$  would imply that there is a reversal of the flow of plastic potential, and thus reversing the flow of entropy which is physically impossible.

Despite these limitations, the proposed material damage model makes several concessions to counteract this effect. Firstly, the yield function tangent is restricted:  $(\partial f/\partial \lambda) < 0$ . Furthermore, the yield function is allowed to approach zero to refine the simulation and retain reasonable convergence requirements:  $(\partial f/\partial \lambda) \rightarrow 0$  for lower and finer time and loading increments, as such an instance allows for finer resolution of the estimation procedure as well.

## 7.5 Predictive capability of this model

Predictably, the mid-height of a long, thin specimen is typically the weak zone in both uniaxial tension and compression. In compression, the weakness is observable in that it causes buckling, which is the lateral concentrated outward straining of the middle portion of a member. This is usually observed in constrained compression scenarios. In a state of tension, the member may exhibit a concentration of strain near or at mid-height of the member, and in particular on near the edges at the mid-height, which causes a contraction of the width dimension of the member and this is known as necking.

In 3-point bending, the development of a plastic-damage hinge in the middle portion of the specimen follows from the development and localisation of stress in the middle part of the bending specimens — the mid-length of the member. Furthermore, in cantilever beam bending, it is possible to view the plastic-damage hinge developed near the fixed support of the beam as in Section 6.1 under large deformations. The model accurately represents these zones as the weak/damaged zones and does not necessarily follow the strain localisation but follows the stress localisation. Qualitatively, this is accurate and all these predictions are within the predictive capability of this model.

## 7.6 Effect of the damage energetic strength parameter

Predictably, the material damage model shows that the damage variable is higher in materials with lower values of the damage strength parameter (i.e. weaker ductile materials). Thus, the damage strength parameter  $S_0$ , which is simply an arbitrary albeit consistent material property that characterises the propensity of a material to undergo damage softening, should have a different value in this implementation compared to that in [44]. This is clear by assessing the results in [2] as well.

The comparison of the effect of damage strength is further extended to this observation of the differing values of the damage variable for each of the damage strength situations considered as per the initial problem description and material properties. In general, similar bar/beam bending examples showcased in other non-local damage examples, albeit with different material properties and a different implementation of damage evolution, show a sharp concentration of damage at the bar's mid-span [31].

# Chapter 8

## Future work and study

### 8.1 *Drucker-Prager* yield criterion

Ducker and Prager [6] proposed their yield criterion, the *Drucker-Prager* yield criterion as a smooth approximation case for the classical *Mohr-Coulomb* yield law. The *Mohr-Coulomb* yield law is commonly used in geotechnical and concrete engineering, as well as in geology to describe the stresses in soft materials [5]. Softer materials tend to be highly pressure-sensitive, as well as including the material property of cohesion strength.

The *Drucker-Prager* improves on the smoothness of *Mohr-Coulomb* yield law, and states that "plastic yielding commences once the  $J_2$  invariant of the stress deviator and the hydrostatic portion of the stress tensor exceeds the cohesion strength". This is in contrast to the *von Mises* yield criterion, where yielding is controlled by the yield strength and strain/work hardening. This is possible to implement in SESKA, in particular when assessing brittle damage and is a good basis for future work and study where our material damage model may include the *Drucker-Prager* yield criteria. Fundamental thermodynamics concepts such as the principle of maximum plastic dissipation are unlikely to change. However, the evolution of plasticity may change accordingly.

### 8.2 Implementation of meso-scale void-closure effects

The implementation described in this paper proceeds by way of discretising local points, otherwise known as *Gauss* integration points. These points are defined in the reference and intermediate configurations of the material under deformation — in this paper, this is referred to as either mesoscale damage, local damage or internal local damage. Conceptually, for each local point in compression, it may close cracks rather than open other cracks near the particular local point [24] — this is known as the void-closure effect. In compression, each material point is pushed closer to another material point, and the work done in doing this is what manifests as compressive stress in the material.



So as for further study, the closure effect can be implemented into this existing model by splitting the stress tensor into exclusively tensile and compressive portions in order to apply the closure effect to only the compressive portion of the material stress. This would also achieve the goal of normalising the pressure-insensitivity and stress-regime independence of the *von Mises* yield criterion.

### 8.3 Implementation of viscoplastic damage

Viscoplasticity, by definition, describes the plastic behaviour of solids but is entirely dependent on the rate of deformation. This would easily include a mechanical description of damage for brittle materials. Brittle and quasi-brittle materials tend to exhibit rate-dependent material behaviour, and viscoplasticity is inherently rate-dependent. This would easily fit in the current constitutive framework for stress, strain and phenomenologically inelastic variables such as damage and hardening. Furthermore, the associative flow rule would be the same. However, the evolution of plasticity in the plastic multiplier would be markedly different.

An initial investigation into the feasibility of such an implementation produced the following: the plastic strain-rate tensor  $\mathbf{L}_{pl}$  is redefined as the *viscoplastic strain-rate* tensor  $\mathbf{L}_{vp}$ . All other continuum mechanics quantities remain the same. Algorithmically, the plastic multiplier would be computed using *Perzyna's* viscoplastic laws as described and rigorously derived in [34], [36], and [37]. The preliminary study of *Perzyna's* viscoplasticity laws in conjunction with the constitutive framework of the model described throughout this paper proposes the following equation for the plastic increment:

$$\Delta\lambda = \frac{\Delta t}{\omega} \left( \frac{\|\text{dev}(\bar{\boldsymbol{\Sigma}}_{n+1})\|}{\sigma_y(Z_{n+1})} \right)^N \quad (8.1)$$

whereby the parameter  $N$  is the rate sensitivity parameter, and the parameter  $\omega$  is directly related to the viscosity of the material. The time increment  $\delta t$  is crucial in the algorithmic implementation of viscoplasticity, whilst it is trivial and only used to store computational variables with the implementation of rate-dependent plasticity and damage as described in this thesis paper. Further study is needed to consolidate this preliminary knowledge and further work is required to fully implement the concept of viscoplasticity and thus brittle damage into SESKA using some of the damage concepts in this study.

# Bibliography

- [1] Adkins, W. A. & Davidson, M. G.. 2012. *Ordinary Differential Equations*. Springer Science+Business Media: New York, USA.
- [2] Areias, P. M. A., Cesar de Sa, J. M. A. & Conceicao Antonio, C. A.. 2003. A gradient model for finite strain elastoplasticity coupled with damage. *Finite Elements in Analysis & Design*. 39(2003): 1191-1235. doi: 10.1016/S0168-874X(02)00164-6.
- [3] Bridgman, P. W.. 1952. *Studies in Large Plastic Flow and Fracture*. McGraw-Hill: New York, USA.
- [4] de Borst, R.. 1987. Smearred cracking, plasticity, creep, and thermal loading - a unified approach. *Computer Methods in Applied Mechanics and Engineering*. 62(1987): 89-110. doi: 10.1016/0045-7825(87)90091-0.
- [5] de Souza Neto, E. A., Peric, D. & Owen, D. R. J.. 2008. *Computational Methods for Plasticity, Theory and Applications*. John Wiley & Sons: West Sussex, United Kingdom.
- [6] Drucker, D. C. & Prager, W.. 1952. Soil mechanics and plasticity analysis of limit design. *Quarterly of Applied Mathematics*. 10: 157-165. doi: 10.1090/qam/4829.
- [7] Erdmann, K. & Wildon, M. J.. 2006. *Introduction to Lie Algebras*. Springer-Verlag: London, United Kingdom.
- [8] Fermi, E.. 1956. *Thermodynamics*. Dover Publications: New York, USA.
- [9] Garrett, S. J.. 2015. *Introduction to Actuarial and Financial Mathematical Methods*. Elsevier: California, USA.
- [10] Gdoutos, E. E.. 2020. *Fracture Mechanics, an Introduction*. 3<sup>rd</sup> Ed. Springer Nature: Switzerland.
- [11] Hackett, R. M.. 2018. *Hyperelasticity Primer*. 2<sup>nd</sup> Ed. Springer International Publishing: Switzerland.
- [12] Hencky, H.. 1933. The Elastic Behavior of Vulcanized Rubber. *Journal of Applied Mechanics*. 1: 45-53. doi: 10.5254/1.3547545
- [13] Hofstetter, G. & Meschke, G.. 2011 (Eds.). *Numerical Modelling of Concrete Cracking*. CISM, Courses and Lectures. No. 532 (Jirasek, M.).
- [14] Holzapfel, G. A.. 2000. *Nonlinear Solid Mechanics, A Continuum Approach for Engineering*. John Wiley & Sons: West Sussex, England.
- [15] Hopkins, G.. 2014. *Highly Non-linear Post-buckling Analysis of Shell Structures*. OpenUCT: University of Cape Town, South Africa.
- [16] Hopkins, G.. 2017. *Growth, Modelling and Remodelling of Cardiac Tissue: A Multiphase Approach*. OpenUCT: University of Cape Town, South Africa.

- 
- [17] Krajcinovic, D. & Lemaitre, J.. 1987. *Continuum Damage Mechanics: Theory and Application*. Springer-Verlag: Wien, Austria.
- [18] Lai, W. M., Rubin, D. & Krempl, E.. 1993. *Introduction to Continuum Mechanics*. 3<sup>rd</sup> Ed. Pergamon Press.
- [19] Lai, W. M., Krempl, E. & Rubin, D.. 2010. *Introduction to Continuum Mechanics*. 4<sup>th</sup> Ed. Elsevier: Massachusetts, USA.
- [20] Lauterbach, B. & Gross, D.. 1998. Crack growth in brittle solids under compression. *Mechanics of Materials*. 29(1998): 81-92. doi: 10.1016/S0167-6636(97)00069-0.
- [21] Lax, P. D. & Terrell, M. S.. 2014. *Calculus with Applications*. 2<sup>nd</sup> Ed. Springer Science+Business Media: New York, USA.
- [22] Lemaitre, J.. 1985. A continuous damage mechanics model for ductile fracture. *Journal of Engineering Materials and Technology*. 107(1985): 83-89. doi: 10.1115/1.3225775.
- [23] Lemaitre, J. & Chaboche, J. L.. 1990. *Mechanics of Solid Material*. Cambridge University Press: Cambridge, United Kingdom.
- [24] Lemaitre, J.. 1996. *A Course on Damage Mechanics*. Springer-Verlag: Berlin, Germany.
- [25] Lemaitre, J. & Desmorat, R. J.. 2005. *Engineering Damage Mechanics, Ductile, Creep, Fatigue and Brittle Failures*. Springer-Verlag: Berlin, Germany.
- [26] Lubliner, J.. 2006. *Plasticity Theory*. Revised Ed. University of California at Berkeley: California, USA.
- [27] Malvern, L. E.. 1969. *Introduction to The Mechanics of A Continuous Medium*. Prentice-Hall: New Jersey, USA.
- [28] Mandel, J.. 1972. *Plasticité Classique et Viscoplasticité*. CISM, Courses and Lectures. No. 97 (Mandel, J.).
- [29] Mase, G. T. & Mase, G. E.. 1999. *Continuum Mechanics for Engineers*. 2<sup>nd</sup> Ed. CRC Press: Florida, USA.
- [30] Mashayekhi, M. et al.. 2005. Numerical Analysis of Damage Evolution in Ductile Solids. *Structural Integrity and Durability*. 1(1): 67-82. doi: 10.3970/sdhm.2005.001.067.
- [31] Mohamad-Hussein, A. & Shao, J. F.. 2007. Modelling of elastoplastic behaviour with non-local damage in concrete under compression. *Computers and Structures*. 85(2007): 1757-1768. doi: 10.1016/j.compstruc.2007.04.004.
- [32] Omatuku-Ngongo, E.. 2019. *Phase Field Modeling of Dynamic Brittle Fracture at Finite Strains*. OpenUCT: University of Cape Town, South Africa.
- [33] Onate, E. & Owen, R.. 2007 (eds.). *Computational Plasticity*. Springer: Dordrecht, Netherlands.

- [34] Peric, D.. 1993. On a class of constitutive equations in viscoplasticity: formulation and computational issues. *International Journal for Numerical Methods in Engineering*. 36: 1365-1393. doi: 10.1002/nme.1620360807.
- [35] Perrot, P.. 1998. *A to Z of Thermodynamics*. 1<sup>st</sup> Ed. Cambridge University Press: Oxford, United Kingdom.
- [36] Perzyna, P.. 1963. The constitutive equations for rate sensitive plastic materials. *Quarterly of Applied Mathematics*. 20(4): 321-332. doi: 10.1090/QAM/144536.
- [37] Perzyna, P.. 1966. Fundamental problems in viscoplasticity. *Advances in Applied Mechanics*. 9: 243-377. doi: 10.1016/S0065-2156(08)70009-7.
- [38] Reddy, J. N. 2013. *An Introduction to Continuum Mechanics*. 2<sup>nd</sup> Ed. Cambridge University Press: New York, USA.
- [39] Sansour, C. & Kollmann, F. G.. 1997. Viscoplastic shells: Theory and numerical analysis. *Archives of Mechanics*. 49(3): 477-511.
- [40] Sansour, C. & Kollmann, F. G.. 1998. Large viscoplastic deformations of shells: Theory and finite element formulation. *Computational Mechanics*. 21(1998): 512-525. doi: 10.1007/s004660050329.
- [41] Sansour, C., Kollmann, F. G. & Bocko, J.. 2003. A model of finite strain viscoplasticity with an anisotropic elastic constitutive law. *Deformation and Failure in Metallic Materials*. 2003: 107-135. doi: 10.1007/978-3-540-36564-8\_5.
- [42] Simo, J. C. & Hughes, T. J. R.. 1998. *Computational Inelasticity*. Springer-Verlag: New York, USA.
- [43] Skrzypek, J. J. & Ganczarski, A.. 1999. *Modeling of Material Damage and Failure of Structures, Theory and Applications*. Springer-Verlag: Berlin, Germany.
- [44] Steinmann, P., Miehe, C. & Stein, E.. 1994. Comparison of different finite deformation inelastic damage models within multiplicative elastoplasticity for ductile materials. *Computational Mechanics*. 13(1994): 458-474. doi: 10.1007/BF00374241.
- [45] von Mises, R.. 1913. Mechanik der Festen Körper im Plastische-deformablen Zustand. *Nachrichten von der Gesellschaft der Wissenschaften zu Göttingen, Mathematisch-Physikalische Klasse*. 1913: 583-592.
- [46] Voyiadjis, G. & Yaghoobi, M.. 2019. *Size Effects in Plasticity: From Macro to Nano*. Elsevier: United Kingdom.
- [47] Wriggers, P.. 2008. *Nonlinear Finite Element Methods*. Springer-Verlag: Berlin, Germany.
- [48] Zhang, W. & Cai, Y.. 2010. *Continuum Damage Mechanics and Numerical Applications*. Springer-Verlag: Berlin, Germany.

# Appendix

## A Expansion of finite element related quantities into index notation

These hold for each simulation step  $n + 1$ :

### A.1 Weak form of the momentum balance

The weak form is provided as

$$p_0^{weak} = \int_{\mathcal{B}_0} \mathbf{FS} : \text{Grad}(\delta \mathbf{u}) \, dV - \int_{\mathcal{B}_0} \mathbf{b}_0 \cdot \delta \mathbf{u} \, dV - \int_{\partial \mathcal{B}_{0(N)}} \mathbf{t}_0 \cdot \delta \mathbf{u} \, dA = 0, \quad (.2)$$

thus, in index notation this is

$$p_{0(ij)}^{weak} = \int_{\mathcal{B}_0} F_{ki} S_{ij} \delta u_{k,j} \, dV - \int_{\mathcal{B}_0} b_{0(e)} \delta u_i \, dV - \int_{\partial \mathcal{B}_{0(N)}} t_{0(e)} \delta u_i \, dA = 0 \quad (.3)$$

### A.2 Approximation of the displacement-related fields

The numerical approximations of the displacement field, its increment, its variational form and their spatial derivatives are provided in Eq. (5.10), Eq. (5.11) and Eq. (5.12). The index forms are:

$$u_{h(i)} = \sum_{I=1}^{N_e} N^I u_i^I \quad (.4)$$

$$\delta u_{h(i)} = \sum_{I=1}^{N_e} N^I \delta u_i^I \quad (.5)$$

$$\Delta u_{h(i)} = \sum_{I=1}^{N_e} N^I \Delta u_i^I \quad (.6)$$

$$u_{h(i,j)} = \sum_{I=1}^{N_e} \frac{N^I}{X_I} u_i^I \quad (.7)$$

$$\delta u_{h(i,j)} = \sum_{I=1}^{N_e} \frac{N^I}{X_I} \delta u_i^I \quad (.8)$$

$$\Delta u_{h(i,j)} = \sum_{I=1}^{N_e} \frac{N^I}{X_I} \Delta u_i^I \quad (.9)$$

### A.3 Index form of linearised quantities

As a consequence of linearising the weak form to define the incremental/iterative solution scheme for the displacement field,  $\mathbf{K}$ ,  $\mathbf{f}_{ext}$  and  $\mathbf{f}_{int}$  are produced. We express these in index notation as

$$K_{ij} = \int_{\mathcal{B}_{0(e)}} D_{ijkl} F_{sk} \frac{N^J}{X_l} F_{ri} \frac{N^I}{X_j} dV + \int_{\mathcal{B}_{0(e)}} S_{ij} \frac{N^J}{X_i} \frac{N^I}{X_j} dV, \quad (.10)$$

$$f_{ext(i)} = \int_{\mathcal{B}_{0(e)}} b_{0(i)} N_I dV + \int_{\partial \mathcal{B}_{0(e)}} t_{0(i)} \cdot N_I dA, \quad (.11)$$

and

$$f_{int(i)} = \int_{\mathcal{B}_{0(e)}} F_{ri} S_{ij} \frac{N^I}{X_j} dV. \quad (.12)$$

## B Expansion of return-mapping quantities into index notation

These hold for each simulation step  $n + 1$ :

### B.1 Algorithmic tangent operator

The full algorithmic form of the consistent tangent operator for this material damage model is:

$$\begin{aligned}
\frac{\partial S_{ij}}{\partial C_{rs}} &= -C_{ir}^{-1} C_{sk}^{-1} (\Sigma_{jk}^{trial} - 2G(1-M)_{n+1} \Delta t \lambda_{j+1} N_{kj}) \\
&+ (1-M)_{n+1} C_{ik}^{-1} \left( \left( K - \frac{1}{3}G \right) \delta_{kj} C_{rs}^{-1} + G \delta_{ks} C_{rj}^{-1} \right) \\
&- 2G(1-M)_{n+1}^2 \Delta t \frac{N_{ed}}{\left( \frac{2G\Delta t}{(1-M)_{n+1}} + \frac{2G\Delta t \lambda_{j+1} \left( \frac{\partial M_{n+1}}{\partial \lambda} \right)}{(1-M)_{n+1}^2} - \sqrt{\frac{2}{3}} \frac{\partial R_{n+1}}{\partial \lambda} \right)} \\
&\left( \left( K - \frac{1}{3}G \right) \delta_{de} C_{rs}^{-1} + G \delta_{ds} C_{re}^{-1} \right) C_{ik}^{-1} N_{kj} - \\
&\frac{2G(1-M)_{n+1}^3 \Delta t \lambda_{j+1}}{\|\text{dev}(\Sigma_{de}^{trial})\|} C_{ik}^{-1} \left( \delta_{kd} \delta_{je} - \frac{1}{3} \delta_{kj} \delta_{de} - N_{kj} N_{ed} \right) \left( \left( K - \frac{1}{3}G \right) \delta_{de} C_{rs}^{-1} + G \delta_{ds} C_{re}^{-1} \right).
\end{aligned}$$

### B.2 Stress computation

The algorithmic form of the *Mandel* stress update is:

$$\Sigma_{ij}^{trial} = (1-M)_{n+1} [K \text{tr}(\bar{\alpha}_{ij}) + G \text{dev}(\bar{\alpha}_{ij})]$$

$$\Sigma_{ij} = \Sigma_{ij}^{trial} - 2G (1-M)_{n+1} \Delta t \lambda_{j+1} N_{ji}.$$

When combined with the computational formulation of the *Mandel* stress tensor in Eq. (5.54), it is inevitable that the update of the 2<sup>nd</sup> Piola-Kirchhoff stress tensor is

$$S_{im} = C_{ij}^{-1} \Sigma_{jm}.$$

### B.3 Flow vector

The flow vector that is as a result of the maximum plastic dissipation principle and the associative flow rule is

$$N_{ab} = \frac{\text{dev}(\Sigma_{ab}^{trial})}{(1 - M)_{n+1} \|\text{dev}(\Sigma_{ab}^{trial})\|}.$$

### B.4 Strain measures

The right *Cauchy-Green* tensor  $\mathbf{C}$  and the distorted *Hencky* strain tensor  $\bar{\alpha}$  as used per this model are algorithmically implemented as

$$(C_{pl}^{-1})_{ij} = (\Delta F_{pl}^{-1})_{ik} (C_{pl}^{-1})_{kl} (\Delta F_{pl}^{-1})_{jl}$$

$$\alpha_{mi}^{trial} = \ln \left( C_{ij} (C_{pl}^{-1})_{jm} \right).$$

### B.5 *Strain-rate* measures

The plastic *strain-rate* tensor  $\mathbf{L}_{pl}$  was implemented algorithmically as

$$(L_{ij})_{pl} = \Delta t \lambda_{j+1} N_{ji}.$$



# C Ethics approval

Application for Approval of Ethics in Research (EIR) Projects  
Faculty of Engineering and the Built Environment, University of Cape Town

## ETHICS APPLICATION FORM


**Please Note:**


Any person planning to undertake research in the Faculty of Engineering and the Built Environment (EBE) at the University of Cape Town is required to complete this form **before** collecting or analysing data. The objective of submitting this application *prior* to embarking on research is to ensure that the highest ethical standards in research, conducted under the auspices of the EBE Faculty, are met. Please ensure that you have read, and understood the **EBE Ethics in Research Handbook** (available from the UCT EBE, Research Ethics website) prior to completing this application form: <http://www.ebe.uct.ac.za/ebe/research/ethics1>


| APPLICANT'S DETAILS  |  |   |
|--|--|---|
| Name of principal researcher, student or external applicant                | Paul Namalomba   |   |
| Department   | Department of Civil Engineering  |   |
| Preferred email address of applicant:                                      | nmlpau002@myuct.ac.za  |   |
| If Student   | Your Degree:<br>e.g., MSc, PhD, etc.   | MScEng (Structural Engineering & Materials) |
|  | Credit Value of Research: e.g., 60/120/180/360 etc.                              | 120   |
|  | Name of Supervisor (if supervised):  | Dr. Sebastian Skatulla (A/Prof)             |
| If this is a research contract, indicate the source of funding/sponsorship | Privately funded   |   |
| Project Title  | Towards a smeared damage model for ice, with von Mises plasticity considerations |   |

**I hereby undertake to carry out my research in such a way that:**

- there is no apparent legal objection to the nature or the method of research; and
- the research will not compromise staff or students or the other responsibilities of the University;
- the stated objective will be achieved, and the findings will have a high degree of validity;
- limitations and alternative interpretations will be considered;
- the findings could be subject to peer review and publicly available; and
- I will comply with the conventions of copyright and avoid any practice that would constitute plagiarism.

| APPLICATION BY  | Full name      | Signature  | Date       |
|---|----------------|--|------------|
| <b>Principal Researcher/ Student/External applicant</b> | Paul Namalomba |  | 16/02/2021 |

| SUPPORTED BY                         | Full name | Signature  | Date |
|--------------------------------------|-----------|--|------|
| <b>Supervisor (where applicable)</b> |           |  |      |

| APPROVED BY   | Full name             | Signature  | Date       |
|---|-----------------------|--|------------|
| <b>HOD (or delegated nominee)</b><br>Final authority for all applicants who have answered NO to all questions in Section 1; and for all Undergraduate research (Including Honours). | Prof. Alphose Zingoni |  | 09/07/2021 |
| <b>Chair: Faculty EIR Committee</b><br>For applicants other than undergraduate students who have answered YES to any of the questions in Section 1.                                 |                       |  |            |